# Improving the global coherency of the Shared Earth Model using static, dynamic and geomechanics data

Nicolas Mastio

# Improving the global coherency of the *Shared Earth Model* using static, dynamic and geomechanics data

# THÈSE

présentée et soutenue publiquement le 21 avril 2020

pour l'obtention du grade de

## Docteur de l'Université de Lorraine

### Spécialité Géosciences

par

**Nicolas MASTIO**

**Composition du jury:**

| | | |
|---|---|---|
| *Rapporteurs:* | Dr. Jérôme FORTIN | ENS Géologie, France |
| | Prof. Martin LANDRØ | NTNU, Norvège |
| *Examinateurs:* | Prof. Christian DAVID | Université de Cergy-Pontoise, France |
| | Dr. Alessandra RIBODETTI | Université de Nice, France |
| | Prof. Judith SAUSSE | Université de Lorraine, France |
| *Directeurs de thèse:* | Dr. Pierre THORE | Total SA, France |
| | Prof. Guillaume CAUMON | Université de Lorraine, France |
| *Co-directrice de thèse:* | Dr. Marianne CONIN | Université de Lorraine, France |
| *Invité:* | Dr. Yves LEROY | Total SA, France |

**GeoRessources - UMR 7359**
Université de Lorraine – CNRS
École Nationale Supérieure de Géologie
2 rue du Doyen Marcel Roubault - BP 10162
54505 Vandœuvre-lès-Nancy, FRANCE

# Remerciements

Je tiens à remercier Docteur Pierre Thore, référent en géophysique à TOTAL SE, qui a lancé ce sujet de thèse et qui a encadré la majorité de cette thèse. Sa enthousiasme et sa disponibilité m'ont été d'un grand secours.

Je remercie Professeur Guillaume Caumon, professeur à l'ENSG et responsable de l'équipe RING du laboratoire GéoRessources, pour sa gentillesse, son exigence et sa volonté de tout comprendre. Il a toujours su trouvé du temps pour m'aider quand cela été nécessaire.

Je remercie également Docteur Marianne Conin, maître de conférences à l'Université de Lorraine et enseignante au département Géoingénierie de Mines Nancy, qui déborde d'énergie et de motivation.

J'adresse mes sincères remerciement aux membres du jury de thèse qui ont accepté les conditions exceptionnelles d'une soutenance pendant le confinement.

Je tiens à exprimer toute ma reconnaissance à tous les personnes qui par nos échanges ont pu guidés ma réflexion et m'encourager. En particulier je tiens à remercier Docteur Yves Leroy, Professeur Albert Giraud et Docteur Jérôme Fortin pour leur aide sur l'aspect mécanique des roches.

Je remercie également l'ANRT, l'école doctorale SIReNa et l'équipe REM de TOTAL.

Enfin, je remercie les Pau's Wildlings pour tous ces moments que l'on a passé et que l'on va passer ensemble.

# Résumé

La production des réservoirs pétrolifères modifie l'état de contrainte du sous-sol. En effet, l'extraction du pétrole induit une diminution de la pression des pores. Cette contrainte est alors reprise par la roche réservoir ce qui induit sa compaction. De plus, le réservoir n'est la seule région affectée par la production : les couches sus-jacentes et sous-jacentes se déplacent aussi. Afin de comprendre l'effet de cette compaction du réservoir sur les couches sus-jacentes et sur la subsidence, des modèles géomécaniques sont construits. Le champ de déplacement et le changement d'état de contrainte sont calculés à partir du comportement élastique et du changement de la pression des pores. Néanmoins, ces modèles sont entachés d'incertitudes. D'une part, dans les champs pétrolifères, les données sont éparses et parfois mal-comprises. D'autre part, elles sont le résultat d'un traitement long et complexe tout au long duquel plusieurs erreurs peuvent être commises. Toutes ces incertitudes pesant sur ces données rendent leur interprétation et leur utilisation difficile.

Pour améliorer la prédictibilité des modèles, les données sismiques comme la sismique 4D sont utilisés dans le processus de construction du modèle géomécanique. La sismique 4D est empreinte par l'écoulement des fluides dans le réservoir, par sa déformation et celle des roches environnantes et par l'endommagement des roches. Dans la plupart des champs en production, la quantité de « time-shifts » (la différence en temps de trajet des réflecteurs) dans les roches sus-jacentes est importante. Ce signal s'explique en partie par la déformation, mais surtout par le changement de la vitesse des ondes sismiques. L'ouverture de petites fractures peut induire des changements de vitesse fort. Les modèles de fractures permettent d'expliquer ce changement de propriétés élastique durant un changement d'état de contraintes. Grâces à des modèles synthétiques, des auteurs ont prédits que le changement de vitesses est anisotrope parce que le changement d'état de contrainte dans les roches sus-jacentes est anisotrope. Cependant, l'anisotropie du changement de vitesse en sismique 4D n'est pas considérée. L'inversion 4D ne considère que des changements de vitesse verticale.

L'objet de cette thèse est d'extraire plus d'information dans les données pour créer une description plus précise du sous-sol. En utilisant des méthodes d'ensemble, le modèle géomécanique est mis-à-jour en utilisant des données issues de l'inversion sismique 4D. Pour ce faire, nous proposons en premier lieu d'obtenir la variation de pression du réservoir qui permet d'expliquer des données sismiques 4D. Cette étude suggère que la compartimentalisation du réservoir doit être réévaluée afin de comprendre les données sismiques. Puis, nous proposons

d'obtenir l'anisotropie du changement de vitesse à partir des données sismiques 4D avant sommation. Une reconstruction tomographique de ce changement de vitesse permet de réaligner la base au monitor. Cette méthode est appliquée sur un cas d'étude réel. L'anisotropie du champ de vitesse obtenue corresponds à une diminution d'epsilon ($\varepsilon$) et de delta ($\delta$) en termes de paramètres de Thomsen alors que le changement de vitesse verticale est faible. Les modèles géomécaniques montrent que la déformation des roches sus-jacentes est compatible avec l'ouverture de fractures horizontales ; ce n'est pas ce que l'on observe dans notre cas d'étude. Pour expliquer nos résultats, nous proposons un modèle de roches dans lequel se développe une fracturation verticale dans une roche saturée en eau. Ces fractures ont un rapport d'aspect faible (entre $10^{-2}$ et $10^{-3}$). Cette seconde approche nous interroge sur les hypothèses faites quand les prédictions des modèles géomécaniques sont comparées aux résultats d'inversion 4D.

Ces deux approches montrent un grand potentiel dans l'amélioration de la cohérence et la réduction des incertitudes dans les modèles quand différentes données sont confrontées. Davantage d'effort est nécessaire afin de construire un modèle du sous-sol qui permettrait de comprendre toutes les données à notre disposition.

# Abstract

Petroleum reservoir production modifies the stress state of the subsurface. Petroleum is drawn out, the reservoir pore pressure decreases, and the reservoir rock supports an additional loading. The reservoir is not the only affected area of the field during the production: the layers above (the overburden) and below (the underburden) move. To understand the effect of the reservoir compaction on the overburden and on the subsidence, geomechanical models are built. The rock elastic behavior and the pore pressure change are used to compute the displacement field and the stress changes. In any case, the models of petroleum fields are riddled with uncertainties because the data are sparse and fuzzy and often the results of a long and complex processing. The data uncertainties make the interpretation difficult, or the usage of the prediction made by reservoir models.

To reduce these uncertainties, seismic data such as time-lapse seismic (4D) is used in the geomechanical modelling workflow. 4D seismic are imprinted by the fluid flow in the reservoir, by the strain in the reservoir and in the overburden, and by the rock damaging. In most of the produced fields, the amount of time shifts (the reflectors time-arrival difference) in the overburden is significant. While only a small part of the overburden time shifts is explained by the strain, the velocity change plays a major role. But the relationship between the velocity change and the stress state change due to the reservoir compaction is not known. Microcracks opening is known to have a strong effect on the velocity change. Crack-based models can explain the stress-dependent velocity change in rock samples. Based on synthetics models, different authors predict that the velocity change is anisotropic because the stress change in the overburden is anisotropic. However, the velocity change anisotropy is not considered in the classic time-lapse seismic inversion as only the vertical direction is considered.

The object of this thesis is to extract more information from the data to create a more precise description of the subsurface model. A Mechanical History Matching of time-lapse inverted time strains using Ensemble methods is performed. For this, we first propose to invert for pressure variation in the reservoir to match the time-lapse seismic data. Using the empirical R-factor law, time-lapse time strains are predicted by the mechanical vertical strains. The reservoir pore pressure is updated to match the geomechanical model predictions with the time-lapse inversion results, suggesting that a new compartmentalization of the reservoir is needed to match the 4D information in the overburden. This first approach interrogates on the usage of reservoir simulation data in the geomechanical model. Second, we propose to recover the velocity change anisotropy from prestack time-lapse

seismic data. A tomographic reconstruction of the velocity change is performed by realigning the baseline to the monitor. The method is applied to a real case study. The retrieved anisotropic velocity change in the overburden corresponds to a large decrease in $\varepsilon$ and $\delta$ in terms of Thomsen parameters while the vertical velocity change is tiny. Classically, geomechanical models show an overburden stretching corresponding to an opening of horizontal cracks; this is not what we observe in the velocity change anisotropy. To explain the data, we propose a rock-physics model corresponding to vertical cracks with a small aspect ratio (between $10^{-2}$ and $10^{-3}$) in a water-saturated rock. This second approach interrogates on the assumptions made when the geomechanical model simulation results are compared to the time-lapse seismic inversion results.

As shown in the two approaches, a great potential for improving the consistency and reduce uncertainty of the models exists when mixing various data. This work is preliminary and much more work is required to integrate all sources of data into the shared earth model.

# Contents

# Introduction

Due to its economic interest, the subsoil of the Earth is a strategic place. In modern history, numerous examples show how the ongoing exploitation of geological resources can have an impact on the production and its surrounding environment, together with political/industrial choices. In the following, I will go through several examples of such environmental impacts of geoengineering application.

**Environmental impacts of the subsurface exploitation:** The production of oil and gas fields induces subsidence because of the reservoir compaction (e.g. 1.5 m in the field core for a 6 cm surface subsidence in Lacq onshore gas field—Rolando et al., 1997, Figure 1; reservoir compaction of about 12 m and 8 m seabed subsidence for the Ekofisk offshore field, North Sea; more than 6 m for the Valhall platforms—Figure 2C). The large subsidence of the Ekofisk field was surprising and it led the operator (former Phillips company) to jack-up the platform by about 6 m in 1987 (Figure 2A&B). Laboratory experiments showed that the water-saturated chalk have a lower compaction strength compared with the oil-saturated chalk (Sulak et al., 1988), and the attempts of re-pressurization in the reservoir with water injection provoked the water-weakening of the chalk formation. Regional seismic activity may also increases during reservoir production. Before production of the Lacq gas field started in 1957, the area was considered aseismic. However, since 1969, tens of seismic events with a magnitude superior to 3 occurred. In the U.S. state of Oklahoma, the frequency of earthquakes has considerably increased since the shale gas production has started (hundreds of earthquakes with a magnitude superior to 3 are recorded each year in the 2014–17 period—Holland, 2011; Benz et al., 2015, Figure 3). In France, geothermal energy is exploited in Soultz-Sous-Forêts (Alsace) where 5000-meter-deep wells have been drilled. Seismic events have been recorded after the hydraulic stimulation of the wells. This pilot site allowed to understand how the induced seismicity occurred in this region (Charléty et al., 2007; Cuenot et al., 2008). Nevertheless, the possible occurrence of earthquakes of magnitude superior to 3 makes difficult the exploitation of deep geothermal energy in France.

**Societal and political impacts of the subsurface exploitation:** The discovery of the huge onshore gas field of Groningen in 1959 transformed the energy balance of the Netherlands. Indeed, gas has progressively replaced coal and heavy fuel, and coal mines closed (the last coal mine in the Netherlands was officially closed in 1976). However, as for the Lacq gas field, the induced seismicity has become frequent since 1991 (5 earthquakes per year—Dempsey and Suckale, 2017) but their frequency has exponentially increased since 2003 and protest against gas extraction has occured (Figure 4). Because of the damages created by the local seismicity and subsequent mudslides, the

Figure 1: Lacq gas field, © Total S.A.

prime minister, Mark Rutte, decided to stop the production before 2030.

Because companies are responsible for the fields production consequences, they try to minimize such impacts. The environmental consequences of the resource exploitation need to be studied, and the fields monitoring during their exploitation is a way to achieve this goal.

### Reservoir monitoring to assess geomechanical risks

To measure and understand oil and gas reservoir production impacts, diverse monitoring methods have been developed (geological and geophysical logging, seismic monitoring, tracer concentration monitoring, remote sensing—see Djuraev et al., 2017). However, the lack of direct accessibility to the subsurface makes investigations difficult. Monitoring data are sparse, fuzzy, and riddled with inherent errors in measurements. For instance, electrical resistivity tomography (ERT) is a method to estimate the resistivity of the subsurface from electrical measurements made at the surface or in boreholes. While the resistivity is estimated in the whole space, only the resistivity between the electrodes are measured. The scarcity comes from the fact that these electrodes are limited in number. The precursor of the ERT, the mathematician Andrey Nikolayevich Tikhonov (1906–1993), developed theoretical tools to face this kind of ill-posed problem.

Among the numerous available methods, seismic monitoring methods such as time-lapse seismic are interesting regarding geomechanical risks. Elastic wave propagation is related to the mechanical properties of the earth; thus, the time-lapse attributes can potentially be translated into geomechanical properties changes (Hatchell and Bourne, 2005). Nevertheless, the mechanical phenomena which are responsible for these time-

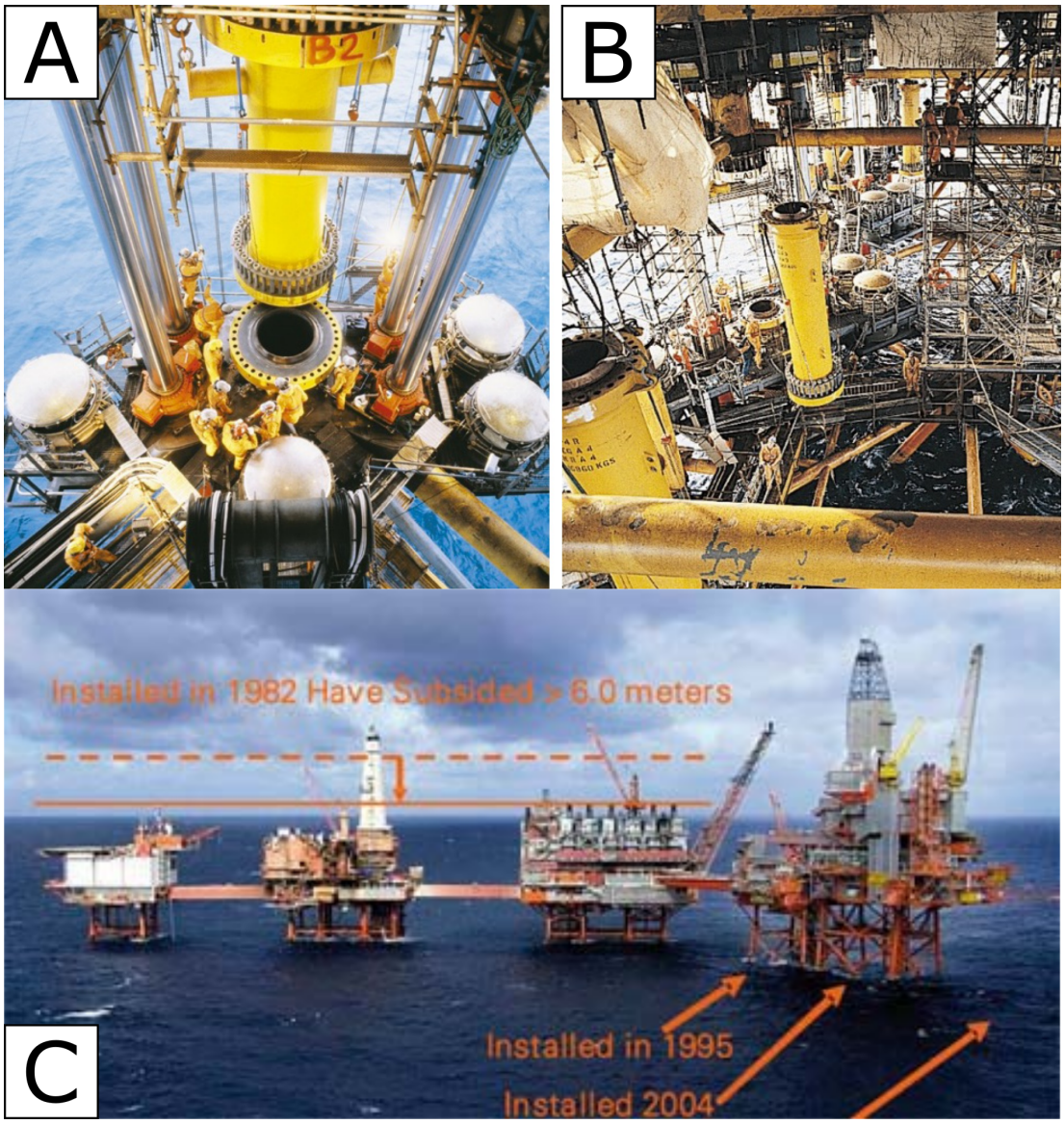


Figure 2: (A&B) Six-meter jacked up of the Ekofisk platforms to compensate for subsidence in the seabed in 1987, © ConocoPhillips. (C) Valhall platforms are impacted by the reservoir compaction and the subsidence, © BP (extracted from Kristiansen et al., 2009).

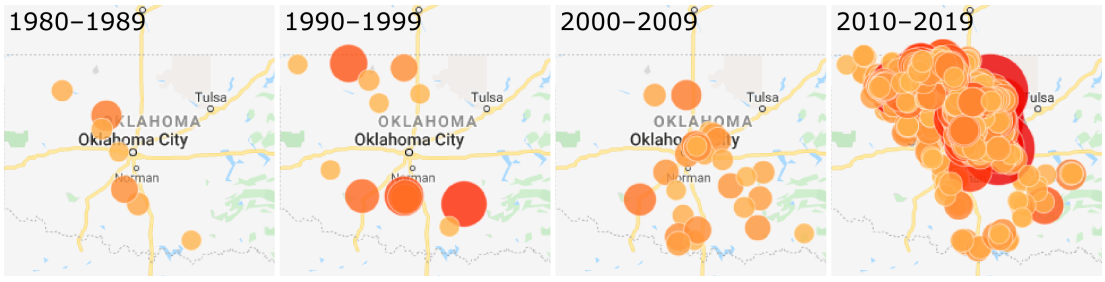


Figure 3: Earthquakes epicenter and magnitude in Oklahoma since 1980. Only earthquakes with a magnitude of 3 and higher are displayed. The data are provided by the United States Geological Survey. (https://earthquakes.ok.gov/what-we-know/earthquake-map/)

Figure 4: Protest against gas extraction in Groningen, Netherlands, 2018. © Pierre Crom/Getty Images

lapse effects are still poorly understood. In addition, time-lapse time-shifts maps are riddled with uncertainties, as they are the result of a long seismic processing. Repeatability issues due to differences in the acquisition between the base and the monitor can occur and it requires additionnal seismic preprocessing. Time-shifts cannot be recovered over the whole seismic survey: they can only be measured along reflectors. Time-shifts are also difficult to measure as the reflected energy is affected both by phase and amplitude changes. Time-shifts are contaminated with noise and they are sensitive to the regularization parameters (Rickett and Lumley, 2001). Furthermore, the conversion of time-shifts into velocity change is ambiguous because the geometrical deformations such as layer thickness changes are generally ignored, and the seismic waves are assumed to propagate vertically only. This assumption can lead to misposition of the velocity change (Edgar and Mastio, 2017). The velocity change is also suspected to be anisotropic (Sayers, 2006). Nonetheless, as only the vertical velocity change is considered, the anisotropy is not known. The time-lapse velocity change suffers from all these assumptions and their interpretation in terms of geomechanics is difficult.

## Thesis objectives

Different models of the subsurface are built in different disciplines. Geophysicists build velocity model to better image the reflectors and provide a seismic image in depth. Geologists interpret the seismic image in terms of structures and depositional features. Reservoir engineers interpret the production data in terms of permeability and porosity of the reservoir. Each model allows to learn something on the subsoil behavior, but when the different disciplines do not consider each other's, it can lead to incoherencies between the model predictions. How can we use monitoring data to follow the subsurface

movements and assess risks in the reservoir and in the overburden?

While data are used to constrain the different models of the field, matching them is not a guaranty to have more reliable models. Using the data to constrain the model is an inverse problem (e.g., Tarantola, 2005). Solving this kind of problem requires (i) the model parametrization which controls the degree of freedom of the model (e.g., the permeability for the reservoir model or the pore pressure drop for the geomechanical model), (ii) the forward modeling which uses the physical laws and the model parameters to predict the anticipated results of monitoring measurements (e.g. a flow simulator or a finite element code which solves for the stress change) and (iii) accurate measurements of predicted properties (e.g. the pore pressure at the well or the stress change). How can we ensure the physical meaning of the model parameters when the data are noisy and the forward problem is not fully understood?

It can be reasonable to change the model parameters, especially if it allows the models to be more consistent with the data. In the case of dynamic reservoir data, this process is called history matching. For instance, reservoir engineers use a reservoir model in which the fluid flow dynamics is simulated and compare it to the existing production and injection rates, and time-lapse attributes of the reservoir. Then they perform history matching loops, together with the geologist, to update the reservoir properties and the resulting permeability maps. As compacting areas induce a measurable velocity change, can we use time-lapse seismic data to detect reservoir compartmentalization?

## Contributions and thesis outline

In this thesis, we propose methods to reconciliate the different models of the reservoir.

In the first part, the theory which relates the mechanical stress changes to the fluid flow behavior, or poroelasticity, is presented. This theory consists in a set of equations which are solved numerically within two codes (one for the fluid flow and the other for the geomechanics). The stress-dependent rock-physics models such as the third-order elastic theory and the effective elastic models are reviewed. These models give a better insight of the expected geomechanical signal we expect in the time-lapse seismic data, especially in terms of anisotropy.

In the second part, a geomechanical workflow is proposed to address the differences observed in the time-lapse seismic inversion and the time-lapse predicted effects in the geomechanical model. The ensemble Kalman filter (EnKF), an ensemble-based method is used to update the reservoir properties of the geomechanical model, to provide a better match of the time-lapse seismic data.

In the third part, another geomechanical workflow is proposed to estimate the in-situ stress in area where active faults have been observed. In this area, the activity of these high-angle dip faults cannot be explained by an Andersonian stress state. The boundary conditions of the geomechanical model are calibrated using well data and constrained with yield criterion on the faults using Covariance Matrix Adaptation Evolution Strategy (CMA-ES).

In the fourth and last part, we use anisotropic inversion contained in the time-lapse seismic to determine an appropriate rock-physics model. The overburden stretching is suspected to open cracks, which are responsible for the time subsidence observed

at the reservoir top. The stress change regime in the overburden should in principle open horizontal cracks and create an anisotropic velocity change. Nonetheless, this anisotropy has never been retrieved in time-lapse studies: a new ray-based method is proposed to recover it. A tomographic reconstruction of the velocity change is performed by realigning the baseline to the monitor using prestack data. The method is applied to a real case study and a rock-physics model based on cracks is determined. This part was submitted to *Geophysics* and it is still in revision.

## Context of the thesis

### Administrative and scientific frame

This thesis is a collaboration between an industrial company, Total S.A., and an academic laboratory, GeoRessources (Université de Lorraine/CNRS), and it was followed by Association Nationale de la Recherche et de la Technologie (ANRT). Total is a French multinational oil company that was created in 1924 under the name of "Compagnie Françaises des pétroles (CFP)". Total takes actions in different domains: oil and gas exploration, production but also in the refining, marketing, trading, and shipping of crude oil and different petroleum products. This thesis took place at the CSTJF. GeoRessources, as a research laboratory on geology, covers geological ressources, with their exploration, exploitation, valorisation and societal impacts. I was associated to the RING team which is specialized in numerical geology. It addresses mathematical and numerical descriptions of geological objects. The student spent approximately 80% of my time in Pau at the CSTJF and 20% in Nancy at the GeoRessources laboratory.

### Communications

### Published article

1. N. Mastio, P. Thore, M. Conin, and G. Caumon. Determination of a stress-dependent rock-physics model using anisotropic time-lapse tomographic inversion. *Geophysics* 85: C141–C152. doi: 10.1190/geo2019-0526.1

### Conferences

1. J. Edgar and N. Mastio. Time-lapse velocity change tomography. In *79th EAGE Conference and Exhibition 2017*, vol. 2017, p. 1–5, 2017. doi: 10.3997/2214-4609.201700810

2. N. Mastio, P. Thore, M. Conin, and G. Caumon. Consistency of rock physics model predictions and anisotropic time-lapse tomographic results. In *81st EAGE Conference and Exhibition 2019,* vol. 2019, p. 1–5, 2019. doi: 10.3997/2214-4609.201900820

3. P. Thore, A. Mazuyer, and N. Mastio. Constrained inverse method for estimating virgin stress state. In *81st EAGE Conference and Exhibition 2019*, vol. 2019, p. 1–5, 2019. doi: 10.3997/2214-4609.201901151

## Introduction (en français)

Le sous-sol est un endroit stratégique de la Terre à cause de son intérêt économique. Dans l'histoire moderne, de nombreux exemples montrent comment l'exploitation de ces ressources géologiques peut impacter leurs mises en production, l'environ-nement et, les choix politiques et industriels. Dans ce qui suit, nous présentons plusieurs exemples.

Plusieurs cas illustrent les impacts environnementaux de l'exploitation du sous-sol. Le champ gazier de Lacq, dans le Sud-Ouest de la France, a été produit depuis 1957. Sa production a engendré une subsidence de 6 cm en surface pour une compaction du réservoir de 1.5 m mesurée au niveau du puits, et une activité micro-sismique. Une dizaine d'événements sismiques d'une magnitude supérieure à 3 ont été enregistré depuis 1969. Dans les champs pétroliers en Mer du Nord, la subsidence mesurée au niveau du fond marin est beaucoup plus importante, de l'ordre du mètre. Le cas le plus extrême est le champ d'Ekofisk, ou la subsidence a été tel que d'important travaux imprévus ont dû être effectué pour ré-élevé la plateforme en 1987. Des expériences en laboratoire ont montré que les tentatives de repressuriser le réservoir en injectant de l'eau ont participé à l'importante compaction du réservoir puisque le réservoir, constitué de craie, a une compétence mécanique plus faible quand il est saturé en eau. Dans l'état de Oklahoma aux États-Unis, l'exploitation des gaz de schistes a considérablement augmenté l'activité sismique régionale. La stimulation hydraulique est connu pour engendrer une activité sismique, comme il a été sur le site pilote en géothermie de Soultz-Sous-Forêts en Alsace. Le champ gazier de Groningen aux Pays-Bas a montré que l'activité sismique induite par la production peut entrainer une contestation des populations contre les projets d'exploitation du gaz. Le premier ministre, Mark Rutte, a décidé d'arrêter la production avant 2030.

Comme les sociétés pétrolières sont responsables des conséquences de la production des champs, elles mettent tout en œuvre pour limiter les impacts. La surveillance des champs durant leur production permet d'atteindre ce but.

Afin de mesurer et de comprendre les impacts de la production des réservoirs d'huile et de gaz, diverses méthodes de surveillance ont été développées. Cependant, la difficulté d'accéder au sous-sol rends son investigation difficile. Les données issues de la surveillance sont éparses, mal-comprises et, entachées d'erreurs. Parmi les méthodes de surveillance, la sismique 4D est intéressant concernant les risques géomécaniques. En effet, la propagation des ondes élastiques est relié aux propriétés mécaniques des roches traversées. Les attributs générés par la sismique 4D peuvent potentiellement être traduit en changement de propriétés géomécaniques. Néanmoins, les phénomènes géomécaniques induisant ces effets 4D ne sont pas bien compris. De plus, le traitement sismique qui permet d'aboutir à ces attributs est entaché d'incertitudes. Le manque de compréhension des phénomènes sus-jacents à ces effets 4D ont entraîné des hypothèses fortes, ce qui rend les attributs 4D difficile a interprété, voir erronés.

L'objectif de cette thèse est de mieux comprendre les phénomènes géomécaniques qui induisent des effets 4D. Les différents modèles du sous-sol (le modèle géologique, le modèle réservoir et le modèle géomécanique) sont mis en lumière

avec les données issues de la sismique 4D. Comme il s'agit de comparer des données d'acquisition avec des modèles, nous étudions un problème inverse dans lequel on ne sait pas si on doit faire plus confiance dans les données ou dans les modèles. Mais la mise en cohérence des modèles et des données permettrait d'aboutir à un modèle du sous-sol plus robuste ainsi que de mieux comprendre les données issues de la sismique 4D.

Dans cette thèse, nous proposons des méthodes pour réconcilier les différents modèles du réservoir. Dans une première partie, la théorie qui relie les changements mécaniques à l'écoulement du fluide, aussi appelé poroelasticité, est présenté. Cette théorie consiste en une suite d'équations qui sont résolues numériquement dans deux codes (un pour l'écoulement et un pour la géomécanique). Les modèles de roches qui permettent d'expliquer le signal 4D sont passés en revue. Ces modèles donnent un aperçu du signal que l'on devrait mesurer en sismique 4D, en particulier en termes d'anisotropie. Dans une deuxième partie, un workflow géomécanique qui adresse les différences observés entre les résultats d'inversion 4D et ceux prédits par les modèles géomécaniques est présenté. Le filtre de Kalman d'ensemble est utilisé pour mettre à jour les propriétés du modèle géomécanique dans le réservoir, afin de fournir un meilleur lien avec les résultats d'inversion. Dans une troisième partie, un autre workflow géomécanique qui estime les contraintes in-situ avec des critères d'activation de failles est proposé. Cette méthode est appliquée dans un cas d'étude, ou l'activité des failles ne peut pas être comprises avec un état de contrainte Andersonien. Les conditions aux limites du modèle géomécanique sont calibrés en utilisant des données de puits et des critères de rupture au niveau des failles en utilisant l'algorithme d'optimisation CMA-ES. Dans une quatrième et dernière partie, nous utilisons les informations anisotropes contenues dans la sismique 4D pour déterminer un modèle de roches approprié. Les déformations dans les roches sus-jacentes au réservoir sont susceptibles d'ouvrir des fractures, ce qui expliquerait le décalage temporel observé au toit du réservoir en sismique 4D. En principe, le changement d'état de contrainte aurait tendance à ouvrir des fractures horizontales, ce qui induit un changement de vitesse anisotrope. Néanmoins, cette anisotropie n'a jamais été mesurée en sismique 4D. Une nouvelle méthode basée sur des rayons sismiques est proposée afin de retrouver cette anisotropie. Une reconstruction tomographique du changement de vitesse est proposé en réalignant la base au moniteur en utilisant des données sismiques avant sommation. Cette méthode est appliquée sur un cas d'étude réel et un modèle de roches basé sur des fractures est déterminé. Cette partie a été soumise dans le journal *Geophysics* et est encore en révision.

# Chapter 1

# Reservoir geomechanics and 4D effects

**Contents**

## Résumé du Chapitre 1

L'exploitation des réservoirs d'huile et de gaz soulève des problème géomécaniques tels que la subsidence, les glissements bancs sur bancs le long de la stratification, la réactivation de failles ou encore la fracturation de la roche couverture. La prédiction de ces risques requiert la construction et la calibration d'un modèle géomécanique du réservoir et des roches environnantes. Ce dernier est une synthèse de différents modèles : un modèle stratigraphique et structural qui définit une géométrie des couches, rempli de propriétés élastiques obtenues par inversion sismique et un modèle réservoir où est estimé le changement de la pression des pores grâce à la simulation d'écoulement des fluides. Par conséquent, la construction du modèle géomécanique est interdisciplinaire.

Dans l'industrie pétrolière, les modèles géomécaniques sont construits comme la succession de construction des modèles suivants : le modèle structural, le modèle réservoir et, le modèle géomécanique. Le changement d'état de contrainte est estimé par la résolution des équations de la poroélasticité. Ces équations sont le couplage des équations de l'écoulement des fluides et de l'équilibre mécanique de la roche. Leurs résolutions nécessitent donc un modèle réservoir et un modèle géomécanique. Dans le premier, la conservation de la masse de fluide et la loi de Darcy sont résolus. Dans le second, le comportement élastique de la roche, l'équilibre mécanique, ainsi que les équations de compatibilité de Beltrami sont résolus. Afin d'étudier la sensibilité des paramètres régissant le comportement hydromécanique du réservoir, ces équations sont décrites en déformation plane. Ce cas particulier nous permet d'étudier des solutions simples dans lesquelles les principaux paramètres qui régissent les déformations et les changements de contraintes durant la production du réservoir sont connus.

Pour calibrer le modèle géomécanique avec des données sismiques 4D, différents modèles de roches liant les paramètres géomécaniques au changement de vitesse des ondes élastiques sont présentés, sur la base d'une revue bibliographique. Les essais effectués en laboratoire sur des échantillons de roches montrent un comportement élastique non linéaire vis-à-vis de la propagation des ondes. Cette non-linéarité est expliquée par l'ouverture et la fermeture de micro-fractures de la roche. Ces modèles de roches peuvent être aussi utilisés pour comprendre le changement de la vitesse des ondes observé en sismique 4D, puisqu'ils mettent en jeu des paramètres microstructuraux sans dimension. Néanmoins, le changement d'échelle entre celle du laboratoire et celle du réservoir n'est pas direct, puisqu'un désaccord entre les valeurs de R-factor est observé. Les modèles de roches montrent aussi que l'étude de l'anisotropie de la vitesse des ondes permettent de mieux cerner l'état de relaxation du fluide dans les fractures.

The exploitation of oil and gas reservoirs may raise geomechanical problems such as subsidence, bedding-parallel slip, well failure, fault reactivation, caprock fracturing, ... The prediction of these hazards requires the building and the calibration of a geomechanical model of the reservoir and the surrounding rocks. The geomechanical model is a synthesis of the different reservoir models made during the exploitation of petroleum fields: it requires a stratigraphic model for the layers geometry, elastic properties obtained by seismic inversion, and the pore pressure change estimated with fluid flow simulation in the reservoir model. Therefore, geomechanical model building is very interdisciplinary (Ringrose and Bentley, 2016).

In the following, we present how geomechanical models are built and calibrated in the petroleum industry. The theoretical models behind fluid flow and rocks' mechanical behavior in the reservoir, or poroelasticity, is presented (section 1.1.1). The modelling procedure is described as the succession of model building steps: first the structural model, then the reservoir model and finally the geomechanical model (section 1.1.2). To fulfil the need for sensitivity analysis to understand the main factors in hydromechanics process, the poroelastic equations are written in plane strain conditions. Some simple poroelastic solutions are derived to highlight the main parameters which influence the strain and stress fields during reservoir production (section 1.1.3). To calibrate the geomechanical model with time-lapse seismic data (section 1.2), based on literature and laboratory experiments results, different models linking the geomechanics to the time-lapse velocity change are presented (section 1.3).

## 1.1 Reservoir geomechanics

### 1.1.1 Poroelasticity

In the subsurface, the oil and gas are contained in the rocks' porosity. These fluids are under pressure and exert a force on the solid skeleton. The theory of the porous medium mechanics in small strain, or poroelasticity, explains the interaction between the fluid flow and the rock mechanical behavior (Biot, 1941; Rice and Cleary, 1976). This thermodynamic theory models the saturated rock as the superposition of two continuous mediums. The first one describes the elastic behavior of the skeleton, where the strain is a linear function of the effective stresses (the stress applied on the solid skeleton). The second one describes the fluid flow dynamics with the fluid mass, i.e. the pore pressure.

In an isotropic medium, the poroelastic problem consists in solving the following set of equations:

- Fluid mass conservation

  In a continuous medium, without any source or sink term, the conservation of the fluid mass $m_f$ over a small volume of rock can be written in function of the fluid mass flow $\boldsymbol{w}$ as

$$\frac{\partial m_f}{\partial t} = -\operatorname{div} \boldsymbol{w} \quad . \tag{1.1}$$

The fluid mass flow corresponds to $\boldsymbol{w} = m_f \boldsymbol{u_r}$, where $\boldsymbol{u_r}$ is the equivalent fluid velocity relative to the rock skeleton.

- The equilibrium equation

$$\operatorname{div} \boldsymbol{\sigma} + (m_s + m_f)\boldsymbol{g} = \boldsymbol{0} \quad , \tag{1.2}$$

where $\boldsymbol{g}$ is the gravity and $\boldsymbol{\sigma}$ is the total stress tensor (the stress applied on the system skeleton and fluid), and $m_s$ is the material density. The acceleration part of the solid and the fluid are ignored as the fluid flow and the rock strain are slow. The only body force that is considered is the gravity.

- The Darcy's law (1856)

$$\boldsymbol{w} = -\frac{\rho_f}{\mu} \boldsymbol{K}.(\mathbf{grad}\, p - \rho_f \boldsymbol{g}) \quad , \tag{1.3}$$

where $\rho_f$ is the fluid density, $\mu$ is the dynamic viscosity, and $p$ the fluid pressure. The permeability $\boldsymbol{K}$ is a second-order tensor. Its unit is the $\mathrm{m}^2$ in the standard unit. In the petroleum industry, the unit is the darcy (D) or the millidarcy (mD) such as 1 D = 0.9869233 $\mu\mathrm{m}^2$.

- The poroelasticity

The stress-strain relation is linear under small deformation and it can be written as

$$\boldsymbol{\sigma} = \lambda \operatorname{tr}(\boldsymbol{\varepsilon})\, \mathbf{1} + 2\mu\boldsymbol{\varepsilon} - bp\mathbf{1} \quad , \tag{1.4}$$

where $\lambda$ and $\mu$ are the Lamé coefficients and $b$ Biot's coefficient, and $\varepsilon$ the strain tensor field. $\mathbf{1}$ is the second-order identity tensor.

$$\delta m_f = \rho_f \left( b \operatorname{tr}(\boldsymbol{\varepsilon}) + \frac{p}{M} \right) \quad , \tag{1.5}$$

where $\delta m_f$ is the fluid mass variation which can be decomposed into two parts: the fluid mass variation due to the porosity change $\delta\Phi$ and due to a fluid density change $\delta\rho$ ($\delta m_f = \rho_f \delta\Phi + \Phi\delta\rho_f$). $M$ is the Biot's modulus.

In poroelasticity, two limit cases are generally considered: drained ($p = 0$) and undrained ($\delta m_f = 0$) conditions. Drained conditions occur when there is no change in pores' water pressure due to external loading: the fluid can drain out easily causing volumetric strains in the subsoil. Undrained conditions occur when the rate of loading is much quicker than the rate at which the fluid can drain out of the soil. The external loading is partly taken by the fluid with an increase in the pore pressure. The soil volume change is then limited to the elastic behavior of the skeleton and the fluid compressibility.

The Biot's coefficient $b$ is related to the overall specimen incompressibility $K$ and the skeleton incompressibility $K_s$ by

$$b = 1 - \frac{K}{K_s} \quad , \tag{1.6}$$

Biot's modulus $M$ is linked to the pore compressibility $N$ and the fluid bulk modulus $K_f$ by

$$\frac{1}{M} = N + \frac{\Phi}{K_f} \quad . \tag{1.7}$$

- Compatibility equations were first described by Barré de Saint-Venant in 1864 and proved rigorously by Beltrami in 1886

$$\varepsilon_{ik,jl} - \varepsilon_{jk,il} - \varepsilon_{il,jk} + \varepsilon_{jl,ik} = 0 \quad . \tag{1.8}$$

### 1.1.2 The industrial workflow

In the petroleum industry, Biot's coefficients and modulus are not known. Thus, we can use the effective stress hypothesis, or Terzaghi stress (Terzaghi, 1925, 1936). This is equivalent to assuming that the volumetric strain of the solid skeleton is negligible compared to the porosity variation. This implies that $b = 1$ and $N = 0$. As the reservoir is produced during several years or decades, a long-term solution can be considered. This solution is such as:

$$\begin{cases} \operatorname{div} \boldsymbol{w} = 0 \\ \boldsymbol{w} = -\frac{\rho_f}{\mu} \boldsymbol{K}.(\mathbf{grad}\, p^{(\infty)} - \rho_f \boldsymbol{g}) \end{cases} , \tag{1.9}$$

where $p^{(\infty)}$ is the long-term pore pressure change. Therefore, the long-term hydraulic problem is not coupled to the mechanical problem. Nevertheless, the mechanical problem depends on the pore pressure change:

$$\boldsymbol{\sigma} = \lambda \operatorname{tr}(\boldsymbol{\varepsilon})\, \mathbf{1} + 2\mu\boldsymbol{\varepsilon} - p^{(\infty)}\mathbf{1} \quad . \tag{1.10}$$

In general, the fluid flow dynamics and the geomechanics are solved separately in different model and solvers (e.g. Bouziat et al., 2019). The fluid flow dynamics is simulated by solving the fluid mass conservation and the Darcy's law (equations 1.1 and 1.3). The displacement field is computed by solving the equilibrium, poroelasticity and compatibility equations (equations 1.2, 1.4, and 1.8) in the geomechanical model and uses the pore pressure change computed in the reservoir model (e.g., De Gennaro et al., 2008; Herwanger and Koutsabeloulis, 2011)

#### 1.1.2.1 The structural model

In the petroleum industry, the subsurface knowledge is limited to seismic and well data:

- Seismic surveys allow to image the subsurface by sending acoustic waves in the subsurface. A source (air gun in marine acquisitions or vibrators or explosives in land acquisitions) sends elastic waves in the subsoil. The impedance contrast between the geological layers reflects a part of the energy and the corresponding wave is recorded using a receptor, either a hydrophone or a geophone. Geophysicists process the recorded data to obtain an image of the subsurface. This seismic image is an indirect vision of geological structures. Signal processing techniques are well adapted for layered media which are laterally continuous, but imaging complex geological structures is challenging. Some materials such as salt distorts seismic waves making it difficult to image any structure under it. Furthermore, the

low frequency of the seismic wave used (about 50 Hz) implies a limit in structures resolution.

- Borehole imaging and formation logging provide information on the rock properties along the well trajectory. During exploration, coring allows to retrieve rock samples, which can later be analyzed in the laboratory. Measurements such as the clay and sand content as well as porosity are performed while thin sections provides a more detailed facies description. If coring is not performed, cuttings are studied to deduce the lithology of the drilled formation. While—or after (wireline logging)—drilling, well logging is performed. Several tools are sent down in the well and measured rocks' natural radioactivity, their interval velocity, ... Compared to seismic data, log data have a higher vertical resolution. Nevertheless, the lateral heterogeneity is not retrieved in vertical wells.

Geologists use seismic images to pick horizons and faults. A stratigraphic column is completed with depositional information such as conformities and unconformities. Structural geomodeling tools use geological rules to interpolate the picked features into surfaces and handle their intersections. The seismic data quality impacts the resolution of the structural interpretation: the conceptual geological scheme is prioritized over hazardous seismic data interpretation. As multiple geological scenarios can be compatible with the seismic data, structural model can be seen in a stochastic manner (e.g., Julio et al., 2015). The resulting structural model is a geological representation of the seismic data. The structural model is helpful when the model is infilled with geological properties such as porosity, permeability, and net-to-gross, because these properties are ruled by the deposit and the diagenesis. The interested reader can refer to Wellmann and Caumon (2018).

#### 1.1.2.2 The reservoir model

The reservoir model uses a regular grid that follows the stratigraphy to simulate the fluid flow. Heterogeneities have generally shorter correlation range along the deposition direction (T–axis) than along an isochronous surface (UV–plane). For this reason, and because the flow is mainly horizontal, the cell size is thin in the direction normal to the stratification (around 1 m) and larger in the tangential direction (around 50 m). A pillar gridding representation is commonly used for reservoir modelling (Ringrose and Bentley, 2016).

Net-to-gross, porosity, saturations, and permeability properties are locally known along the well through log data. They provide a high vertical resolution of the material properties, but the lateral heterogeneities are not known. Well tests such as drill stem test (DST) or extended well test (EWT) are performed to estimate the flow behavior around the producing wells (Spivey and Lee, 2013). DST are performed during several hours or a few days and provide surface fluid samples, indications of productivity, short-term flow, and pressure buildups to estimate the effective permeability and the drainage radius. EWTs are longer than DSTs (they can extend to several weeks or months) and are used to characterize the reservoir flow further away from the wells. They provide an estimation of the reservoir volume and the interwell communication as well as production-related data.

To understand flow at the reservoir scale, reservoir's properties are populated in the reservoir grid. A geostatistical analysis is performed to reproduce the spatial repartition of these properties (variogram analysis on well data or analogue outcrop—Pyrcz and Deutsch, 2014). Interpolation methods can differ: kriging, sequential Gaussian simulation (SGS), etc. This variability is first simulated in a planar grid (UVT grid). As the past geological event may have altered the spatial organization of the reservoir layers (folded or faulted layers), a UVT mapping is performed to relate the depositional layering to the current one (Mallet, 2004). This allows to preserve the spatial repartition and continuity of the properties when infilling the reservoir model.

#### 1.1.2.3 The geomechanical model

Building a geomechanical model requires to understand the rocks mechanics, characterized by a behavior law and mechanical properties. Such parameters can be measured in the laboratory. Mechanical tests such a uniaxial and triaxial tests are performed on rock samples to provide a stress-strain curve. However, these tests are only performed on a limited number of rock samples. Indirect measurements of the elastic properties, such as seismic data, enrich these sparse measurements. Seismic waves investigate all the seismic cube and elastic wave velocities can be used to estimate elastic properties over a larger volume. High-frequency elastic waves (ultrasonic) are also used at the laboratory to monitor damages to the rock sample during mechanical tests. Contrary to compression tests (uniaxial or triaxial test), which are performed until rupture of the sample, ultrasonic tests are a non-destructive procedure. These can also be repeated, for instance with new parameters such as a different pore pressure, confinement stress or water saturation. Ultrasonic machines also have the advantage of being transported easily while mechanical testing machines cannot. However, despite the use of an appropriate rock-physics model, the 'dynamic' elastic properties estimated from seismic velocities or from the ultrasonics laboratory measurements are different from the 'static' elastic properties measured with mechanical tests on rock samples (Christaras et al., 1994; Guéguen and Palciauskas, 1994; Al-Shayea, 2004; Ciccotti and Mulargia, 2004; Sastre and Calleja, 2004; Song et al., 2004; Saenger et al., 2006; Martínez-Martínez et al., 2012).

The equality of the 'static' and 'dynamic' properties ($K_{\text{stat}} = K_{\text{dyn}}$ and $G_{\text{stat}} = G_{\text{dyn}}$) is valid for an isotropic, homogeneous, linear elastic material. This may be valid for steel (Ledbetter, 1993) but for rocks, there can be large differences between static and dynamic moduli, and the dynamic stiffness is almost always larger than the static one (Simmons and Brace, 1965; Walsh, 1965b; Cheng and Johnston, 1981; Martin III et al., 1994; Yale et al., 1994; Tutuncu et al., 1998; Fjær, 2009; Martínez-Martínez et al., 2012). This difference is explained by the rock heterogeneities such as fractures, cracks, and cavities) as well as the effect of fluid. In the industry, this problem is solved by assuming that these two elastic properties (static and dynamic) are correlated. In most studies, a linear relationship is used and the geomechanical model parameters are derived from sonic properties (either from seismic inversion or ultrasonic laboratory measurements). Fjær (2019) points out that the "ratio" between static moduli and dynamic moduli is complex and depends on several conditions including stress state and stress history. He comments: the "comparison of static and dynamic moduli is often hampered and maybe

mistaken due to insufficient characterization of anisotropy" (Fjær, 2019). Despite efforts to estimate the 'static' elastic properties from various measurements, the difficulty of accessing the correct elastic properties induces uncertainties in the geomechanical model.

The translation of the geological structural knowledge into geomechanical features is also complex. For instance, faults conveniently explain the lateral discontinuity of the layers but their contributions to the geomechanical model have not been established in the frame of reservoir modeling. Faults mechanics are modelled by a frictional contact on a surface separating two volumes. A fault reactivation depends on the in-situ stress, the pore pressure in the fault and fault properties such as the fault orientation and the fault friction angle (Hawkes et al., 2004). Depending on the seismic imaging accuracy, the fault orientation can be known is some case. Other properties can be complexed to measure (Guglielmi et al., 2008). Furthermore, allowing the fault to slide creates a non-linear mechanical problem, which is more difficult to solve. To preserve a linear approach, only the damage area can be modelled by reducing the elastic properties around the fault. Seismic methods do not necessarily image accurately the fault and the properties around it. Faults geometry and their properties have a great impact on stress change, especially when faults are close to the reservoir. Consequently, the geomechanical model is very uncertain in faulted areas.

In the industry, the structural model focuses only on the reservoir geometry and the overburden layering for drilling purposes. Nevertheless, the geomechanical model requires the knowledge of the underburden. This area is hardly ever investigated by the wells because drilling stops at the bottom of the reservoir. Also, seismic waves do not correctly image deep structures. Laterally, the model length should be 10 times bigger than the reservoir length to avoid boundary effects. But the seismic cube, the structural model and the geological model do not contain this area because they are dimensioned to the field development area. Therefore, geometrical features and mechanical properties are missing. The continuity of the layering and elastic properties can be assumed but this adds uncertainties to the geomechanical model.

Once the geomechanical model is build, and the mechanical properties are known, the model is discretized using simple geometrical elements to numerically solve the mechanical equations. The finite element method is often used to solve the mechanical equations. It can be performed on a structured mesh based on hexahedra in 3D or quadrilaterals in 2D when the layer geometry is simple (e.g. Herwanger and Horne, 2009; Herwanger et al., 2010). However, unstructured meshes are preferred for geomechanical model because they can handle more complex structures (Matthai et al., 2007; Botella et al., 2016). They are typically based on tetrahedra in 3D or triangles in 2D. These geometrical objects can conveniently mesh an eroded surface for instance. Simple boundary conditions are generally imposed. The seabed is considered as a free surface. Neumann boundary conditions are used to impose $\sigma_n = \sigma.n = 0$ along this surface, where $n$ is the normal vector to the surface. For other boundaries, the displacement is fixed: the horizontal displacement on the lateral boundaries and the vertical displacement on the bottom boundary. This can be set using the Dirichlet boundary conditions. Neumann boundary conditions can also be used to represent the tectonic forces. These forces can be known at the well by using direct stress measurements or by measuring the well's ovalization. These data can then be used to find the set of Neumann boundary

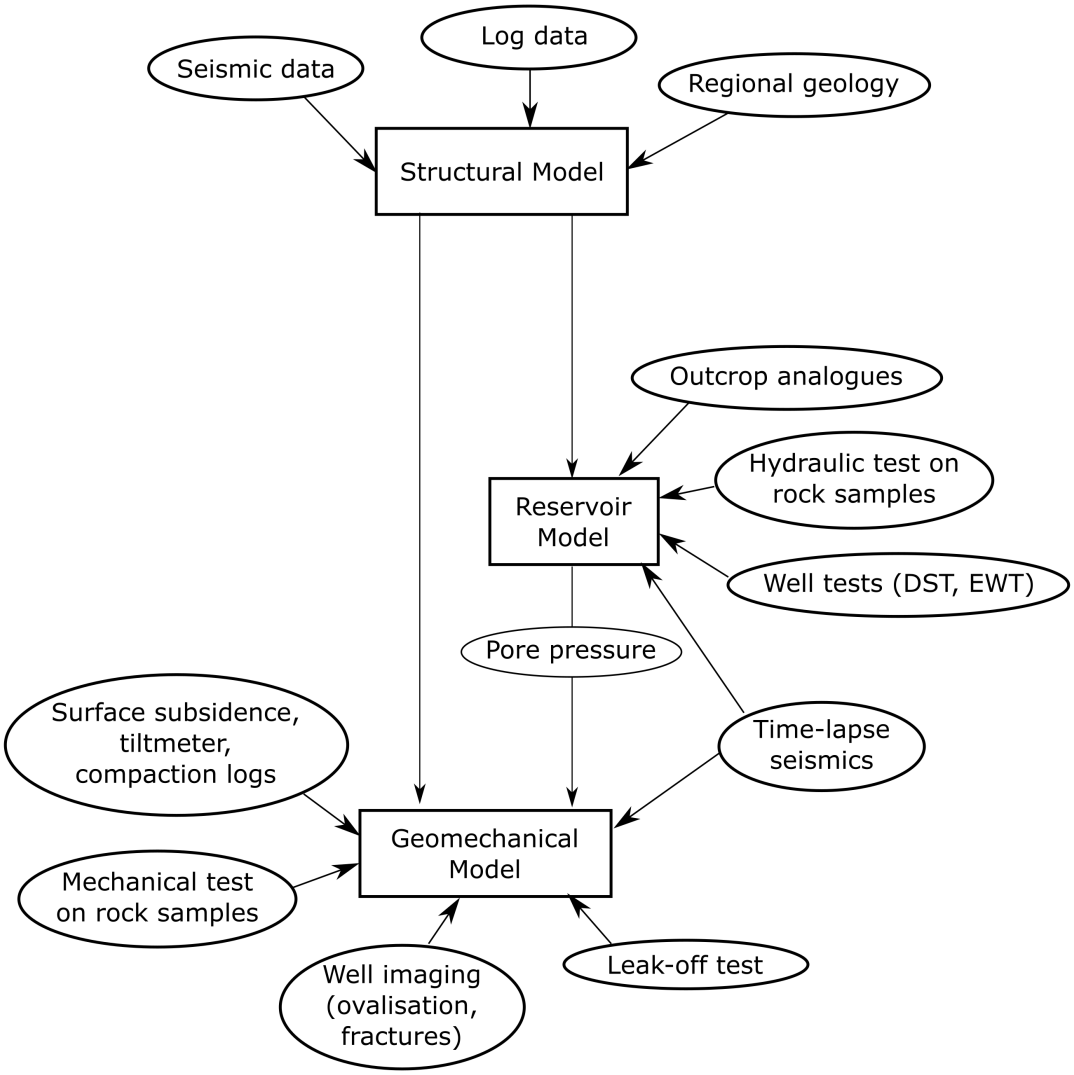


Figure 1.1: Geomechanical workflow

conditions that match the stress data at the wells (Mazuyer et al., 2018).

Finally, poroelastic equations can be solved. The poroelasticity model assumes that the rock skeleton behavior is purely elastic. However, there is no proof of such reversibility and inelastic effects may occurs. Cam-Clay model and viscoplasticity may be considered (Chan, 2004). The different steps and data used to build the geomechanical model are summarized in Figure 1.1.

#### 1.1.2.4 Coupling between the geomechanics and the reservoir fluid flow

Poroelastic equations show a close link between the fluid flow and the geomechanical model. Different methodologies are used to solve the coupled equations of the poroelasticity (fully coupled, partially coupled, one-way coupled—Longuemare et al., 2002). In the industry, flow equations and stress change are solved separately within two different software (one for the flow dynamics and one for the geomechanics). Because the numerical schemes used to simulate the fluid flow, the geomechanics are different and

the models do not cover the same region (the reservoir model covers the reservoir while the geomechanical model covers both the reservoir and the surrounding rocks), the discretization is different. As a coupled reservoir—geomechanical simulation is considered, a correspondence between pore pressure on the reservoir grid and on the geomechanical mesh is required. In the following, an exact correspondence between the pore pressure in the two models is not needed. The fluid flow is simulated first, and the resulting pore pressure change is inserted in the geomechanical model. A simple approach is to rasterize the pore pressure change of the reservoir grid then apply a smoothing filter to avoid sharp pore pressure change. Indeed, smooth pore pressure changes make the geomechanical simulation easier, as sharp pore pressure changes would require a thinner mesh and more computation time to obtain a similar result. The reservoir model can also be updated with the geomechanical results. When a fully coupled reservoir–geomechanical model is considered, the reservoir pore pressure is updated together with the geomechanical one Settari et al. (1998). Some studies consider a coupling of the permeability with the volumetric strain, which adds an extra coupling term (Rolando et al., 1997; Du et al., 2007).

#### 1.1.2.5 Optimization loop

Despite the numerous data available in the reservoir, the prediction made by the geomechanical model can be far from the reality. Backward optimization loops are now a standard procedure to better fit the monitoring data. Yet, the high degree of freedom and the large uncertainties of all successive models raise the questions of what can reasonably be changed and how far can one go in the different models.

### 1.1.3 Modelling the reservoir in plane strain condition

Linking the time-lapse seismic to the geomechanical model is a 3D problem because both the reservoir model and the time-lapse seismic attributes are computed in 3D. Nevertheless, geomechanical models are often performed in a 2D plane strain condition. Plain strain condition assumes that the model is infinite along the out-of-plane axis. Even if this hypothesis is not valid, 2D models are simple to build and provide a first approximation of the 3D solution.

Analytic solutions are known for some 2D elastostatic problems. These solutions can be used to predict the stress change for particular geometries in plane strain condition. This approach is interesting to derive the main mechanical parameters involved in a compacting reservoir.

#### 1.1.3.1 Analytical solution for a rectangular reservoir in a half-space

Analytical solutions can be found for simple elastostatic problems (see Nowacki, 1986; Kachanov et al., 2013). The rectangular reservoir in a homogeneous isotropic infinite space can be solved using the following "Airy stress function" method (Bower, 2009). The Airy potential is given by

$$\Phi = f_\Phi(x-L, z-B) - f_\Phi(x-L, z-T) - f_\Phi(x-R, z-B) + f_\Phi(x-R, z-T) \quad , \quad (1.11)$$

with

$$f_\Phi(x,z) = \frac{\eta p}{2\pi}\left(xz\log(x^2+z^2) - 3xz + x^2\arctan\frac{z}{x} + z^2\arctan\frac{x}{z}\right) \quad . \tag{1.12}$$

where $\eta$ is the poroelastic stress coefficient. It's physical meaning is developed in Appendix A.

The stress changes are related to Airy potential by

$$\sigma_{xx} = \frac{\partial^2\Phi}{\partial z^2} \quad , \tag{1.13}$$

$$\sigma_{zz} = \frac{\partial^2\Phi}{\partial x^2} \quad , \tag{1.14}$$

$$\sigma_{xz} = -\frac{\partial^2\Phi}{\partial x\partial z} \quad . \tag{1.15}$$

For the considered Airy stress function, this gives

$$\sigma_{xx} = \frac{\eta p}{\pi}\left[\arctan\left(\frac{x-L}{z-B}\right) - \arctan\left(\frac{x-L}{z-T}\right) - \arctan\left(\frac{x-R}{z-B}\right) + \arctan\left(\frac{x-R}{z-T}\right)\right] \tag{1.16}$$

$$\sigma_{zz} = \frac{\eta p}{\pi}\left[\arctan\left(\frac{z-B}{x-L}\right) - \arctan\left(\frac{z-T}{x-L}\right) - \arctan\left(\frac{z-B}{x-R}\right) + \arctan\left(\frac{z-T}{x-R}\right)\right] \tag{1.17}$$

$$\sigma_{xz} = \frac{\eta p}{\pi}\log(r_1 r_2 r_3 r_4) \tag{1.18}$$

where

$$r_1^2 = (x-L)^2 + (z-B)^2 \tag{1.19}$$

$$r_2^2 = (x-L)^2 + (z-T)^2 \tag{1.20}$$

$$r_3^2 = (x-R)^2 + (z-B)^2 \tag{1.21}$$

$$r_4^2 = (x-R)^2 + (z-T)^2 \tag{1.22}$$

We can verify that $\sigma_{xx} + \sigma_{zz} = -2\eta p$ inside the rectangle defined by $L$, $R$, $B$, and $T$ and $\sigma_{xx} + \sigma_{zz} = 0$ outside. The solution is plotted in Figure 1.2.

Mindlin (1936) proposed a method to express the stress fields in a half-space given the stress fields in an infinite space. In the half-space domain, the stresses can be written as a function of the stresses obtained for the infinite space $\boldsymbol{\sigma}^{(\infty)}$, and the "mirror" stress $\bar{\boldsymbol{\sigma}}^{(\infty)}(x,y,z) = \boldsymbol{\sigma}^{(\infty)}(x,y,-z)$ such as

$$\sigma_{xx} = \sigma_{xx}^{(\infty)} + (3-4\nu)\bar{\sigma}_{xx}^{(\infty)} - 4\nu\bar{\sigma}_{zz}^{(\infty)} + 2z\frac{\partial\bar{\sigma}_{xx}^{(\infty)}}{\partial z} \tag{1.23}$$

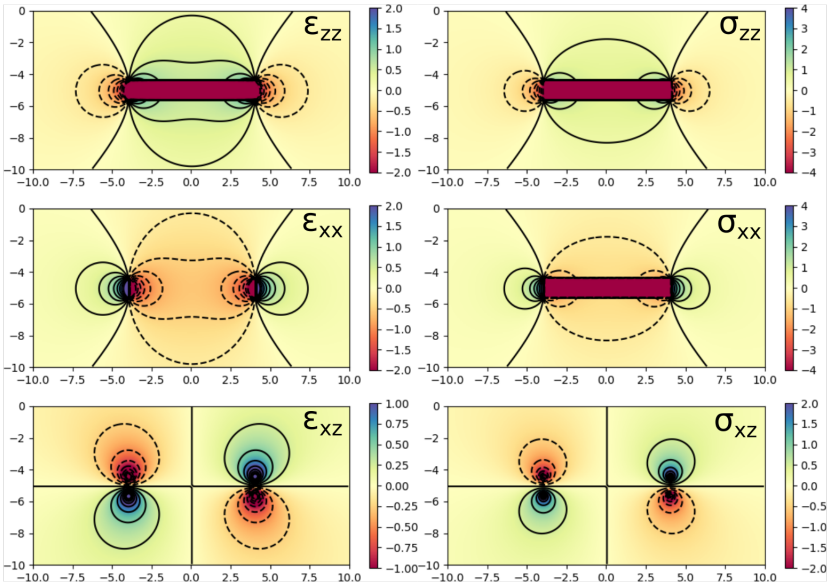


Figure 1.2: Strain and stress change for a rectangular reservoir in an infinite space. The strain components are without unit and stress components are in GPa. The Poisson's ratio is 0.3 and the pore pressure change is taken to -1 GPa. The stresses are computed using the strain and a Young modulus of 1.8 GPa

$$\sigma_{zz} = \sigma_{zz}^{(\infty)} - \bar{\sigma}_{zz}^{(\infty)} + 2z\frac{\partial \bar{\sigma}_{zz}^{(\infty)}}{\partial z} \tag{1.24}$$

$$\sigma_{xz} = \sigma_{xz}^{(\infty)} - \bar{\sigma}_{xz}^{(\infty)} - 2z\frac{\partial \bar{\sigma}_{xz}^{(\infty)}}{\partial z} \tag{1.25}$$

The strain and stress change for a rectangular reservoir in an half-infinite space are plotted in Figure 1.3.

#### 1.1.3.2 Numerical stress change computation with the finite element method

In the previous part, the reservoir has the same elastic properties as the surrounding rocks. The analytic solution shows that stress change is mainly deviatoric in the reservoir's surroundings. Chang and Conway (1969) used an analytical method to describe the stress change for a rectangular reservoir with an elastic properties contrast between the reservoir and the surrounding rock. However, the solution is complex to implement. To pursue the stress analysis, the finite element method is used. This numerical method is convenient because it can solve various reservoir geometries and heterogeneities in the elastic properties can be introduced easily.

In the following section, the stress changes is studied in rectangular reservoir with a Young modulus ratio (defined as the reservoir Young modulus divided by the surrounding rock Young modulus). The effect of such a Young modulus contrast is studied in Figure 1.4. The Figure 1.4A presents the volumetric part of the stress in the reservoir and around when the Young modulus of the reservoir is the same as the Young modulus around it. We can see that the stresses change are mainly isotropic in the reservoir.

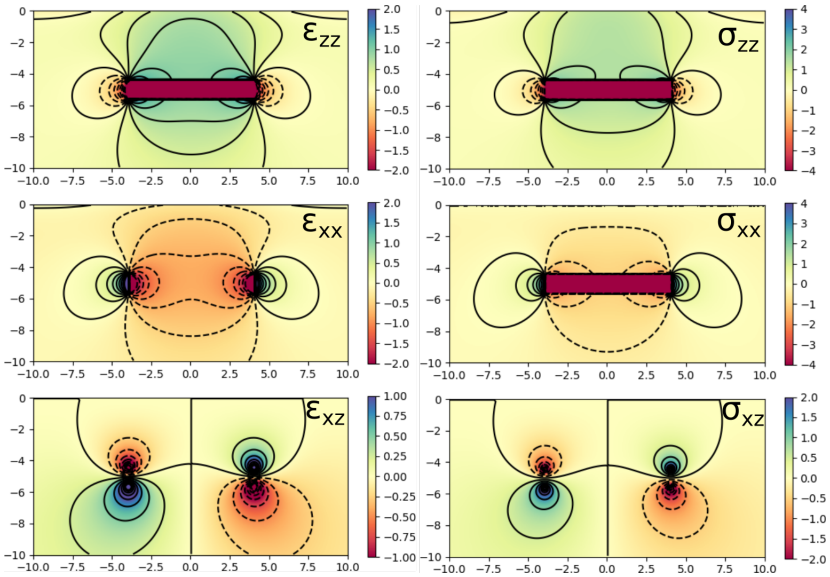


Figure 1.3: Strain and stress change for a rectangular reservoir in an half-space. The elastic properties and the pore pressure change are the same than in Figure 1.2.

Around the reservoir, the stress change are mainly deviatory, and no significant volumetric change can be observed. When a Young modulus contrast of 10 is applied (the reservoir Young modulus is 10 times smaller than the Young modulus around it—Figure 1.4B), the volumetric part of the stresses around the reservoir is significant. We can observe a dilative part above and upper the reservoir and a compacting part on the sides of the reservoir.

The finite element solution for a rectangular reservoir can be compared to the analytic solution when the Young modulus ratio is equal to 1 (Figure 1.5). This comparison is influenced by several approximations made by the finite element solution. Firstly, the finite element method can only be applied in a finite domain, while the solution we are looking for lies in an infinite domain (half-space). Secondly, it solves the equilibrium equations on a mesh, thus the solution depends on the mesh. Theoretically, refining the mesh leads to a better estimation of the real solution, but this tendency cannot be observed because of the limited domain. Thirdly, the analytical solution shows that the stresses are infinite at the corner of the rectangle reservoir. These singularities are not handled in the finite element method because the basis functions can only handle finite values. The solution is improved when the mesh is refined close to the corners.

In mechanics, singularities (points where the stress is infinite) is a well-known phenomenon whenever cracks are considered. This is problematic for the finite element method. It is also a problem when comparing the vertical strain with the time-lapse time strain because of the infinite quantities close to the reservoir while the time-lapse inversion constrains the time strain to be smooth. This issue can be solved by smoothing either the sharp reservoir boundaries or the introduced reservoir pore pressure change. Nevertheless, the high sensitivity of the reservoir geometry and the pore pressure change make it difficult to relate them quantitively to time-lapse velocity changes. As the reservoir geometry influences have a strong influence on the stress change close to it, an erroneous reservoir picking can have a strong influence on the predicted stress changes. This

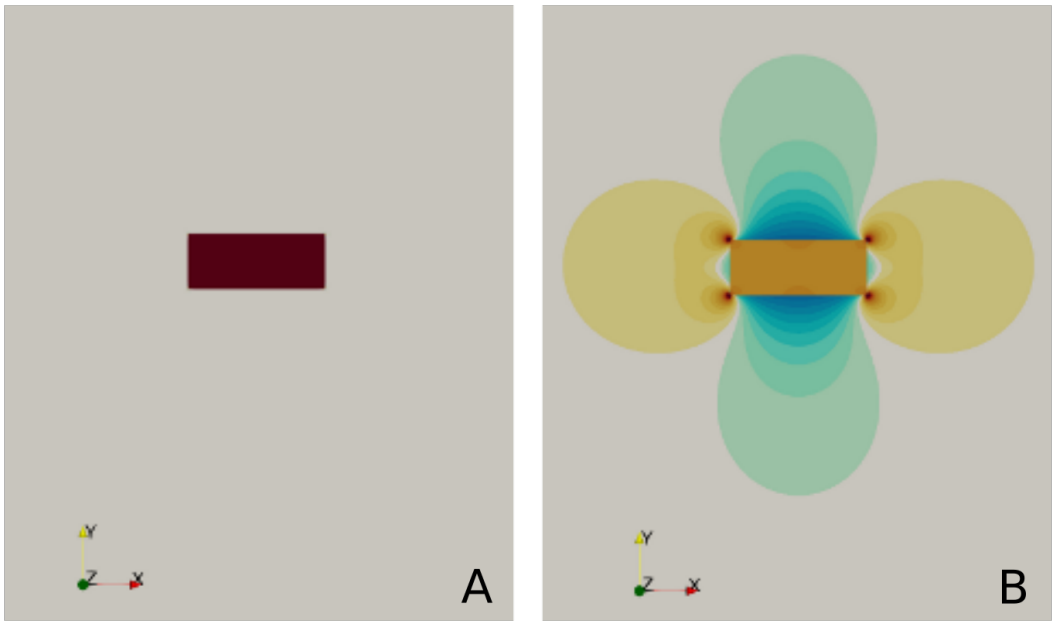


Figure 1.4: Volumetric stress for a rectangular inclusion computed with the finite element method. (A) Volumetric stress with the same Young modulus in the reservoir and in the surrounding rock. (B) Volumetric stress with a Young modulus in the reservoir 10 times smaller than in the surrounding rock.

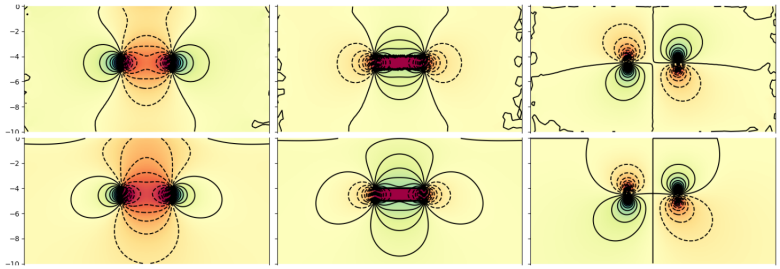

Figure 1.5: Comparison of the strain computed with the finite element method (first line) and with analytical solution (second line). The three rows corresponds to the three strain components $\varepsilon_{xx}$, $\varepsilon_{zz}$, and $\varepsilon_{xz}$. The main differences are for the values close to zero.

problem is attenuated for the upper part of the overburden which is at a far distance from the reservoir.

## 1.2 Time-lapse seismic monitoring

During the oil and gas field production, repetitive seismic acquisitions are performed to monitor the reservoir and the surrounding rocks. The seismic image before the production is called the base. At regular time steps, additional seismic acquisitions are shot: these seismic images correspond to the monitors. Different attributes characterizing the evolution of the seismic image can be measured, such as the traveltime difference (time-shifts), the phase and the amplitude changes of reflected seismic energy.

### 1.2.1 State of the art

Among the numerous field monitoring techniques, time-lapse seismic is now common in the oil and gas industry. The Arco oil and gas field marked the beginnings of time-lapse monitoring as an enhanced oil recovery (EOR) method (Greaves et al., 1983). Three seismic surveys were taken during a 15-month period, during the in-situ combustion. The results show a measurable amplitude change at the top of the Holt Sands (reservoir top) which extends laterally during the combustion propagation (Greaves and Fulp, 1987).

Since then, the improvement of seismic data processing has helped the development of seismic monitoring. In the North Sea, the offshore fields with chalk reservoirs (e.g. Ekofisk field—Key et al., 1998; Valhall; South Arne; Dan; Tyra) and high-pressure high-temperature fields (e.g. Elgin and Franklin—De Gennaro et al. (2008); Shearwater, Skua, Egret, Heron, Kirstin) have been extensively monitored using time-lapse seismic. The processing of the monitoring data shows evidences of reflectors travel-time differences (time subsidence at the top of the reservoir of 10 ms in Ekofisk field—Guilbot and Smith, 2002; 23 ms for the Valhall field—Hall et al., 2002). Since the first North Sea time-lapse studies, this phenomenon has been reported for many fields (MacBeth et al., 2019). Overburden time-shifts are surprising because time-lapse methods were originally developed to monitor the fluid flow in the reservoir, not the mechanical change in the overburden.

Significant efforts have been made to understand the time-lapse seismic effect of compacting reservoirs. The geometrical deformation of the reflectors and the velocity change potentially induces measurable time-shifts. The first one is due to the reservoir compaction and the overburden stretching. The second one is associated with the fluid substitution (Gassmann substitution), the porosity change, and the rock damaging. Thus, the interpretation of time-shits is ambiguous because one does not known which part of the time-shift is due to the strain and which part is due to the velocity change. Retrieving the physical phenomenon is even harder. Landrø and Stammeijer (2004) propose two methods for resolving this ambiguity. The first one measures the travel-time changes in pre-stack seismic data and the other one uses travel-time and impedance changes in stacked seismic data. However, their method is limited to isotropic horizontal layers and requires high quality pre-stack gathers for both surveys. To link the time-shifts to the velocity change, it is preferable to work with the derivative of the time-shifts,

the time strain. As this derivative is sensitive to time-shifts noise, Rickett et al. (2007) developed a nonlinear inversion designed to retrieve smooth time strains. In most cases, the overburden is affected by a positive time strain above compacted area which can either be interpreted as a velocity decrease or an increase of the layer thickness, but the ambiguity remains.

### 1.2.2 Evidence of velocity change in the time-lapse seismic data

The traveltime differences between a monitor and the baseline are called the time-shifts. There are a 4D parameters often used in the context of compacting reservoirs. Indeed, in this context studies show that measurable time-shifts are observed due to both the reservoir compaction and the overburden time-shifts. This traveltime difference is decomposed into the geometrical deformation (reservoir and overburden layers thickness changes) and the velocity change. For instance, in the reservoir, the substitution of oil and gas by water induces an increase in the velocity. On the contrary, the measured reservoir time subsidence shows evidence of an elastic wave velocity decrease in the overburden which is associated to the rock damaging. For a given layer of thickness $z$ and velocity $v$, Landrø and Stammeijer (2004) expressed the time-shifts $d\tau$ due to a small change in length $dz$ and a small change in velocity $dv$ as

$$\frac{d\tau}{\tau} = \frac{dz}{z} - \frac{dv}{v} \quad . \tag{1.26}$$

Time-shifts are due the accumulation of small velocity change along the seismic path. The integrative property of these parameters makes it difficult to observe the different layer contribution in term of velocity change. This differential form of the time-shifts involves the quantity $\frac{d\tau}{\tau}$, which is called the time strain. Figure 1.6 presents some North Sea fields where the overburden time-shifts are significant.

Equation 1.26 is only valid for a vertical ray travelling in a homogeneous elastic medium. Nonvertical rays allow to study the time-shifts angle dependence in prestack time-lapse seismic data. Røste et al. (2006) use both zero-offset and offset dependent time-shifts to discriminate between layer thickness and velocity related changes. However, their method is very sensitive to the time-lapse anisotropy changes. "Uncertainty in estimated thickness change and velocity changes becomes severe when the changes in anisotropic parameters exceed 1%" Røste et al. (2006).

## 1.3 Towards a stress-dependent rock-physics model

### 1.3.1 Predicting vertical velocity changes using the geomechanical model

The vertical strain can be computed from the geomechanical model presented in section 1.1.3 but the velocity change is more complex to estimate. Indeed, geomechanical simulations are performed in linear elasticity, so the elastic coefficients remain constant. Nevertheless, time-lapse seismic data are explained by a velocity change, which means that the elastic properties or the rock density vary. The density change is not enough in term of magnitude to explain the velocity change and goes in the wrong direction

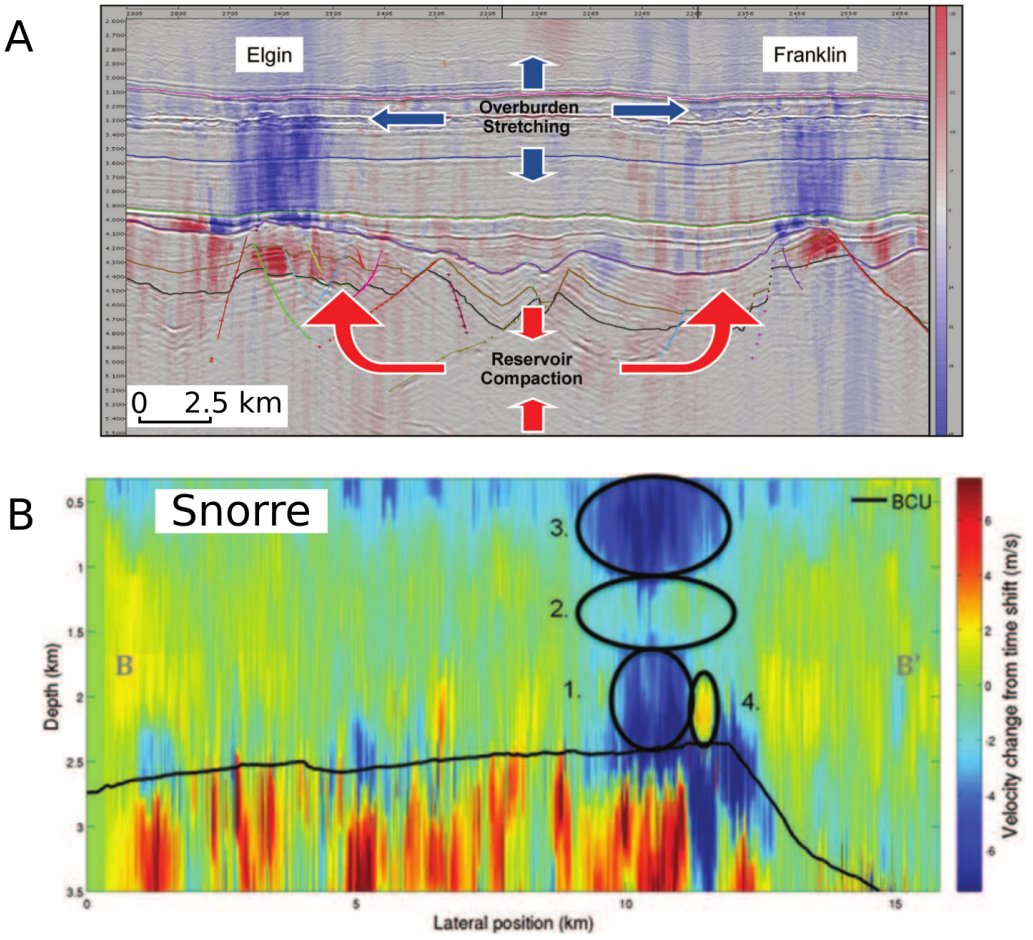


Figure 1.6: Overburden time-shifts observed in several studies. (A) Time-strain measured at the Elgin/Franklin North Sea HPHT fields, extracted from De Gennaro et al. (2008). (B) Velocity change map computed from the time-shifts at the Snorre field, extracted from Røste et al. (2015).

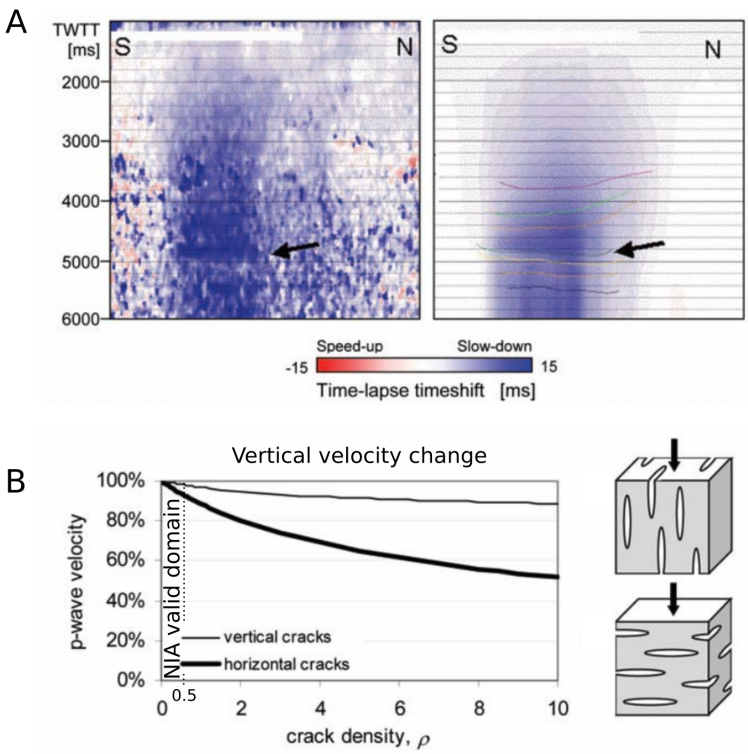


Figure 1.7: (A) The similarity between the time-lapse time-shifts (left) and the geomechanical strain (right) leads Hatchell and Bourne (2005) to propose the $R$–factor model. (B) Hatchell and Bourne (2005) proposed a micromechanical model base on cracks to explain the overburden time-shifts. The horizontal cracks have a stronger influence on the vertical velocity than the vertical cracks model.

(compacting rock becomes denser, so the elastic waves should propagate slower). In fact, elastic properties change is the main component of the elastic velocities change. Thus, to explain the velocity change, nonlinear behavior law is needed (nonlinear elasticity, irreversible compaction or damaging, viscous behavior, friction contact...).

Hatchell and Bourne (2005) and Røste et al. (2006) propose that the vertical velocity change is proportional to the vertical strain with proportionality coefficient (dilatation factor $\alpha$ or $R$–factor, with $\alpha = -R$) such as

$$\frac{\Delta v}{v} = -R\varepsilon_{zz} \quad . \tag{1.27}$$

The $R$–factors are estimated on each layer by comparing the vertical velocity change measured in the time-lapse seismic data and the vertical strain resulting from the geomechanical simulation. These factors are difficult to estimate everywhere because of uncertainties in both the time-lapse inversion results and the geomechanical strain. MacBeth et al. (2018) review the different values (in compacting and stretching areas) obtained in various fields. A large difference is noticed between $R$–factors measured in the reservoir (less than 2) and $R$–factors measured in the overburden (typically between 4 and 9). As far as rocks are concerned, this difference is understood mechanically with the dissymmetry between compressional and extensional behavior in mechanical tests. Indeed, rocks are known to be more fragile in traction than in compression. Neverthe-

less, MacBeth et al. (2018) write that "geomechanical simulations do not predict this observational asymmetry". They propose to introduce two $R$–factors, $R^+$ for extensive areas and $R^-$ for compressive areas. The equation 1.27 is still valid but the proportionality factor $R$ differs depending on the region (compressive or extensive). These two parameters can be defined for the reservoir and the overburden layers, but only one is measured because the stress regime is not complex enough. The stress regime is compressive in the reservoir and extensive in the overburden, with some compressive parts at the edge of the reservoir. Thus, instead of measuring 4 $R$–factors (two in the reservoir and two in the overburden), the stress change due to reservoir compaction allows for the measurement of only two of them ($R^+$ in the overburden and $R^-$ in the reservoir).

| Field | $R^+$ (overburden) | $R^-$ (reservoir) | Reference |
|---|---|---|---|
| Valhall | 4–9 | <2 | Hatchell et al. (2005) |
| Ekofisk | 4–10 | 2 | Janssen et al. (2007) |
| Ekofisk | 7–22 | 16 | Wong and MacBeth (2016) |
| Dan | 4–6 | | Hatchell et al. (2007) |
| Holstein | 5–10 | <1 | Ebaid et al. (2009) |
| Shearwater | 4–6 | 1–3 | Van Bergen et al. (2013) |
| Mars | 4–8 | <2 | Hatchell and Bourne (2005) |
| Shearwater | 20–35 | <2 | Staples et al. (2007) |
| Elgin–Franklin | 7 | | Hawkins et al. (2007) |
| Elgin–Franklin | 20–100 | | De Gennaro et al. (2008) |
| Snorre | 20 | | Røste et al. (2015) |
| Genesis | 5 | | Hodgson et al. (2007) |
| Statfjord | 15 average | | Røste and Ke (2017) |

Table 1.1: $R$–factors reported from various fields. Adapted from MacBeth et al. (2018) with some minor corrections.

The $R$–factor is widely used in the industry because of its simplicity. But this apparent simplicity hides many assumptions. The geomechanical model is much simplified:

- Linear isotropic elasticity: The geomechanical simulation is performed in linear elasticity with isotropic elastic properties. However, the subsoil is not an isotropic material at reflection seismic resolution. It can consist of some layered rocks that are considered transversely isotropic (VTI or HTI) or fractured rocks that can be considered orthotropic. Furthermore, in time-lapse seismic data, the velocity change occurs both in the reservoir and in the overburden. In the latter, it can only be understood as a change in the elastic properties due to the stress change. Thus, the material is nonlinear.

- Poroelastic behavior of the reservoir: Two-way coupling between the reservoir fluid flow and the geomechanical model is rarely performed. Indeed, the pore pressure change of the reservoir fluid flow simulation is generally used to infill the geomechanical model. This one-way coupling adds uncertainties in the pore pressure, as the reservoir fluid flow simulation does not consider the rock elastic

response. The uncertainties in the stress change are also affected by the error in the pore pressure. Furthermore, when nonlinear elasticity or nonelastic (e.g. plasticity or viscoplasticity) model is considered, the stress change depends not only on the final pore pressure but the pore pressure history.

- Vertical strain: The stress change around the reservoir is known to be anisotropic. Holt et al. (2018) point out that R-values depend on the stress path (a measure of the stress anisotropy). In practice, only the vertical strain is considered in equation 1.27, and the non-vertical strain components are ignored.

The time-lapse inversion assumes that only vertical velocity change is measured. Indeed, the time-lapse time-shifts are measured in the migrated stack of the base and the monitor, and the conversion of these time-shifts into a velocity change requires to consider a virtual vertical ray. Edgar and Mastio (2017) show that this assumption can lead to misposition of the velocity change anomalies. Horizontal stress changes may also play an important role in the velocity change (Tura et al., 2005; Røste et al., 2006).

The $R$-factor assumes a linear relationship and the same model is used regardless of the rock facies:

- Reservoir lithologies change, but the same simple law is still used in every situation. Laboratory tests on rock samples show that the mechanism associated to rock compaction is very diverse depending on the rock type. For example, sandstones show compaction band and grain crushing (Fortin et al., 2006, 2007). The carbonates' porosity is driven by the pore aspect ratio which is driven by the diagenesis (Fournier et al., 2014). Shales are known to have an intrinsic anisotropy; thus, an anisotropic rock-physics model should be used (Wang, 2002). Restricting the link between geomechanics and the time-lapse seismic with a one parameter law implies that the $R$–factors average various physical and geological realities.

- The relationship between the velocity change and the effective stress change is linear only for a limited range of effective stress change. Laboratory experiments shows that the velocity change on rock due to stress change is complex and can increase the velocity (closing cracks) but can make suddenly the velocity decrease (grain crushing). In time-lapse seismic, the velocity change is measured between the base and the monitor, which can be spaced of several years. We may not see the phase where the velocity in the reservoir decreases due to grain crushing.

Because of these assumptions, the $R$–factor model is not a rock-physics model. $R$–factors do not measure intrinsic properties of the rocks, but they are fitting parameters. They contain anisotropic information (Fuck et al., 2009; Herwanger and Horne, 2009) and stress path dependent features (Holt et al., 2018).

Herwanger points out that the $R$–factor model is easy to use because it is a 1–parameter model and it allows to link the time-shifts due to changes in layers thickness and velocity. Nevertheless, this approach does not allow to consider the changes in triaxial stress state because it would require retrieving the velocity change anisotropy. Moreover, the $R$–factors retrieved in time-lapse studies (R=4–6) are different from those measured in laboratory (R around 100). This major issue is still an unsolved problem. The $R$–factor is widely used in the industry for its simplicity, but it suffers from the lack

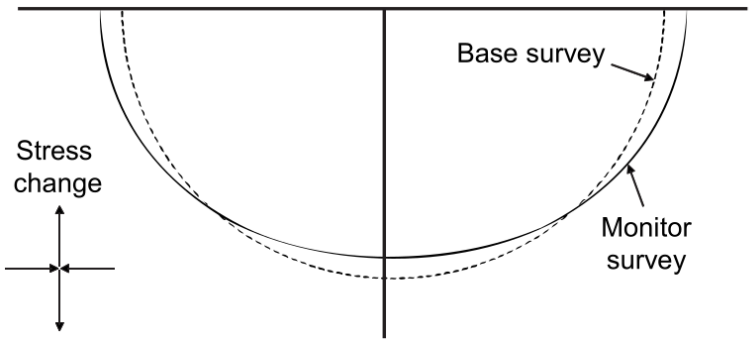


Figure 1.8: Waveforms of the base survey and the monitor survey in the overburden based on the predictions of the velocity change anisotropy according to Herwanger and Horne (2008). The stress change in the overburden is assumed to be deviatoric, with a streaching along the vertical direction and compressive along the horizontal plane. The velocity change corresponds to a decrease in $\alpha$ and increase in $\delta$ and $\varepsilon$ (where $\delta = \varepsilon$) in terms of Thomsen parameters.

of an inherent rock-physics model. Despite the numerous field cases using this model, the geomechanical time-lapse signal is not fully understood yet (MacBeth et al., 2018).

### 1.3.2 Nonlinear elasticity

Nonlinearity is a common effect in rock elasticity. Indeed, stress-strain relations under a loading (uniaxial or triaxial) is curved. In term of wave propagation, the nonlinear elasticity predicts a stress-dependent velocity and frequency effects, which are not seen with linear elasticity. Nonlinear elasticity predicts that the wave velocity depends not only on the lithology by also on the lithostatic stress. Thus, we can use to understand the time-lapse velocity change due to stress change.

In a first approach, we consider the 'third-order' elastic coefficient as a proxi for estimating the velocity change. In a second approach, heterogeneities, such as or penny-shaped cracks or spheroidal cavities, are introduced in the rock, and effective elastic theory is used to predict the equivalent properties of such materials.

#### 1.3.2.1 'Third-order' elastic coefficients

'Third-order' elastic coefficients have been used to understand the velocity change observed in time-lapse seismic data (Herwanger and Horne, 2009; Fuck et al., 2009). This theory assumes that the rock is elastic, which means that it is only valid for small stress change (Winkler and McGowan, 2004). The application range can go up to hundreds of MPa for unconsolidated and 10-20 MPa for consolidated rocks. At higher stress where inelastic deformation occurs, the theory is no longer valid (Sun and Prioul, 2010).

'Third-order' elasticity is an extension of the linear elastic theory to include finite deformation in elastic isotropic material. Murnaghan (1937, 1951) defined three additional elastic parameters $m$, $n$, and $l$ which characterize the material nonlinearity. The parametrization is, of course, non-unique and several authors propose alternative parametrization (Toupin and Bernstein, 1961; Bland, 1969; Eringen et al., 1975; $A$, $B$, and $C$—Landau and Lifshits, 1987). Many 'third-order' elastic coefficients are ac-

cessible in the literature (see e.g., Gupta, 1973; Bonner, 1974; Lockner et al., 1977; Carmichael, 2017). The mathematical development of this theory motivates the laboratory measurements of these three nonlinear constants for rocks. For example, Hughes and Kelly (1953) proposed to perform velocity measurements under hydrostatic pressure and uniaxial condition to access these constants.

In our case, we use the 'third-order' elastic coefficients accessible in the literature to predict the velocity change due to a vertical strain. Murnaghan (1937) wrote the longitudinal velocity as

$$\rho_0 v_P^2 = \lambda + 2\mu(2l + \lambda)\theta + (4m + 4\lambda + 10\mu)\varepsilon_{zz} \quad . \tag{1.28}$$

The longitudinal velocity is elliptical and it depends on two 'third-order' elastic coefficients, here $l$ and $m$. Other expressions can be found in the literrature. For instance, Takahashi and Motegi (2015) express the velocity change induced by a static uniaxial loading $T_{11}$. For longitudinal waves, the velocity change takes the form

$$v_{ij} = v_0(1 + \alpha_{ij}\frac{T_{11}}{E}) \quad , \tag{1.29}$$

where the subscript $i$ corresponds to the propagation direction and the subscript $j$ to the polarisation direction. Then $\alpha_{11}$ and $\alpha_{22}$ correspond to the dilatation factor of Røste et al. (2006) or the opposite of the $R$–factor of Hatchell and Bourne (2005) for the vertical and horizontal velocity change considering a static uniaxial loading. They take the form

$$\alpha_{11} = \frac{1}{2(\lambda + 2\mu)}(5\lambda + 10\mu + 2l + 4m - 2\nu(\lambda + 2l)) \quad , \tag{1.30}$$

and

$$\alpha_{22} = \frac{1}{2(\lambda + 2\mu)}(\lambda + 2l - \nu(6\lambda + 10\mu + 4l + 4m)) \quad . \tag{1.31}$$

In the following, we considered that the strain is mainly vertical. Equation 1.28 is specialized for a vertical strain $\varepsilon_{zz}$ at constant volume ($\theta = 0$). The same formula can be founded by taking $\nu = 0.5$ in equation 1.30. Using $\nu = 0.5$, two $R$–factors ($R_V$ and $R_H$) which represent the vertical and the horizontal velocity change due to a vertical strain can be expressed as

$$R_V = -\frac{5}{2} + \frac{\lambda}{2(\lambda + 2\mu)} - \frac{2m}{\lambda + 2\mu} \quad , \tag{1.32}$$

and

$$R_H = -\frac{2\lambda + 5\mu + 2m}{2(\lambda + 2\mu)} \quad . \tag{1.33}$$

We can see that the $R$–factors depends only on one 'third-order' elastic coefficient $m$ and the elastic properties $\lambda$ and $\mu$.

Herwanger and Horne (2009) also used the third-order elastic coefficients to express the $R$–factor. They only expressed the vertical $R$–factor ($R_V$), and they found

$$R = -\frac{1}{2}\frac{c_{111} - c_{112}}{C_{33}} \quad . \tag{1.34}$$

Using the relations $C_{33} = \lambda + 2\mu$ and $m = \frac{1}{4}(c_{111} - c_{112})$, we can see that their formula is a simplified version of the equation 1.32, where the term of the velocity change induced by density change is ignored. Indeed, numerical applications shows that the velocity change induced by density change is small compared to the velocity change induced by the nonlinear elastic effect. In addition, published values for $c_{111}$ and $c_{112}$ show that $c_{111}$ is larger than $c_{112}$. Herwanger and Horne (2009) claimed that the term $c_{112}$ can be neglected (as he also neglect the horizontal strain).

To obtain some numerical results on these $R$–factors, we use the laboratory data of Winkler and Liu (1996) and Winkler and McGowan (2004). Winkler and Liu (1996) performed laboratory tests to measure the 'third-order' elastic coefficient for different porous rock in dry and water-saturated condition. They use the Landau parameters to express the nonlinear elastic coefficients. We use the following formula to convert them into Murnaghan coefficients:

$$m = \frac{1}{2}A + B \tag{1.35}$$

where $A$ and $B$ are Landau coefficients (Landau and Lifshits, 1987).

We compute the associated $R$–factors are calculated and the values are reported in Table 1.2.

| Rock | $K$ (GPa) | $G$ (GPa) | $m$ (GPa) | $R_V$ | $R_H$ |
|---|---|---|---|---|---|
| Berea Sandstone (A) | 4.1 | 4.5 | -3441.5 | 679 | -340 |
| Berea Sandstone (B) | 3.7 | 3.7 | -5541.5 | 1281 | -641 |
| Buff Sandstone | 9.9 | 9.5 | -3489.5 | 307 | -153 |
| Hanson Sandstone | 10.4 | 10 | -3806.5 | 318 | -159 |
| Limestone 1078 | 21 | 12.2 | -1349.5 | 70 | -30 |
| Limestone 1083 | 29.6 | 20.6 | -11299 | 394 | -197 |
| Massilon Sandstone | 6.1 | 6.3 | -14435 | 1989 | -994 |
| Portland Sandstone | 9.7 | 7.3 | -980 | 98 | -49 |
| Westerly Granite | 29.9 | 23.6 | -27262.5 | 886 | -443 |

Table 1.2: Physical properties of various rock samples found in Winkler and Liu (1996). Third-order elastic coefficients are translated into Murnaghan coefficient m. The two $R$–factors ($R_V$ and $R_H$) are derived from these properties.

Winkler and McGowan (2004) performed nonlinear acoustoelastic constant measurements on dry (Table 1.3) and water-saturated rocks (Table 1.4). Winkler and McGowan (2004) explain that water-saturated rocks stress-dependency velocity is not fully described by the 'third-order' elastic coefficient because of probable rock dilatancy. The third-order elastic coefficients are uncertain and the associated $R$–factor in Table 1.4 may not represent correctly the elastic properties stress-dependence. Winkler and McGowan (2004) think that this is due to local-flow dispersion and dilatancy and that this phenomenon may not exist at lower frequencies.

| Rock | Density (kg.m$^{-3}$) | $v_P$ (m/s) | $v_S$ (m/s) | $m$ (GPa) | $R_V$ | $R_H$ |
|---|---|---|---|---|---|---|
| Portland Sandstone | 2140 | 2190 | 1948 | -997 | 191 | -96 |
| Indiana Limestone | 2210 | 3730 | 2216 | -7615 | 493 | -246 |
| Berea 1 Sandstone | 2040 | 2051 | 1423 | -4198 | 976 | -488 |
| Berea 2 Sandstone | 2100 | 2644 | 1761 | -4256 | 577 | -289 |

Table 1.3: Physical properties of 4 rock samples studied by Winkler and McGowan (2004) in dry condition. Elastic properties are derived from ultrasonic velocities measurements.

| Rock | Density (kg.m$^{-3}$) | $v_P$ (m/s) | $v_S$ (m/s) | $m$ (GPa) | $R_V$ | $R_H$ |
|---|---|---|---|---|---|---|
| Portland Sandstone | 2330 | 3234 | 1726 | -2491 | 202 | -101 |
| Indiana Limestone | 2390 | 4216 | 2166 | -14995 | 704 | -352 |
| Berea 1 Sandstone | 2280 | 2841 | 1340 | -3822 | 413 | -207 |
| Berea 2 Sandstone | 2310 | 3230 | 1855 | -18315 | 1518 | -759 |

Table 1.4: Same physical properties than in Table 1.3 but in wet condition. Winkler and McGowan (2004) explain that the third-order elastic coefficients cannot be trusted "since the underlying model appears inadequate".

The $R_V$ and $R_H$ are opposite in sign and the magnitude of $R_H$ is about half of the magnitude of $R_V$. These $R$–factors means that we can expect a vertical velocity decrease and an horizontal velocity increase in the overburden. This is in agreement with the Herwanger and Horne's prediction on the velocity change anisotropy in the overburden.

#### 1.3.2.2 Elastic effective models

Rocks are known to have heterogeneity such as cracks and pores. Considering these observed heterogeneities using a mechanical approach allows to model and predict some rock elastic behaviors. For example, Walsh (1965a) express the compressibility pressure-dependence of porous material for two special cases, the spherical pores, and the narrow cracks. His crack model allows to predict the hysteresis in the strain-stress curves observed in laboratory test on rock sample and the fact that the ultrasonic elastic properties are higher than the static ones (Walsh, 1965b). Models introducing partial gas saturation (gas coming out of solution) predict an increase (20%) in the velocity for seismic frequencies (White, 1975).

Kachanov (1980, 1992) identified two crack density tensors ($\alpha$ and $\beta$) as microstructural parameters to describe the effective elastic properties. For dry rocks, the effective properties are well modelled by the tensor $\alpha$. The elastic properties of dry rocks are influenced by an 'elliptic' type of orthotropy (characterized by four independent elastic constants). The properties are not sensitive to a change in the crack aspect ratio and the limit case of penny shaped cracks can be considered. The second tensor plays an important role for fluid-filled or closed sliding cracks. The presence of fluid in the rock breaks the orthotropic symmetry and the crack aspect ratio must be considered. Guéguen and

Kachanov (2011) plot the longitudinal elastic velocity anisotropy regarding the cracks orientation (vertical and horizontal) and the aspect ratio.

For laboratory tests on rock samples, effective models have shown their interest. Fortin et al. (2007) model the effects of pore collapse and grain crushing in sandstones with a model of spherical pores and randomly oriented cracks. They use the non-interaction approximation to relate the microstructural parameters (porosity, crack density and crack aspect ratio) to the effective bulk and shear moduli. Ultrasonic velocity measurements of P-waves and S-waves are performed to estimate the effective bulk and shear moduli and to predict the microstructural parameters evolution. In the water-saturated case, they manage to retrieve the evolution of the crack aspect ratio.

The effective elasticity of fluid-saturated rocks with cracks and pores depends on the ratio between the rate of loading and the rate of fluid diffusion in the rock. While wave speeds in dry rocks are controlled by static effective elastic properties, the wave speeds on saturated rocks depends on the wave frequency. Borgomano (2018) shows two characteristic frequencies (the cutoff frequency $f_1$ of the drained/undrained transition which can be predicted under Biot theory from the permeability $\kappa$, the drained bulk modulus $K_D$, the fluid viscosity $\eta$, and sample's length $L$, $f_1 = 4\kappa K_D/\eta L^2$, and the cutoff frequency which corresponds to the time needed to equilibrate the fluid pressure between neighboring cracks by local squirt flow).

Because of the various permeabilities of the rock and the different range of elastic wave frequencies used to investigate the subsurface (seismic wave and ultrasonic laboratory measurement), the velocity change retrieved in time-lapse seismic or in laboratory test do not refer to the same elastic properties in the case of a water-saturated rock. We can distinguish two limit cases of rock, clay with a low permeability and sands with a high permeability:

- In clay, the elastic property change are mainly due to pore pressure change. This can be modelled by the poroelasticity with undrained compliance. In undrained condition, no macroscopic fluid flow can possibly take place as the clay permeability is very low. The undrained compliances can be measured under any conditions where there is not enough time for the macroscopic flow to occur, and yet enough time for local flow to occur (at the REV scale). The seismic waves see the same undrained compliance than the mechanical test in laboratory. But, if wavespeed measurements are performed at ultrasonic frequencies, typical of laboratory experiments, the REV is not isobaric. In such a situation, ultrasonic waves measure unrelaxed compliances, which are different from the undrained compliances (Guéguen and Sarout, 2009).

- In sands, the fluid can flow easily. Poroelasticity models this behavior with the drained condition. The drained compliances are measured in the laboratory on samples that are deformed at constant fluid pressure and they can be measured on dry rock samples. For a seismic wave, the characteristic time of the pore pressure diffusion ($\tau$=$l^2/2c$=2.5 $10^5$ s, with characteristic distance $l$=50 m and diffusivity $c$=$10^{-2}$ m.s$^{-2}$) must be compared to the wave period (20 ms for a wave frequency of 50 Hz) to know if the wave measured drained or undrained compliance. As the diffusivity is generally low for sandstone, the seismic wave measures the undrained

compliance. But the drained compliance must be used for the mechanical model as the characteristic time of the overburden is in days (8,64 $10^4$ s in one day).

#### 1.3.2.3 *R*–factors derived from effective model

*R*–factors can be predicted with various rock-physics models derived from microstructures. The first model consists in measuring the influence of the pore size on the vertical velocity $v$. This model can be parametrized by the porosity $\Phi$. The *R*–factor derived from this model can be written as Terzaghi hypothesis.

$$R_A = -\frac{1}{v}\left(\frac{\partial v}{\partial \Phi}\right)(1-\Phi) \tag{1.36}$$

where $\frac{\partial v}{\partial \Phi}$ is known experimentally (e.g. Mavko et al., 2019). The range of value for R lies between 1 and 3 (Hatchell and Bourne, 2005). Røste et al. (2015) give the range of values for chalk (1.5), sand (1.6–2.4) and clay (2.7–3.6).

The Xu and White (1995) model allows to consider the aspect ratio change of the sand and clay pores. The *R*–factor derived from this model can be written as

$$R_B = \left(\frac{\partial v}{\partial \alpha_{\text{sand}}}\alpha_{\text{sand}} + \frac{\partial v}{\partial \alpha_{\text{clay}}}\alpha_{\text{clay}}\right)\frac{1-\Phi}{\Phi} \quad . \tag{1.37}$$

MacBeth et al. (2018) use this model to estimate the *R*–factor and they find values between 1 and 3 for porosities between 0 and 20%. We can observe that the *R*–factor increase a lot when the porosity decreases.

Ultrasonic velocity measurements along triaxial stress paths along three directions (0°, 45° and 90°) have been performed for shales (e.g., Holt et al., 1996; Dewhurst and Siggins, 2006; Pervukhina et al., 2008; Sarout and Guéguen, 2008; Delle Piane et al., 2011; Sarout et al., 2014). Shale samples varied from soft to stiff shales, from dry to wet and further fully saturated shales. Holt et al. (2018) combined the laboratory tests on shales in undrained conditions and the simulated overburden stress changes to estimate the time-lapse vertical P-wave velocity change. The ratio between horizontal change $\gamma_h$ and vertical stress change $\gamma_v$, defined as the stress path $\kappa = \frac{\gamma_h}{\gamma_v}$, depends on the reservoir shape and the elastic contrast between the reservoir and the surrounding rock. They observe that the pore-pressure change depends linearly on the stress path as predicted by the Skempton's law. They use Skempton's parameters $A_S$ and $B_S$ to express the *R*–factor for shales as

$$R = \left\{\left(\frac{a}{3} + b - A_S B_S c\right) + \left[\frac{2a}{3} - b - B_S(1-A_S)c\right]\kappa\right\}\frac{E_V}{1-2\nu_{VH}\kappa} \tag{1.38}$$

where $a$, $b$, and $c$ are three parameters which can be determined with three experiments with different stress path and there are expressed in $Pa^{-1}$. In the overburden, the stress change is mainly deviatoric. This implies that $\gamma_v + 2\gamma_h \approx 0$ i.e. $\kappa \approx -0.5$. Note that this *R*–factor depends on the linear properties of the rock $E_V$ and $\nu_{VH}$.

#### 1.3.2.4 Cracks

MacBeth et al. (2018) consider *R*–factors for various crack distributions: random hor-

izontal cracks ($R_{C1}$), isotropic cracks distribution ($R_{C2}$), vertical cracks randomly distributed along horizontal planes ($R_{C3}$), and vertical cracks ($R_{C4}$). MacBeth et al. (2018) proposes to use the time-shifts offset-dependence to estimate which model should be considered. Indeed, the anisotropic velocity change induce by these model is different, and the two parameters retrieved by the time-shifts (the zero-offset time-shifts and the time-shift gradient) could potentially be inverted for more information than just only the crack density. Nevertheless, these $R$–factors ($R_C$s) are only valid for dry rocks. Guéguen and Kachanov (2011) show that the velocity change anisotropy differs a lot when water-saturated rocks are considered.

# Chapter 2

# EnKF for time-lapse seismic data assimilation

**Contents**




**Abstract** In the oil and gas industry, field characterization involves several geosciences disciplines such as geology, geophysics, geomechanics or reservoir engineering. To confront the various data types, we use 4D seismic and geomechanics data linked by the $R$–factor attributes to predict synthetic time strains with a geomechanical model. We consider inverting the reservoir pore pressure to provide a geomechanical model which matches the time-lapse seismic data. The proposed workflow can help building more consistent models.

## Résumé du Chapitre 2

La loi empirique du R-factor est communément utilisée dans l'industrie pétrolière pour calibrer les modèles géomécaniques à partir de données de sismiques 4D. Néanmoins, la prédiction des effets 4D à partir du modèle géomécanique peut être en désaccord avec les résultats d'inversion 4D. Ce désaccord nous motive à proposer un workflow dans lequel les paramètres du modèle géomécanique sont modifiés, afin d'avoir une meilleure cohérence entre ce modèle et les données issues de l'inversion 4D. Le filtre de Kalman d'ensemble est utilisé afin de mettre à jour la pression des pores. Les données 4D ainsi prédites par le modèle du R-factor sont plus proches des résultats d'inversion 4D. Néanmoins, la carte du changement de la pression des pores obtenue n'est pas réaliste vis-à-vis de l'écoulement des fluides. Cela suggère que le modèle d'écoulement ainsi que la hauteur utile doivent être pris en compte dans notre workflow.

## 2.1 Introduction

The prediction power of geomechanical models is strongly limited by the large uncertainty of the input parameters used to infill the model. Whereas the structural part is relatively well defined (the seismic interpretation provides accurate position of the surface limits where the seismic illumination is sufficient) the mechanical parameters used for the geomechanical simulations as well as the boundary conditions are strongly dependent on the man's art and are subjected to large uncertainties.

Geomechanical model have a high potential to understand 4D seismic data. In the industry, several workflows have been propose to integrate 4D seismic as a constrain to the geomechanical model (e.g. De Gennaro et al., 2008). Indeed, the $R$–factor model can be used to relate the vertical strain to the time-strain measured within time-lapse seismic inversion. De Gennaro et al. (2008) proposed a workflow to match the synthetic and the time-strain through a least squares approach using the elastic coefficients of the geomechanical model as parameters (Figure 2.1). While this workflow provides a simple approach to integrate time-lapse seismic data into the geomechanical model building, this approach suffers from several shortcomings:

- The amplitude of the time-shifts/strains in the 4D seismic images are subject to noise and strongly depends on the parameterization and regularization used for the 4D inversion (Thore, 2015). 4D seismic data are thought to provide good qualitative data such as the arching effect location but a quantitative inversion may also propagate noise into the geomechanical model.

- The amplitude of the synthetic time-shifts/strains are directly proportional to the $R$–factor used in the rock-physics model.

Using mechanical parameters as inversion parameters in seismic time-lapse problems would change the amplitude but not the shape of the stress-strain state. To overcome this limitation, a new approach is introduced which has benefited from the evolution of the technology in terms of both 4D inversion (Thore and Edgar, 2017) and algorithm (EnKF—Evensen, 2003). We propose an application on real/synthetic data that were created based on the same real data as used by De Gennaro et al. (2008).

## 2.2 Test data

The data used for the workflow comprises inverted 4D seismic data using an internal algorithm modified from Williamson et al. (2007) in the sense that it inverts for constant values for each layer on a trace to trace basis (with lateral correlation) (Figure 2.2A). The chosen seismic section goes through the main anomaly observed in the time-lapse inversion results. The layers used to constrain the time-lapse inversion correspond to those used for the geomechanical model (Figure 2.5). The advantage of using this layer-constrained inversion is that stabilizes the inversion by drastically reducing the number

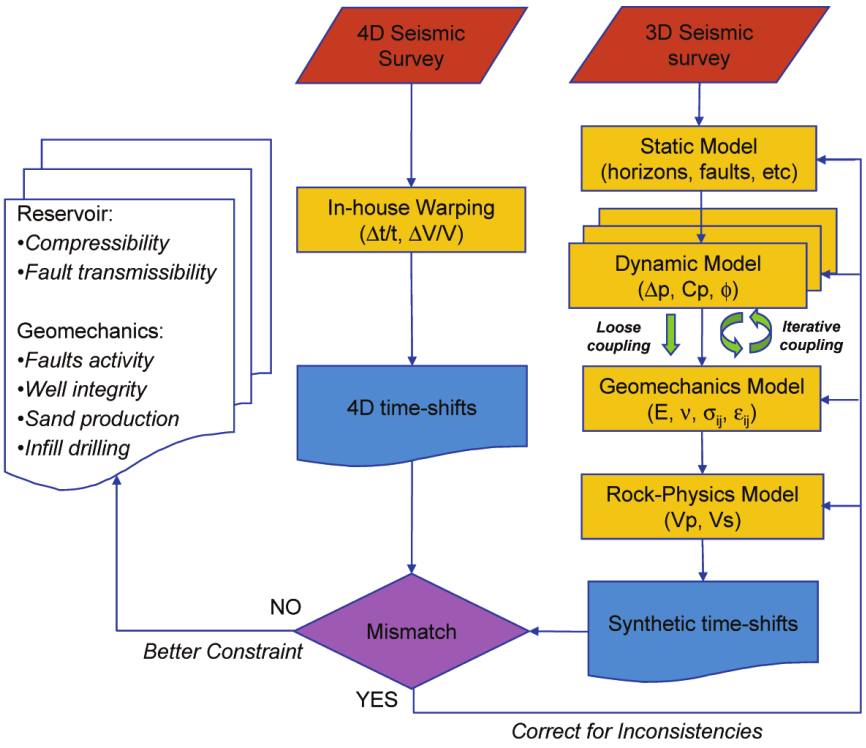


Figure 2.1: Workflow proposed by De Gennaro et al. (2008). The in-house warping technique corresponds to the one developed by Williamson et al. (2007). The static model corresponds to the structural model and the dynamic model to the reservoir model. $C_p$ stands for the pore compressibility where $\frac{\Delta t}{t}$ are the time strains and $\frac{\Delta V}{V}$ is the velocity change. The geomechanical model is updated accordingly to the mismatch between the 4D time-shifts and the synthetic time-shifts. This optimization loop can be performed by updating the static model (add new horizons or faults), update the dynamic model which is the reservoir properties, update the geomechanical model which is the elastic properties and the in-situ stresses, or updating the rock-physics model which correspond to the law which translate the rock properties and oil saturation into seismic wave velocities ($V_P$ and $V_S$).

of parameters as well as creating less dependency to the regularization weight (Thore, 2015; Thore and Edgar, 2017) on the other hand. As the time-strains are constant within a layer in each trace and time-strain discontinuities from one layer to the next are not penalized in the inversion (e.g. the cap rock to the reservoir), this time-lapse inversion algorithm is designed to highlight the mechanical effect in each layer of the overburden. To compare the geomechanical vertical strain to the time-strains obtained by the inversion, the time-strains are converted into depth using the PSDM velocity field tied to the wells.

The time-strains measured at the reservoir location are a mixture of fluid and mechanical effects. They are difficult to measure in each individual layer, so a single reservoir layer is used in the 4D inversion. The reservoir compaction, which varies according to the reservoir geology, the pore pressure change, the Biot's coefficient, and the NTG also produces time-strains. Therefore, the measured time-strains in the reservoir are not used in the inversion process. Only the overburden time-strains are used to invert reservoir properties.

The geomechanical model (Figure 2.5) is built using interpreted horizons and mechanical parameters corresponding to the "best knowledge" available at that time. The model is discretized using triangular mesh which is refined around the reservoir (Figure 2.6). The initial conditions (base time) for the pressure field and at the monitor time are obtained from the flow simulator.

### 2.2.1 Measuring the $R$–factors

The transformation of the simulated vertical strains into time-strains is performed using the $R$–factor. The procedure used to determine the $R$–factor is described in the following.

We first consider the option of picking a judicious area where the vertical strain is the strongest in the layer and therefore the 4D signal is expected to be most reliable. $R$ is calculated on each triangle of this area saying:

$$\text{if} \quad \frac{dt}{t} * \varepsilon_{zz} > 0 \quad \text{then} \quad R = \frac{\frac{dt}{t}}{\varepsilon_{zz}} - 1 \quad , \tag{2.1}$$

and the final value of $R$ is taken to be the mean or the median value over the selected triangles. The problem with this approach is that the calculated values of $R$–factor changes significantly with the shape and the position of the chosen area and is thus quite subjective.

The values of the $R$–factors are in any case much higher than expected. It is commonly admitted that $R^+$ values should oscillate between 3 and 10 and that $R^-$ should be smaller than $R^+$, but we found R values higher than 150 in layers containing seismic anomalies. The median method regarding this problem was the most effective since the resulting $R$–factors are smaller than the other method in every layer. Nonetheless, the problem of the $R$–factor calibration is not so important in our case because, as shown below, we have been retrieving the shapes of the arching effect rather than the amplitudes of the mechanical stress.

### 2.2.2 Setting the problem

Figure 2.2B shows the simulated vertical strain converted into time-strains (to be compared to Figure 2.2A). They exhibit 3 main differences (noted 1 to 3 on Figure 2.2):

- (1) corresponds to a negative anomaly on the 4D time-strains which can be questionable, is it real or an artefact/noise of the 4D inversion? It is situated right below the maximum time-strain amplitude anomaly and could be an artifact of layering effect which tends to compensate over estimated values in one layer by an opposite value in the next layer.
- (2) corresponds to the position of the arching effect seen on the 4D time-strains to be compared with the one observed on the synthetic time-strains. It is a very strong marker of the geomechanical effect and the shift indicates that the model is not correct.
- (3) is the position of the maximum 4D time-strains is anomalic. It is shifted towards the right on the synthetic time-strains. This mismatch indicates again that the model is not compatible with the observed data.

Because of the uncertainty of the time-lapse inversion, we think that the time strain shape is more valuable information than the absolute magnitude of the time strain. Following these observations, we only consider changing the pore pressure in the reservoir compartments and keeping the mechanical parameters unchanged. Indeed, sensitivity analysis has shown that changing the mechanical parameters would be inefficient since it would have an impact on the magnitude of the anomalies rather than on their shapes while changing the source term in the reservoir (the product of pore pressure, net-to-gross, and Biot's coefficient) has a major impact. Also, as mentioned above, the absolute values of the amplitude of the synthetic time-strains are directly related to the values of the $R$–factor which are not reliable. We consider that the mapping of vertical strain to the synthetic time-strains amplitudes is performed once for good by the $R$–factor.

## 2.3 Inversion process

### 2.3.1 Ensemble smoother

To perform the reconciliation, we use a technique adapted from Assisted History Matching: the Ensemble Smoother (ES). This technique is an ensemble-based method which considers on one hand an ensemble of model realizations representing the uncertainties of the model (in our case an ensemble of reservoir pressure changes in the different panels of the reservoir) and on the other hand an ensemble of realizations of the observations (the time-strains) representing the uncertainties on the data.

ES is derived from the Ensemble Kalman Filter (EnKF—Evensen, 2003) which is a stochastic approach of the Kalman Filter. The basic idea of the EnKF is that the distribution of the state is represented using a collection of state vectors, called an Ensemble.

The method is popular because it relies on simple conceptual formulation and it implementation is simple as it does not require derivation of Jacobian matrices. Instead,

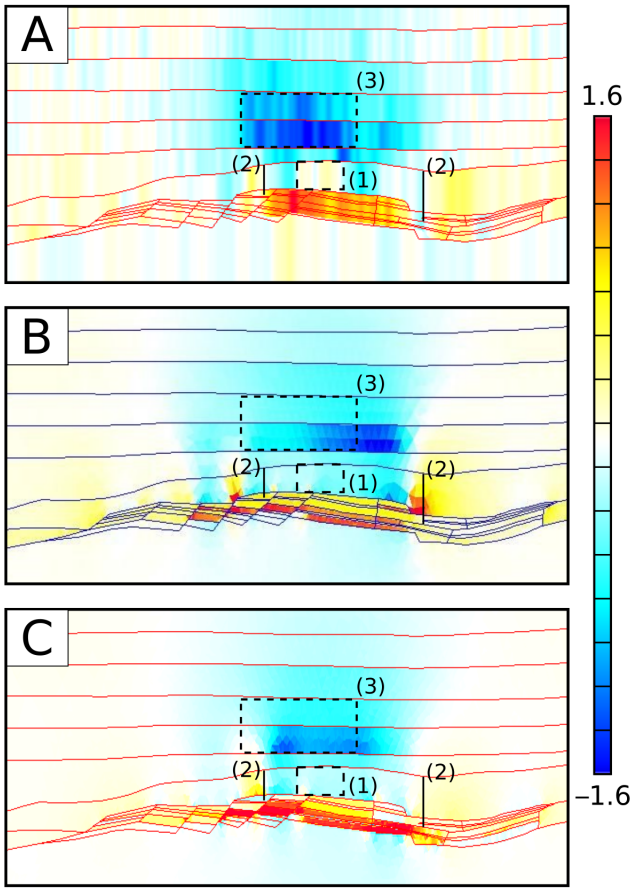


Figure 2.2: Time-strains maps of the studied case (in %) (A) Time-strains obtained by time-lapse seismic inversion. (B) Synthetic time-strains predicted by the initial geomechanical model. (C) Synthetic time-strains predicted by the updated geomechanical model using the ensemble smoother.

the Covariance Matrix between state parameters and observation variables (which is basically a heavy calculation) is approximated thanks to the $N$ realizations. This trick lighten significantly the calculation.

The method starts with an initial guess of the model space statistic. We generate $N = 100$ ensemble members $x_i \in R^n$ using Monte Carlo simulation. This is represented in a matrix formulation as

$$X = (x_1, x_2, \ldots, x_N) \in R^{n \times N} \quad . \tag{2.2}$$

First, the mean of the ensemble members $\bar{X}$ is computed and the ensemble perturbation matrix is computed as

$$X' = X - \bar{X} \quad . \tag{2.3}$$

The covariance matrix $C \in R^{n \times n}$ between the ensemble members $x_i$ is

$$C = \frac{X'(X')^T}{N-1} \quad . \tag{2.4}$$

The measurements $d_i \in R^m$ are defined as the perturbation of a measurement $d$

$$d_i = d + \epsilon_i \tag{2.5}$$

Uncertainty $\epsilon_i$ is synthetically generated with Monte Carlo simulation. The higher the uncertainty is on a value, the less this value will drive modification in the starting ensemble.

Similarly, to the ensemble member's matrix, the perturbed observation is represented in a matrix form

$$D = (d_1, d_2, \ldots, d_m) \in^{m*N} \quad , \tag{2.6}$$

while the introduced perturbation is stored in

$$D' = (\epsilon_1, \epsilon_2, \ldots, \epsilon_m) \in^{m*N} \quad . \tag{2.7}$$

The measurement error covariance matrix is then

$$E = \frac{D'(D')^T}{N-1} \quad . \tag{2.8}$$

In our case, we consider that uncertainties on data values are not correlated so $E$ is a diagonal matrix composed by the uncertainty variance on each data point.

The ensemble members' covariance matrix and the measurement error covariance matrix are used to perform a Monte Carlo approximation of the Kalman filter

$$K = CH^T(HCH^T + E)^{-1} \quad , \tag{2.9}$$

and it is used to do a Bayesian update of the ensemble members

$$X^a = X + K(D - HX) \quad . \tag{2.10}$$

This method can be used to assimilate information on either linear or weakly nonlinear systems. In the nonlinear case, the operator $H$ cannot be expressed as a matrix.

Instead, it is considered as a black box and we only use the vector $HX$ which represents the predicted data. This vector takes the form

$$HX = (f(x_1), f(x_2), \ldots, f(x_N)) \quad , \tag{2.11}$$

where f represents the nonlinear forward operator) and the Kalman gain is computed as

$$K = X'(HX')^T(HX'(HX')^T) + (N-1)E)^{-1} \quad , \tag{2.12}$$

where

$$HX' = HX - H\bar{X} \quad . \tag{2.13}$$

Two terms contribute to the Kalman gain. Firstly, the term $X'(HX')^T$ corresponds to the correlation between the model ensemble and the predicted data ensemble. It allows to measure the sensibility of the predicted data regarding a change in the model parameters. Secondly, the inverse of $HX'(HX')^T + (N-1)E$ is called the innovation (or pre-fit residual) covariance. This term balances the measurements accuracy and the state accuracy. When the magnitude of $E$ is small, meaning that the measurements are accurate, the state estimate depends mostly on the measurements. When the state is known accurately, then the transposed of $HX'(HX')$ is small compared to $E$, and the filter mostly ignores the measurements relying instead on the prediction derived from the previous state.

### 2.3.2 Inversion procedure

As explained above the chosen state variables (i.e. parameters to invert) are the pressure changed in each of the 56 panels of the reservoir. We have used the nominal pressure as given by the flow simulator for the mean and large variations around it for the variability to produce the initial model ensemble of 100 models. For each ensemble member, we calculate the associated synthetic vertical strain using the geomechanical finite element simulation, the $R$–factor law converts the synthetic vertical strains into synthetic time strains. The data consist of the time-strain values in each triangle of the model in the caprock and the overburden. The reservoir is left out because, as mentioned above, the 4D measurements are quite uncertain and the effect in the reservoir is not a pure geomechanical effect. The workflow is illustrated in Figure 2.3.

We introduce an uncorrelated uncertainty in the 4D time strains with 100% in the reservoir and the underburden, a medium value in the caprock and in the layer with the strongest anomaly and a weak value elsewhere.

### 2.3.3 Results

The results in the data domain are shown on Figure 2.2C. The inversion procedure can modify the shape of the stress field in such a way that the synthetic time-strains match in a much better way the 4D time-strains at least in the cap-rock and the overburden part of the model where the data are active.

The questionable anomaly (1) was not corrected by the inversion procedure: the parameterization used did not provide enough freedom to perform such a strong variation. This tends to confirm this anomaly as a 4D inversion artifact. The inconsistencies

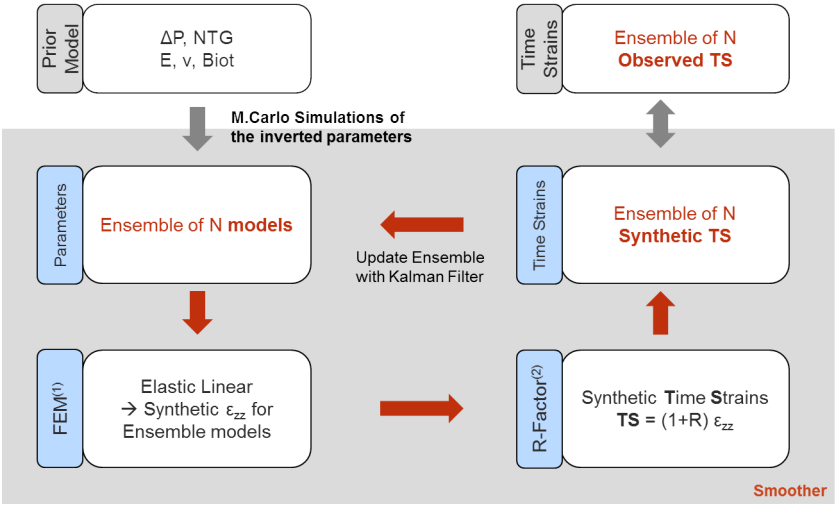


Figure 2.3: Our proposed workflow. This workflow is a simplified version of the one proposed by De Gennaro et al. (2008) presented in Figure 2.1. We only address the update of the geomechanical model properties

(2) have been greatly diminished by the inversion procedure and the arching limits of the 4D signal and the model are quite compatible. In the shale layers, the 4D limits is not precise (the 4D signal is quite weak) but its positioning observed on the synthetic time-strains is relatively sound. In any case, according to Saint-Venant's principle, the diffusive equation of the mechanics does not permit a precise localization of the strain far from the source. The inconsistency (3) is also reduced. The positioning of the maximum synthetic time-strains and of the time-lapse time-strains is more consistent although not totally satisfying. One can observe that the magnitude of the synthetic time-strains is weaker than that of the prior and that of the time-lapse time-strains. As stated above we do not see that as a problem since the absolute amplitude of the synthetic time strains is only qualitatively with the $R$–factor value.

Figure 2.4 shows the results in the model space (the pore pressure). The inverted depletion is significantly different from that of the prior model. The inversion particulary suggest that the pressure change is not as high in most of the central panels as the Flow Simulation model suggested. This suggests, since the pore pressure change is supposed to be well-known in these panels, that another reservoir parameter such as the NTG probably needs to be modified (the mechanical effect is actually the result of the product of three terms: the NTG, the pore pressure change, and the Biot's coefficient). Moreover, the extension of the depletion is disminished on the top right of the reservoir with an important decrease of depletion (50%). On the contrary, the extension of the reservoir depletion on the bottom right is larger than in the prior model.

To be more consistent with the prior information, another inversion has been performed in which the reservoir panels investigated by the wells are fixed to the theoretical value. The results obtained are not as good and, therefore, the pressure changes in the panels investigated by the wells should not be interpretated as pressure change but rather as an indication that the Biot coefficient or the NTG are different that those set in the model.

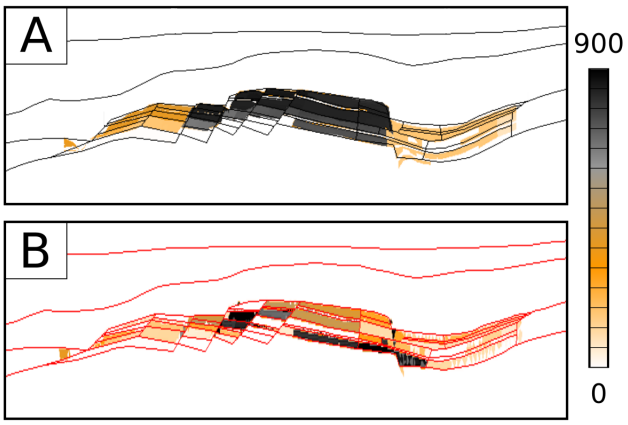


Figure 2.4: Pore pressure change in the compartmentalized reservoir in bar. (A) Pore pressure change in the prior model. (B) Pore pressure change resulting from presented workflow.

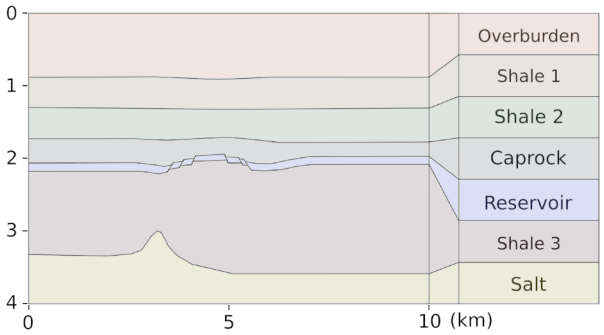


Figure 2.5: Simplified model used in the noise sensitivity analysis. The overburden and the underburden layering are similar to the case study. The reservoir compartmentalization is simplified compared to the case study.

## 2.4 Noise sensitivity analysis

We now study the sensitivity of the inversion to the noise data information. For that we built synthetic data on a simplified model with only 7 reservoir compartments by setting the "truth" as a given value for the depletion (Figure 2.7A).

Time-lapse time-strains are generated using a geomechanical model and the $R$–factor. To analyze the sensitivity of the noised time-lapse time strains data, we generate three different noised versions of the synthetic time-lapse time-strains, from a low noised to highly noised. In the measurement error covariance, we assume that we do not know the noise magnitude in the data (it may be estimated in a real case, but we want to observe the transition between under-assimilation to over-assimilation). We choose $E$ to be a diagonal matrix where the diagonal coefficients are $E = \frac{\epsilon^2}{N-1} I_m$ where $\epsilon$ correspond to the assumed measurement error. During the ES iterations, we decrease $\epsilon$ which has the effect of assimilating more data in the ensemble members. As the ensemble members are generated using a Gaussian law, we plot the members ensemble mean and standard deviation at each iteration of the ES on the Figure 2.8A–C.

For the low noise case (1% noise add in the data) presented in Figure 2.8A, the pore

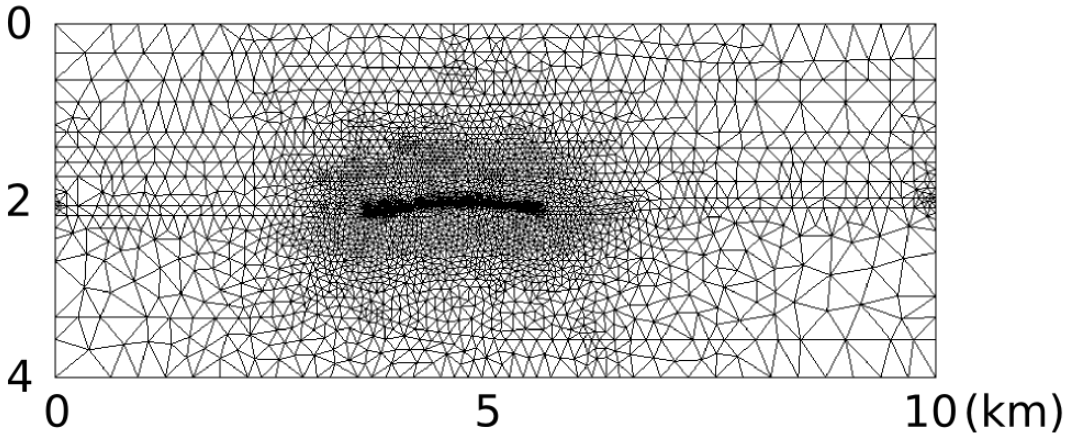


Figure 2.6: Triangular mesh of the simplified model. The mesh is refined in and around the reservoir.

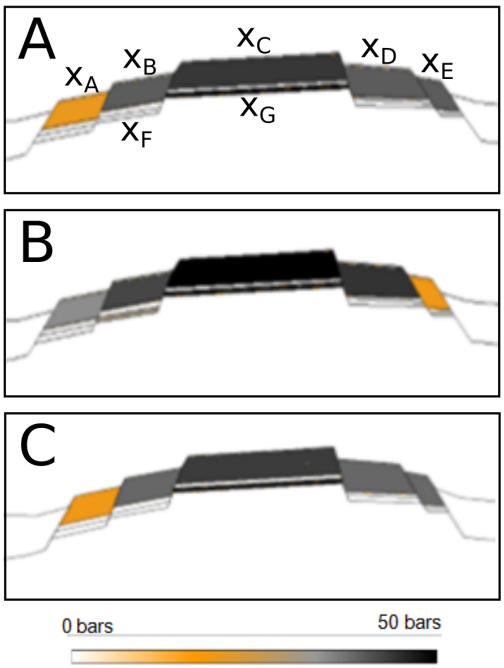


Figure 2.7: Pore pressure change in the simplified model. 7 compartments are considered where the pore pressure change is parametrized by $x_A$, $x_B$, $x_C$, $x_D$, $x_E$ and $x_F$. (A) Pore pressure change in the true model. This pore pressure change is used to computed the true time-strain which we want to match. (B) Prior pore pressure change. (C) Pore pressure change inverted with the ensemble smoother in the low noise case.

pressure means evolves smoothly over the iterations. The standard deviation of $x_A$ to $x_E$ decrease from the first iteration while the standard deviation of $x_F$ and $x_G$ starts to decrease from the 10th iteration. For the mean values, $x_A$ to $x_E$ stabilize around the 20th iteration and $x_F$ and $x_G$ begin to evolve at the 10th iteration and are stable during the last iterations. $x_A$ to $x_E$ are found first with a good accuracy and once there are found, $x_F$ and $x_G$ can be determined. The standard deviation shows that $x_A$ to $x_E$ are less sensitive to noise than $x_F$ and $x_G$. In other word, $x_A$ to $x_E$ are the main parameters which determine the time strains matches.

For the second case (10% noise add in the data) presented in Figure 2.8B, the mean of the ensemble members has a similar behavior than in the low noise case. The standard deviation has a similar behavior until the 20th iteration. Then, the standard deviation decrease slowdown and then increase. The mean values of the ensemble members are well retrieved but the high standard deviation shows that the value of $x_F$ and $x_G$ are uncertain.

The last case is a very noised case (noise of the same magnitude as the data—Figure 2.8C). We can observe a similar behavior than the second case, but the mean value evolves in a more complex way. After the 15th iteration, the standard deviation of $x_F$ and $x_G$ increase quickly and stagnate at the 22nd iteration and then increase slowly.

The values of the reservoir pressure are well retrieved despite the noise. We observe that the noise affects the ensemble standard deviation, but the ensemble mean is well retrieved with sufficient iteration of the ES. The explanation is that the Kalman gain provides an optimal solution when the noised introduced in the data follows a Gaussian law. In a real application case, the time-lapse seismic noise is not Gaussian. We cannot expect that the ensemble mean provides a reliable information of the reservoir if the ensemble standard deviation is high.

## 2.5 Conclusion

This workflow has demonstrated that it is mandatory to integrate geomechanics in the unified vision of an earth model. Indeed, the stress field in the overburden depends on the reservoir pore pressure. Therefore, it must be included in the set of data that should be used to constrain the model. Using a simplistic rock-physics model, 4D data can be translated into mechanical information and thus be used to this purpose. As the main driver for the match is the arching shape, an accurate rock-physics is not mandatory. We suggest that the pore pressure change can be reassessed and refined to build a fully consistent model. We do not believe that the solutions we give are truly reliable since the net-to-gross (NTG) plays also an important role. The ES used for the inversion procedure is shown to be efficient.

We propose some possible improvements of our method. Firstly, we have used as data the amplitude of the time-strain although we were trying to match shapes. This is not an optimal approach and the flow simulation assisted history matching community has proposed solution for that like the Mahalanobis distance. Secondly, the implementation is very basic since we have used the FEM as a direct solver. As an improvement, the superposition principle can be used and only the base needed for the

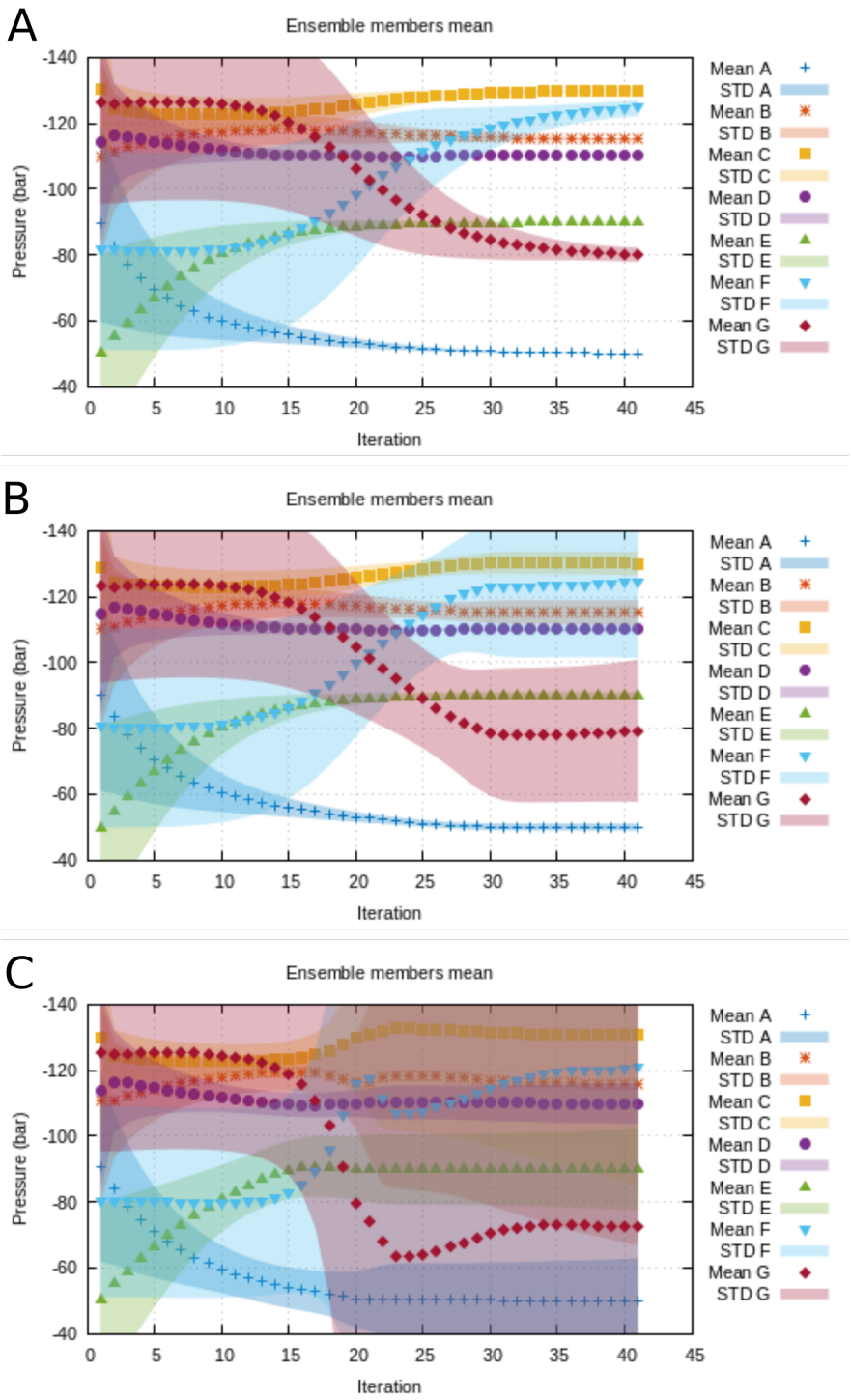


Figure 2.8: Inversion results of the ensemble smoother. Three different noise in the data have been introduced.

direct linear inversion. Finally, a reassessment and discussion with reservoir engineers could lead to a better understanding of reservoir behavior. Our workflow is focused on changing the mechanical parameters while the reservoir model is also riddled with uncertainties. Considering flow simulations constraints regarding pore pressure change predicted by time-lapse seismic data could improve the consistency between the models.

# Chapter 3

# In-situ stress inversion using well data and fault activation criteria

**Contents**




**Abstract** Mechanical simulations require not only the knowledge of the geometry and mechanical properties of the earth but also boundary conditions such as tectonic lateral forces. Boundary conditions are not accessible, and their estimation is difficult. It is possible to estimate equivalent forces by solving an inverse problem which consists in matching simulated stress with measured stress at given positions. Measured data are very expensive to acquire and therefore are sparse and fuzzy. We present a way of constraining the inverse problem by introducing geological/mechanical constraints: the yield criteria. For example, we can impose that a fault is active or not and by this way reduce the valid domain of boundary conditions. This kind of information is usually known by geologists (fault activity) or can be observed from plugs (fractures). We illustrate the workflow on a model based on a real data case.

This chapter is based on an oral presentation given at the EAGE Conference London 2019 (Thore et al., 2019).

## Résumé du Chapitre 3

Les simulations mécaniques requièrent non seulement la connaissance de la géométrie et des propriétés mécaniques de la Terre, mais aussi de l'ensemble des forces impactant le système telles que les contraintes tectoniques. Néanmoins, les conditions aux limites du modèle géomécanique ne sont pas accessibles et leurs estimations sont difficiles. De plus, les mesures de l'état de contrainte du sous-sol sont chères à acquérir, éparses et mal-comprises. L'activité des failles est habituellement connue par les géologues. Des fractures peuvent aussi apparaître au niveau des puits. Nous proposons d'utiliser ces informations pour estimer l'état de contrainte in-situ du sous-sol. Pour ce faire, les contraintes prédites par la simulation géomécanique sont harmonisées avec les mesures de l'état de contraintes en différentes positions. Un critère de rupture est utilisé afin de contraindre l'inversion tout en tenant compte de l'activité d'une faille. Par exemple, nous pouvons imposer l'activité d'une faille, et de ce fait, que l'état de contrainte le long de la faille se trouve sur le critère de rupture. Nous illustrons ce workflow sur un modèle inspiré d'un cas d'étude réel.

## 3.1 Introduction

In the oil and gas industry, the knowledge of the subsurface stress is of paramount importance. For drilling operation, the stress field is the key parameter which determines the mud weight envelope along the well path and impacts the number of casings required. If the pressure in the well is lower than the pore pressure, there are some risks of leak of the aquifer and the well can collapse. If the mud pressure is too high and reaches the fracture pressure, the mud will leak. For hydraulic fracturation, the in-situ stress conditions the crack orientation, thus the direction of larger permeability. This stress field always has a great impact on the well placement.

Modeling of stress state can be achieved through numerical simulations, generally using the Finite Element Method (FEM). In geomechanics, the models require not only the definition of the geometry of reservoir but also the knowledge of the mechanical properties of the surrounding rocks (the overburden up to surface and underburden to some extent). The model is infilled with mechanical properties whose complexity varies with the type of rheology chosen for the different rock-types (Herwanger and Koutsabeloulis, 2011). The modeling results depend not only on the model but also on the boundary forces that are applied to it. To correctly predict stresses and therefore explain the well ovalization or the reactivation of high-angle faults, the elastic properties and density heterogeneity must be defined, and also additional forces, such as the previous tectonic activity, must be considered.

Mazuyer et al. (2018) propose a workflow to introduce these unknown forces in a geomechanical model using stresses measurements at the wells. Their method shows a great potential to match the well stress data. Nevertheless, the Neumann boundary condition calculated to obtain this match lacks of physical sense, e.g., they obtain Neumann boundary condition in traction for some lithologies in a compressional tectonic environment. The inverted boundary conditions are only equivalent parameters that explain the data, adapted to the model and the chosen type of comportment laws. The goal of this paper is to generalize their approach by adding more constraints to the model and therefore to obtain a more precise and hopefully more realistic stress state.

## 3.2 Method

### 3.2.1 Mechanical data

Only a few stress data are available to constrain the mechanical model:

- Leak-off tests provide accurate measurement of the minimal horizontal stress $\sigma_h$. This stress measurement can be derived from the leak-off pressure (LOP) or the instantaneous shut-in pressure (ISIP). In typical oil-field practice, leak-off tests are performed until the LOP, rather than a performing a complete test (Zoback, 2010, p. 212). While this test provides an accurate measurement, it is expensive to perform.

- Well deformation gives also information on the stress state. Well ovalization and well breakouts are known to be a stress-related effects due to tectonic factor. Indeed, the horizontal stress anisotropy creates an elasto-plastic anisotropic strain which follows the direction the horizontal minimal stress.
- Vertical stress is the most well-known stress. For a horizontal layered model, it can be estimated by integrated the density along the depth. The vertical stress $\sigma_V$ at a depth $z_0$ is the sum of the weight of the overlying rocks and water such as

$$\sigma_V(z_0) = \int_0^{z_0} \rho_b g dz \quad , \tag{3.1}$$

  with $\rho_b$ the density and $g$ the standard acceleration of gravity.

Acquiring directly mechanical data (in situ stress field measurements e.g. leak-off tests) is very expensive and consequently the data available to constrain the model are sparse, relatively uncertain and limited to well localization (Zoback et al., 2003).

To alleviate this difficulty, we propose to introduce new constraints to the inverse problem to limit the model space dimension.

### 3.2.2 Stress decomposition

A first estimate of the stress field can be obtained by considering only the gravitational part of the stress. In the water, the stress is isotropic (hydrostatic stress) and it can be written from the pressure $p$ as

$$\boldsymbol{\sigma} = p\mathbf{1} \quad , \tag{3.2}$$

and the pressure is weight of the water column

$$p = \rho_w g z \quad . \tag{3.3}$$

We consider that the model is homogeneous laterally and undergoes plane strain. Then the displacement field takes the form

$$\boldsymbol{u} = (0, 0, u_z(z)) = u_z(z)\boldsymbol{e_z} \quad . \tag{3.4}$$

The non-vanishing strain is $\varepsilon_{zz} = \frac{du_z}{dz}$. From Hooke's law, we obtain the non-null stresses

$$\sigma_{xx} = \sigma_{yy} = \lambda\varepsilon_{zz} \quad \text{and} \quad \sigma_{zz} = (\lambda + 2\mu)\varepsilon_{zz} \quad . \tag{3.5}$$

The Cauchy's equilibrium equation is

$$\frac{\partial \sigma_{zz}}{\partial z} = \rho g \quad . \tag{3.6}$$

Using the boundary condition $\sigma_{zz}(z_0) = \rho_w g z_0$, we integrate the equilibrium equation to

$$\sigma_{zz}(z) = \rho_w g z_0 + \rho g (z - z_0) \quad . \tag{3.7}$$

The lateral stress can be written as

$$\sigma_{xx} = \frac{\lambda}{\lambda + 2\mu}\sigma_{zz} \quad . \tag{3.8}$$

The quantity $\frac{\lambda}{\lambda+2\mu}$ depends only of the Poisson's ratio and corresponds to the lateral earth pressure at rest $K_0 = \frac{\nu}{1-\nu}$. The lateral stress field is

$$\sigma_{xx}^{\text{grav}} = K_0 \left(\rho_w g z_0 + \rho g (z - z_0)\right) \quad . \tag{3.9}$$

In this simplified model, the stress fields do not depend on the Young modulus. This lateral stress is taken as initial condition of our optimization problem. We decompose the stress into a gravitational part and a tectonic part such as

$$\sigma_{xx} = \sigma_{xx}^{\text{grav}} + \sigma_{xx}^{\text{tec}} \quad , \tag{3.10}$$

and this stress is used as Neumann boundary condition of the right side of our model. The tectonic part is parametrized with a piecewise linear function

$$\sigma_{xx}^{\text{tec}} = \begin{cases} A_1 + B_1(z - 0.5(z_0 + z_1)) & \text{si } z_0 \leq z < z_1 \\ A_2 + B_2(z - 0.5(z_1 + z_2)) & \text{si } z_1 \leq z < z_2 \\ \vdots & \\ A_N + B_N(z - 0.5(z_{N-1} + z_N)) & \text{si } z_{N-1} \leq z < z_N \end{cases} . \tag{3.11}$$

The $A_i$, respectively $B_i$, corresponds to the mean, respectively the gradient, of the lateral tectonic stress of the layer $i$. These parameters are the degrees of freedom of the optimization problem.

### 3.2.3 Stress inversion

Various methodologies have been proposed to obtain the stress field from punctual measurements through an inverse approach by several authors.

Maerten et al. (2016) propose to invert the "geomechanical paleo-stress" using fracture data. There method is based on the principle that secondary features developed around major faults provide information on the far field stress. They use a linear elastic behavior law to be able to use the boundary element method. They associate a cost function related to three kinds of fracture (open, close and shear) and they use a Monte Carlo method to find the parameters which minimize the cost function. They also suggest that additional information can be used to constrain the inversion such as in-situ stress (breakout, leak off tests, induced fractures, well bore ovalization), fault throw, slickenline, GPS, InSAR, tiltmeter, focal mechanism, micro-seismicity, and deformed horizons.

Mazuyer et al. (2018) propose to invert the in-situ stress from punctual stress measurements in a geomechanical model. They also use a linear elastic behavior but solve with the finite element method, to handle geologically complex models. Their objective is not to retrieve the "true" stress regime which would imply to have information on the tectonic state during the geological time and large deformation algorithm, rather they look for an "equivalent stress state which matches the true stress state at data points. They decompose the in-situ stress into two components: a gravitational one which correspond the lithostatic stress and a tectonic one which allows for a deviation from the lithostatic stress. For that, they consider the Neumann boundary conditions as parameters (using a piecewise linear function) that can be changed to honor punctual

stress values measured along well. A cost function is defined as the misfit between the measured value and the value from the model and they use an ensemble method (CMA-ES) to find the boundary conditions which minimize the cost function. In addition to the sparse data measured at some well positions they propose to include the Von Mises stress in regions where information about fracture opening is known.

#### 3.2.3.1 Introducing Yield criterion as a stress state to constrain the inversion

Direct stress data are only accessible along well paths. But geologist have hints on whether a fault is active or not. A yield criterion can be used to represent this information, and then provide additional information on the stress data along fault.

A yield criterion is mathematically defined as a five-dimensional surface in the six-dimension space of stresses. This hypersurface can be expressed as a function $f$ such as $f(\boldsymbol{\sigma}) = 0$, where $f$ is a convex function and respects the material symmetries. Usually, the material is considered isotropic.

The Mohr-Coulomb criterion is a commonly used yield criteria in rock mechanics. In the Mohr representation (shear stress in function of the normal stress), this criterion is a straight line. To evaluate the possibility of activation of a given fault, we only need to study the stress projected on the fault facet $\sigma_n$. The resulting vector is then decomposed in a normal component and a tangential one (the direction is not needed). Then, the fault is considered inactive if $\tau < \sigma_n \tan\Phi + c$ and active if $\tau = \sigma_n \tan\Phi + c$, where $c$ is the cohesion and $\Phi$ the friction angle. The domain $\tau > \sigma_n \tan\Phi + c$ corresponds to an instability and it is considered as a forbidden domain.

We write the fault activity function as: $f(\boldsymbol{\sigma}) = \tau - \sigma_n \tan\Phi + c$, where $\sigma_n$ and $\tau$ are functions of the stress and the fault angle and $c$ and $\Phi$ are function of the contact nature of the fault. It is common to estimate that the stress value at the reservoir depth are much bigger than the fault cohesion, therefore we simply write the fault activity function as: $f(\boldsymbol{\sigma}) = \tau - \sigma_n \tan\Phi$.

We propose to add a yield criterion as a constraint to the inversion to make it compatible with fault activity information. To do so, we add to the classic least squares cost function proposed by Mazuyer et al. (2018) a term associated with the fault activity. This is performed using activation functions (Figure 3.1). Two cases are considered here:

- The fault is inactive. The fault activity function must be negative i.e. $f(\sigma) < 0$. The activation function used is

$$g(f(\boldsymbol{\sigma})) = \begin{cases} \tanh f(\boldsymbol{\sigma}) & \text{if } f(\boldsymbol{\sigma}) \geq \epsilon \\ 0 & \text{else} \end{cases}, \tag{3.12}$$

  where $\epsilon$ is a parameter which allows to add a tolerance on the yield criteria. This parameter must be small.

- The fault is active. The fault activity function must be zero i.e. $f(\boldsymbol{\sigma}) = 0$. The

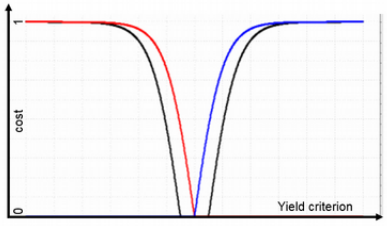


Figure 3.1: Activation functions

activation function used is

$$g(f(\boldsymbol{\sigma})) = \begin{cases} \tanh(f(\boldsymbol{\sigma})) & \text{if } f(\boldsymbol{\sigma}) \geq \epsilon \\ \tanh(-f(\boldsymbol{\sigma})) & \text{if } f(\boldsymbol{\sigma}) \leq -\epsilon \\ 0 & \text{else} \end{cases} . \tag{3.13}$$

#### 3.2.3.2 Method

**Forward Problem:** We consider a geological domain $\Omega$ bounded by $\Gamma_h$ and $\Gamma_v$ respectively the horizontal and vertical boundaries. The computation of the stress state in each point of $\Omega$ is performed using a Finite Element Model $\boldsymbol{\sigma} = F(\boldsymbol{C}, \boldsymbol{g}, \boldsymbol{h})$, where $\boldsymbol{C}$ is the elasticity tensor containing the elastic coefficients, $\boldsymbol{g}$ corresponds to the Dirichlet conditions applied on the horizontal boundaries and $\boldsymbol{h}$ corresponds to the Neumann boundary conditions applied on vertical boundaries. Since $\boldsymbol{C}$ and $\boldsymbol{g}$ are kept constant, the forward problem can be re-written $\boldsymbol{\sigma} = \bar{F}(\boldsymbol{h})$.

**Cost Function:** The initial cost function as posed by Mazuyer et al. (2017) can be written as:

$$J(\boldsymbol{h}) = \sum_{\Omega_D} (F_d(\boldsymbol{h}) - D_d)^2 \tag{3.14}$$

i.e. the sum over the data points $\Omega_D$, of the squared difference of the modeled data $D_d$ and the measured data $D_d$. The data points can refer to any type of data that can be extracted from a mechanical simulation. It usually resumes to $\sigma_h$ estimated using leak-off test when assuming an Andersonian stress state (Zoback et al., 2003).

Mazuyer et al. (2018) search the Neumann conditions $h$ in term of piecewise linear functions that minimize $J(h)$.

Our approach consists in adding to the previous cost function J(h) new constraints associated to yield criteria. We try to minimize the cost function in equation 3.14 while imposing that the stress state is at the yield criterion over a part of model $\Omega_=$, has passed the yield on the domain $\Omega_+$ part of the model and is below the yield criterion on the domain $\Omega_-$ part of the model.

Only one or two of the constraints can be included in the cost function and the sub-domains $\Omega$ can represent a small part of the model (like a fault) or the whole model.

**Optimization:** To solve the equation 3.14, we use the Covariance Matrix Adaptative Evolution Strategy (CMA-ES—Auger and Hansen, 2011). This algorithm is a derivative-free global optimizer which belongs to the family of ensemble methods (Thore and Hubans, 2012). To solve the constrained optimization problem, we cannot use the

classic approach of Lagrange multipliers since this would require calculation of derivatives which is not feasible for mechanical simulator in the general case. We cannot simply reject models that would not respect the constraints because constraints are specified in the data space. The simple strategy of rejection would also induce a high computation time. Our approach consists in transforming hard constraints in soft constraints using step functions (Figure 3.1).

We re-write the cost function 3.14 in the following manner:

$$J(\boldsymbol{h}) = w_D \sum_{\Omega_D} (F_d(\boldsymbol{h}) - D_d)^2 + w_= \delta_{\Omega_=}(Y(\boldsymbol{h})) + w_+ H^+_{\Omega_+}(Y(\boldsymbol{h})) + w_- H^-_{\Omega_-}(Y(\boldsymbol{h})) \quad (3.15)$$

i.e. we add to Equation 3.14 a cost relative to the yield constraints with a Dirac-like function for equality constraint and Heaviside-like functions for inequality constraints. The difficulty lies in the weighting of the different parts of the cost function since the ensemble of data $\Omega_*$ on which they apply can be quite different in size. For the cost function to mimic a constrained problem we need to have the weighting of the constraints to be large compared to the weighting of the data such that the cost function is dominated by the constraint part while the constraints are not verified (i.e. when $\delta$ and $H$ are equal or close to 1) and driven by the data when the constraints are verified (i.e. $\delta$ and $H$ are equal to 0).

**Parameters to use:** The degrees of freedom of this geomechanical inversion are the right border boundary condition (it is what we call the tectonic forces). Because the relationship between the Neumann boundary condition are the stress measured at any point of the model is linear (because we use a linear elastic behavior law), we can use the superposition principle. $\sigma^{\text{tec}}_{xx}$ is decomposed into a $2N$ functions basis such as

$$f_i = \begin{cases} 1 & \text{if } z_i \leq z < z_{i+1} \\ 0 & \text{else} \end{cases} \quad (3.16)$$

and

$$g_i = \begin{cases} z - \frac{z+z_{i+1}}{2} & \text{if } z_{i-1} \leq z < z_i \\ 0 & \text{else} \end{cases} \quad (3.17)$$

such as

$$\sigma^{\text{tec}}_{xx} = \sum_{i=0}^{N-1} A_i f_i + B_i g_i \quad (3.18)$$

Then the stress calculated in the well $\sigma^{\text{tec}}$ is

$$\sigma^{\text{well}}(\sigma^{\text{tec}}_{xx}) = \sum_{i=0}^{N-1} A_i \sigma^{\text{well}} f_i + B_i \sigma^{\text{well}} g_i \quad (3.19)$$

Using the superposition principle, $2N$ well-chosen geomechanical models are enough to explore all the possible solutions.

### 3.2.4 Test data

The method is tested on a model inspired by geometry of a real field of West Africa. It consists of a 2D model 18 km long and 3.5 km deep under around 1.5 km of water. It

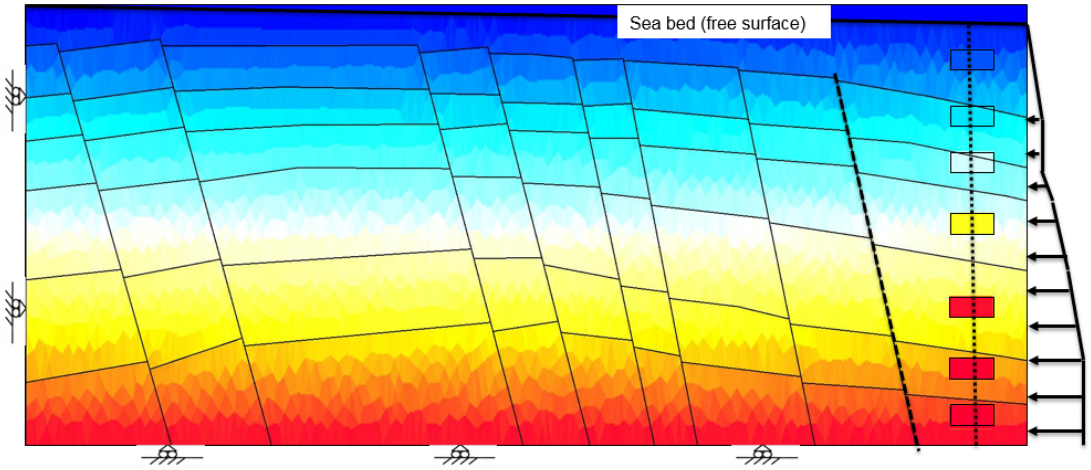


Figure 3.2: Initial stresses of the case study. The dashed line is the studied fault. On the right of the model, we consider a vertical well (marked as a dotted vertical line) with 7 known values of the horizontal stress.

corresponds to a deep water environment in an extension context, with 8 major normal faults not reaching the surface. The model is considered homogeneous and isotropic with a Young modulus of 700 MPa and a Poisson's ratio of 0.25. The density of the rock is 2.06 kg/m$^3$, and the density of the water is 1 kg/m$^3$. The fact that we have used a homogeneous model is not a limit for our method. This choice has simply been made because our goal was to show how Coulomb stress can be introduced in the inversion rather than performing the inversion on real model, which has already achieved by Mazuyer et al. (2018).

We initialize the piecewise Neumann boundary conditions with horizontal forces equal to half of the vertical stress given by the earth weight (Figure 3.2). We then perform an initial mechanical simulation and extracted a value of $\sigma_{xx}$ along a well situated on the right end side of the model close to the side where the Neumann boundary conditions are applied. These values are perturbed in a coherent manner and later used as data points. The Coulomb criteria was measured along the fault situated on the right side of the model (again near the side where Neumann boundary conditions are applied). It appears that with these initial conditions the fault was not reactivated.

We perform two inversion runs. The first one without introducing the Coulomb criterion as constraint and the second which constraints the solution to have the fault active. Cost functions are represented on the Figure 3.4. On the first run of (Figure 3.4A) the cost function diminishes a lot but never succeed to find Neumann boundary conditions that perfectly match the data points: the final cost is of the order of 1 in the normalized space (deviation to data points normalized by data uncertainty). For the second run (Figure 3.4B), which includes the constraint that the fault is active, the constraint is perfectly respected but the final solution is farther from data (a cost of the order of 2.5) that in the first run: the original data show a non-active fault. It is interesting to note (this is not shown on the figures) that the final solution of the second run gives a solution that seem to be more physical in terms of stress field as if the constraint had regularized the solution. Another noticeable point is that mechanical simulations face the Saint-Venant's principle (i.e. the stress state at position far enough

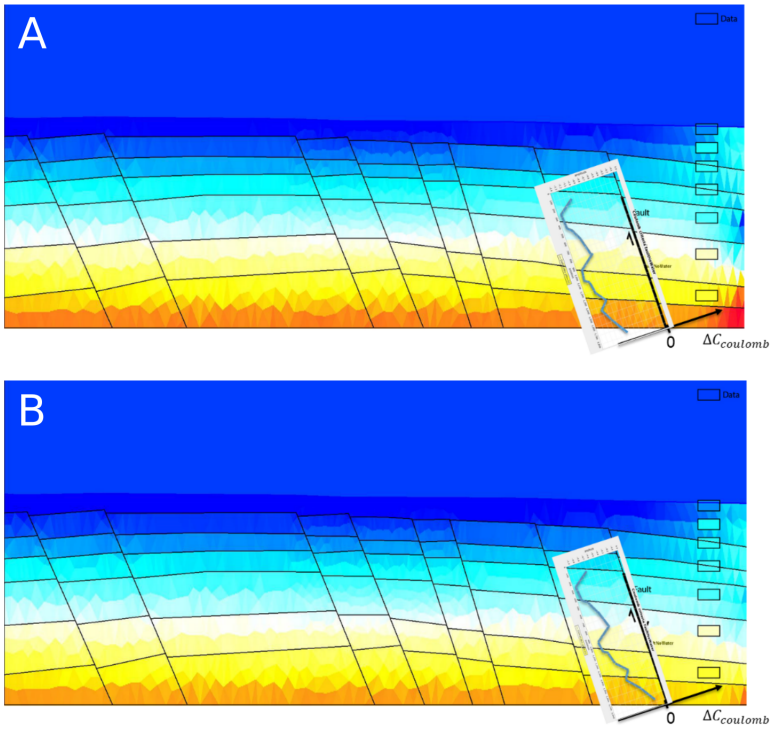


Figure 3.3: Stress results. (A) Case where the fault is considered inactive. (B) Case where the fault is considered active.

from the source is independent of the way the sources have been applied) which explains why even in the case without constraint the data cannot be matched perfectly.

## 3.3 Conclusion

A new type of data to constraint mechanical models have been introduced: the yield criterion. This type of information can be obtained or assess independently of classical mechanical information used to constrain mechanical model. Compared to other source of mechanical data this type of information is solid and drastically reduces the domain of possible solutions of the inverse problem. The parameters that are required in addition to the black or white active/non active state for the fault are the friction angle and the cohesion along the fault. These parameters are usually grossly known. We have presented a way of incorporating this information in an inverse process to determine equivalent boundary conditions. Our next step is to introduce poroelasticity (aquifer and depletion information) to better assess well stability and geohazard.

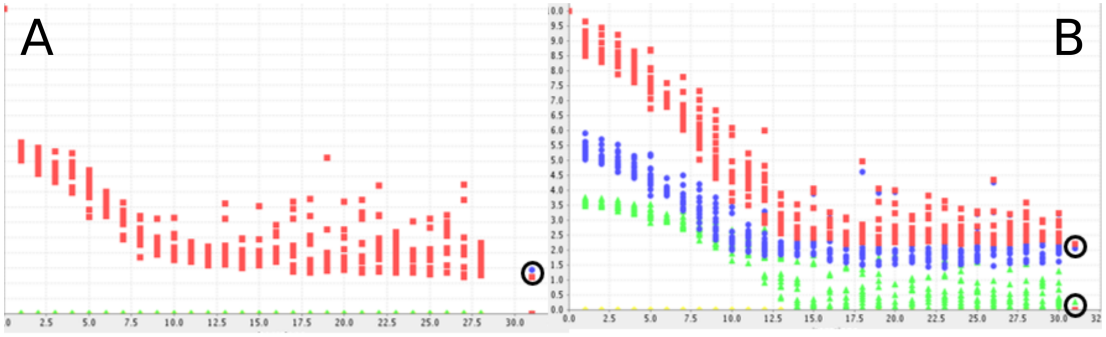


Figure 3.4: Evolution of the cost during the CMA-ES iterations. The red points corresponds to the global cost. The green points corresponds to the cost induced by the stress misfit along the well. The blue points corresponds to the cost due to the fault activation criterion. The circled points correspond to the best candidate found at the end of the algorithm. (A) Case where the fault is considered inactive. (B) Case where the fault is considered active. In that case, the final cost is mainly due to the fault activation criterion.

# Chapter 4

# Determination of a stress-dependent rock-physics model using anisotropic time-lapse tomographic inversion

**Contents**

**Abstract** In the petroleum industry, time-lapse (4D) studies are commonly used for reservoir monitoring, but are also useful to perform risk assessment for potential overburden deformations (e.g., well shearing, cap rock integrity). Although complex anisotropic velocity changes are predicted in the overburden by geomechanical studies, conventional time-lapse inversion workflows only deal with vertical velocity changes. To retrieve the geomechanically induced anisotropy, we propose to use a reflection traveltime tomography method coupled with a time-shift estimation algorithm of prestack data of the baseline and monitor simultaneously. For the 2D approach, we parameterize the anisotropy using five coefficients, enough to cover any type of anisotropy. Before applying the workflow to a real dataset, we first study a synthetic dataset based on the real dataset and include velocity variations between baseline and monitor found in the literature (vertical P-wave velocity decrease in the cap rock and isotropic P-wave velocity change in the reservoir). On the synthetics we measure the angular ray coverage necessary to retrieve the target anisotropy and observe that the retrieved anisotropies depend on the offset range. Based on a synthetic experiment, we believe that the acquisition of the real case study is suitable for performing tomographic inversion. The anisotropic velocity changes obtained on three inlines separated by 375 m are consistent and show a strong positive anomaly in the cap rock along the 45° direction ($\delta$ parameter in Thomsen notation) while the vertical velocity change is surprisingly almost negligible. We propose a rock-physics explanation compatible with these observations and geological considerations: a reactivation of water-filled subvertical cracks.

This chapter was published in the journal *Geophysics*.

N. Mastio, P. Thore, M. Conin, and G. Caumon. Determination of a stress-dependent rock-physics model using anisotropic time-lapse tomographic inversion. *Geophysics* 85: C141–C152. doi: 10.1190/geo2019-0526.1

## Résumé du Chapitre 4

Dans l'industrie pétrolière, des études 4D sont couramment utilisées pour surveiller le réservoir, mais elles sont aussi utilisées pour prédire les risques dans les roches susjacentes au réservoir. Bien qu'une anisotropie complexe des changements de vitesse des ondes soit prédite par les modèles de roches, l'inversion sismique 4D l'ignore et ne considère que les changements de vitesse verticale. Pour retrouver cette anisotropie induite par la géomécanique, nous proposons d'estimer le changement de la vitesse des ondes à partir du changement en temps de trajet des rayons réfléchis par tomographie. Ce dernier est estimé en réalignant la réflexion observée sur la trace du moniteur avec celle de la base. Dans une approche 2D, nous paramétrons l'anisotropie à travers 5 coefficients. Nous étudions d'abord un cas synthétique où nous avons introduit une anomalie de vitesse elliptique dans la roche couverture et une augmentation de vitesse dans le réservoir dans toutes les directions. Ce cas synthétique nous a permis de déterminer la couverture angulaire nécessaire à la mesure de l'anisotropie du changement de la vitesse des ondes. Ensuite, nous appliquons cette méthode à des données sismique 4D d'un champ gazier. La paramétrisation est ici simplifiée à 3 paramètres afin de mesurer la variation de la vitesse des ondes verticalement, horizontalement, et à 45°. L'application sur ce cas réel, le long de trois lignes d'acquisition, a montré que les roches couvertures sont soumises à des changements de vitesse anisotropes dans une direction de 45°, ce qui correspond à une diminution du paramètre delta selon la notation de Thomsen. De plus, l'anomalie de vitesse verticale est faible. Ces résultats suggèrent que, dans la couverture réservoir, une augmentation de la pression du fluide contenu dans un réseau de fractures verticales apparaît durant la production du champ.

## 4.1 Introduction

The repetition of seismic surveys during hydrocarbon reservoir production is a widely used monitoring method. However, the interpretation of the shifts between vintages of time-lapse seismic data in terms of fluid, mechanical and geometrical changes is challenging especially with respect of the time-lapse effect in the overburden (Røste et al., 2006). Indeed, overburden time shifts have been observed in a wide range of time-lapse studies: chalk fields, e.g. Valhall (Barkved and Kristiansen, 2005; Hatchell et al., 2005); high-pressure high-temperature fields, e.g. Elgin, Franklin and Kristin (De Gennaro et al., 2008; Dybvik et al., 2009); sandstone reservoir at normal pressure and temperature, e.g. Snorre field (Røste et al., 2015); turbidite sands fields, e.g. Genesis and Dalia fields (Rickett et al., 2007; Rodriguez-Herrera et al., 2015). Except in rare cases where subsidence is significant (e.g. Ekofisk field—Guilbot and Smith, 2002), shifts in the time-lapse vintages are preponderantly due to the accumulation of small velocity changes.

These velocity changes are the signature of the geomechanical response to the reservoir compaction. Because linear elasticity is incompatible with velocity change, nonlinearity has to be considered. For instance, Prioul et al. (2004) propose to use 'third-order' elasticity coefficients theorized by Hearmon (1953) to express the stress dependence of elastic properties. Laboratory experiments on different shales have been performed to calibrate these coefficients. Based on geomechanical models and published 'third-order' elasticity coefficients, Fuck et al. (2009) and Herwanger and Horne (2009) show that the reservoir production creates anisotropic velocity changes in the reservoir and the surrounding rocks.

Despite numerous theoretical evidences of anisotropy, the overburden time-lapse velocity change is usually considered vertical for operational purposes. One-dimensional time-lapse inversion is common in practice (Williamson et al., 2007). Furthermore, the rock physics which can relate the velocity change to the stress change is not known. This missing rock-physics model is substituted by the empirical model of Hatchell and Bourne (2005) and Røste et al. (2006), which assumes a linear relationship between the velocity change and the relative thickness variations of the overburden layers.

To overcome the limitations of a trace-by-trace inversion, Edgar and Mastio (2017) propose a prestack tomographic inversion method which considers an isotropic time-lapse velocity change. The authors build a ray-based inversion, which accounts for velocity changes along different rays. It consists in coupling a trace alignment procedure with the linearized reflection traveltime tomography to construct a nonlinear scheme, which looks for a smooth time-lapse velocity change that aligns the vintages of time-lapse prestack seismic data. This method avoids the one-dimensional approximation and retrieves velocity changes globally while respecting the ray theory.

In the present contribution, the tomographic inversion method is adapted to tackle an anisotropic perturbation in an initial model assumed isotropic (Červený, 2001). Finding a proper parametrization with respect to the data and the aperture width is essential when an anisotropic model is used to fit seismic data (Alkhalifah and Plessix, 2014; Oh

and Alkhalifah, 2016). The problem is very ill-posed. Prieux et al. (2011) applied full waveform inversion of the Valhall case study, and showed that a nearly equivalent match of the data can be obtained with an isotropic or an anisotropic velocity model. The parametrization must be chosen carefully to obtain a meaningful result.

In the literature, the velocity change in the overburden is assumed to be mainly vertical. In a synthetic case, we introduce a vertical velocity decrease in the overburden and an isotropic velocity increase in the reservoir. We show that our method can retrieve the anisotropic perturbation induced in the velocity model when the acquisition range is large enough. An application to time-lapse vintage of a gas field where the anisotropy of the perturbation is not known is proposed. Our method shows a surprising 45° and horizontal velocity decrease in the cap rock. A plausible rock-physics model based on the homogenization of cracks compatible with the anisotropy of the velocity change and the stress change is derived.

## 4.2 Methods

### 4.2.1 Time shifts induced by an anisotropic velocity change

The velocity change between the base and the monitor has the effect of shifting the reflectors location. Measuring these time-lapse shifts allows us to do a tomographic reconstruction of the velocity change. However, in the case of an anisotropic velocity change, all the elastic parameters cannot be retrieved because only the longitudinal waves are considered.

#### 4.2.1.1 Traveltime perturbation

The traveltime perturbation expression has been established in numerous ways. For an isotropic smooth medium, based on the Fermat's principle in isotropic media (Nolet, 1987; Aki and Richards, 2002), the traveltime perturbation $\Delta t$ along a ray $\Omega_0$ is linearized as

$$\Delta t = -\int_{\Omega_0} \frac{\Delta v}{v_0} dt \quad , \tag{4.1}$$

where $\frac{\Delta v}{v_0}$ is the relative velocity change between the referenced and the perturbed model and $dt$ is the time increment of the ray. For a smooth anisotropic medium, based on the Lagrangian approach (Nowack and Pšenčík, 1991) and the Hamiltonian approach (Červený, 2001), the traveltime perturbation becomes (using Einstein summation rules)

$$\Delta t = -\frac{1}{2}\int_{\Omega_0} \Delta a_{ijkl} p_i p_j g_k g_l dt \quad , \tag{4.2}$$

where $\boldsymbol{p}$ is the slowness vector, $\boldsymbol{g}$ is the polarization vector and $a_{ijkl}$ is the density normalized elastic tensor $a_{ijkl} = \frac{c_{ijkl}}{\rho}$ ($c_{ijkl}$ is the fourth-order elastic tensor and $\rho$ is the rock density) which has the same dimension as a squared velocity. At a first-order approximation, the traveltime perturbation is suitable to solve the tomographic inverse problem (Chapman and Pratt, 1992; Le Bégat and Farra, 1997).

For simplicity of presentation, we consider longitudinal elastic waves only propagating in an initially isotropic heterogeneous medium at velocity $v_0$. In this case, the

slowness vector $\boldsymbol{p}$ and polarization vector $\boldsymbol{g}$ have the same direction as the propagation direction $\boldsymbol{n}$. This can be written as

$$\boldsymbol{p} = \frac{1}{v_0}\boldsymbol{n} \quad \text{and} \quad \boldsymbol{g} = \boldsymbol{n} \quad , \tag{4.3}$$

and the infinitesimal anisotropic velocity change as

$$\frac{\Delta v}{v_0} = \frac{\Delta a_{ijkl}}{2v_0^2} n_i n_j n_k n_l \quad . \tag{4.4}$$

In the context of time-lapse seismics, we consider a reference medium, which corresponds to a field state before production i.e. to the base seismic image, and a second medium corresponding to a snapshot of the same field after a production period corresponding to the monitor seismic image. We expect the velocity field of the second medium is slightly different from that of the reference medium due to the change in the effective stress field in the cap rock and in the reservoir induced by the production of fluids initially present within the reservoir.

#### 4.2.1.2 Parametrizations of the longitudinal wave anisotropy

In the case of anisotropy, inverse problems applied to seismic data suffer from ill-conditioning and non-uniqueness because of the large number of parameters needed to describe the material behavior in the general case, and the limited offset acquisition (Alkhalifah, 1997; MacBeth, 2002; Oh and Alkhalifah, 2016; Kazei and Alkhalifah, 2018; Podgornova et al., 2018).

In the case of general anisotropy, the traveltime perturbation depends on the 21 independent elastic parameters change $\Delta a_{ijkl}$. Perturbations of all elastic parameters cannot be retrieved for two main reasons. The first one is that the reference interval velocity model influences the angle coverage for a given acquisition length, limiting the range of illumination angles available to characterize the elastic coefficients. The second one is that the longitudinal traveltime perturbation is influenced by 15 parameters only, where the 6 constants or combinations: $c_{11}$, $c_{22}$, $c_{33}$, $c_{12}+2c_{66}$, $c_{23}+2c_{44}$, and $c_{13}+2c_{55}$ are the most sensitive parameters and the remaining ones: $c_{16}$, $c_{15}$, $c_{26}$, $c_{24}$, $c_{35}$, $c_{34}$, $c_{14}+2c_{56}$, $c_{25}+2c_{46}$, and $c_{36}+2c_{45}$ have a much smaller influence (Backus, 1970; Every and Sachse, 1992; Kazei and Alkhalifah, 2018). These 15 parameters correspond to the totally symmetric part of the elastic tensor $s_{ijkl} = \frac{1}{3}(c_{ijkl} + c_{iklj} + c_{iljk})$ which can be expressed with the Voigt notation (Love, 1944) as

$$s_{ijkl} = \begin{pmatrix} \boxed{\boldsymbol{s_{11}}} & \boxed{\boldsymbol{s_{12}}} & \boxed{\boldsymbol{s_{13}}} & \boldsymbol{s_{14}} & \boldsymbol{s_{15}} & \boldsymbol{s_{16}} \\ * & \boxed{\boldsymbol{s_{22}}} & \boxed{\boldsymbol{s_{23}}} & \boldsymbol{s_{24}} & \boldsymbol{s_{25}} & \boldsymbol{s_{26}} \\ * & * & \boxed{\boldsymbol{s_{33}}} & \boldsymbol{s_{34}} & \boldsymbol{s_{35}} & \boldsymbol{s_{36}} \\ * & * & * & s_{44} & s_{45} & s_{46} \\ * & * & * & * & s_{55} & s_{56} \\ * & * & * & * & * & s_{66} \end{pmatrix}, \tag{4.5}$$

where the 15 independent parameters (in bold) are $s_{11} = c_{11}$, $s_{22} = c_{22}$, $s_{33} = c_{33}$, $s_{15} = c_{15}$, , $s_{16} = c_{16}$, , $s_{26} = c_{26}$, $s_{24} = c_{24}$, $s_{34} = c_{34}$, $s_{35} = c_{35}$, $s_{12} = \frac{1}{3}(c_{12} + 2c_{66})$, $s_{13} = \frac{1}{3}(c_{13} + 2c_{55})$, $s_{14} = \frac{1}{3}(c_{14} + 2c_{56})$, $s_{23} = \frac{1}{3}(c_{23} + 2c_{44})$, $s_{25} = \frac{1}{3}(c_{25} + 2c_{46})$, and

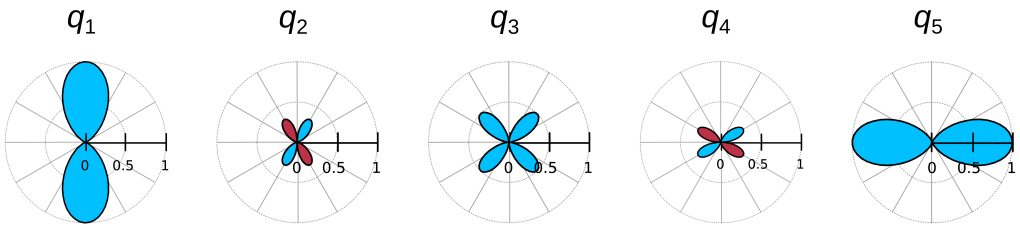


Figure 4.1: Geometrical representation of basis used in polar plots. The five functions define general anisotropy in 2D. Each quarter is subdivided into three parts such as each one represents 30°. We can see graphically that $q_1$ and $q_2$ are sensitive to polar angles between 0° to 30°, $q_3$ is sensitive to angles between 30° to 60° and $q_4$ and $q_5$ are sensitive to polar angles between 60° to 90°. Blue indicates positive values, red negative values.

$s_{36} = \frac{1}{3}(c_{36} + 2c_{45})$. The boxed parameters represent the most sensitive ones.

As the following tomography is performed along inlines, the 2D approach is developed. The anisotropic tomography parameterization problem has already been successfully tackled by Chapman and Pratt (1992) for the case of crosswell tomography and we decide to use their parametrization with slight modifications. We recall the construction of this parametrization in the following. Considering a basis $Ox_1x_2x_3$ oriented such as $x_1$ is the horizontal axis, $x_2$ is the out of plane axis and $x_3$ is the vertical axis, the polarization vector takes the form $n = (\sin\theta, 0, \cos\theta)$, where $\theta$ is the angle between the ray and the vertical axis. In polar coordinates, the anisotropic velocity change in equation 4.4 can be written as

$$\frac{\Delta v}{v_0}(\theta) = q_1 \cos^4\theta + q_2 \cos^3\theta \sin\theta + q_3 \cos^2\theta \sin^2\theta + q_4 \cos\theta \sin^3\theta + q_5 \sin^4\theta \quad , \quad (4.6)$$

where the $q_i$ are functions of the normalized elastic tensor perturbation:

$$q_1 = \frac{\Delta a_{33}}{2v_0^2} \, , \; q_2 = \frac{\Delta a_{35}}{2v_0^2} \, , \; q_3 = \frac{\Delta a_{13} + 2\Delta a_{55}}{2v_0^2} \, , \; q_4 = \frac{\Delta a_{15}}{2v_0^2} \, , \text{ and } \; q_5 = \frac{\Delta a_{11}}{2v_0^2} \, . \quad (4.7)$$

The basis functions used in equation 4.6 are depicted in Figure 1.

This parametrization is general in the sense that it does not assume any material symmetry. The coefficient $q_3$ in equation 4.7 is slightly different from the one described in Chapman and Pratt (1992). Using the proposed coefficients, the three parameters $q_1$, $q_3$ and $q_5$ have the same amplitude for an isotropic velocity change enabling the use of the same regularization weights for these parameters in the inverse problem.

In any case, the most sensitive parameters are $q_1$, $q_3$ and $q_5$ (Every and Sachse, 1992). Moreover, $q_2$ and $q_4$ are equal to zero if the elastic perturbation has a vertical symmetry direction. In this case, $q_1$ represents the vertical to subvertical velocity change. It corresponds to the type of parameters that a classical seismogram trace alignment algorithm attempts to retrieve. $q_3$ is the velocity change measured at $\tilde{4}5°$ and $q_5$ is the horizontal to subhorizontal velocity change. If the vertical symmetry assumption is not respected, $q_2$ or $q_4$ are not equal to zero. In the special case of a

weak vertical transverse isotropy elastic perturbation, the velocity change can be written as $\frac{\Delta v}{v} = \frac{\Delta v}{v}(0°) + \delta \cos^2\theta \sin^2\theta + \varepsilon \sin^4\theta$ (Thomsen, 1986), which is translated to $q_1 = \frac{\Delta v}{v}(0°)$, $q_3 = \frac{\Delta v}{v}(0) + \frac{\delta}{2}$, and $q_5 = \frac{\Delta v}{v}(0°) + \varepsilon$. In this case, vertical velocity change $q_1$ corresponds to the isotropic velocity change, and the differences $2(q_3 - q_1)$ and $q_5 - q_1$ measure the anisotropy. For a tilted transversely isotropic material, the three Thomsen parameters, the azimuth and the dip can be estimated with the five components of $\boldsymbol{q}$. The transformation is exposed in detail in (Chapman and Pratt, 1992, p. 17–19).

### 4.2.2 Tomographic inversion

In classical time-lapse inversion, the measured time shifts are exclusively related to a vertical velocity change. However, with vertical information only, velocity anisotropy cannot be retrieved. The time-lapse velocity change tomography method does not require the vertical assumption. Instead, it models the time shifts applied to each offset as a result of a small velocity perturbation. In our approach, the time shift estimation is embedded inside the tomographic algorithm.

#### 4.2.2.1 Time shifts estimation using arrival time warping methods

Dynamic time warping (Hale, 2013) and nonlinear least-squares regression (Rickett et al., 2007; Williamson et al., 2007) are examples of alignment algorithms formulated as optimization problems. They attempt to minimize a cost function which depends on a base trace $B(t)$ and a monitor trace $M(t)$ having the same source and receiver locations, a depth of interest (in the time domain) $\tau$, and a time shifts $\Delta t$. For the sake of simplicity, we consider a general expression of the minimization problem, but the following can be adapted to any trace alignment method written as cost function.

At a given reflection, the measured time shift $\Delta t_{\text{measured}}$ is the solution of the minimization problem

$$\Delta t_{\text{measured}} = \arg\min_{\Delta t} [r_{\text{TShift}}(\Delta t))]^2 \quad , \tag{4.8}$$

with $r_{\text{TShift}}$ being the residuals between the base $B(t)$ and the warped monitor $W(M(t), \Delta t)$ within a time window $\Delta\tau$ around the considered reflection, i.e.

$$r_{\text{TShift}} = \sum_{t=\tau-\frac{\Delta\tau}{2}}^{\tau+\frac{\Delta\tau}{2}} [B(t) - W(M(t), \Delta t)] \quad . \tag{4.9}$$

The Jacobian of the trace alignment residual depends only of the monitor trace as

$$J_{\text{TShift}} = \frac{\partial r_{\text{TShift}}}{\partial \Delta t} = -\sum_{t=\tau-\frac{\Delta\tau}{2}}^{\tau+\frac{\Delta\tau}{2}} \frac{\partial W}{\partial \Delta t}(M(t), \Delta t) \quad . \tag{4.10}$$

In equations 4.9 and 4.10, the time window $\Delta\tau$ must be adapted to the considered case since the retrieved time shifts are sensitive to the chosen window length (Mikesell et al., 2015).

The choice of the relevant trace alignment algorithm depends on the time-lapse effect observed on the data set. For instance, if strong amplitude changes occur, including

the amplitude term in the trace alignment function can be considered. In the overburden, where very limited amplitude changes are observed, the presented trace alignment algorithm in equations 4.9 and 4.10 can be used.

#### 4.2.2.2 Traces realigment with a smooth anisotropic velocity change

The inverse problem can be written as a minimization problem. We look for the velocity change $q$ solution of

$$\arg\min_{\boldsymbol{q}} \left( \|r(\boldsymbol{q})\|^2 + \sum_{i=1}^{5} \|\mu_i L_i q_i\|^2 \right) \quad , \tag{4.11}$$

where $r(\boldsymbol{q})$ is the residual vector which measures the misalignment between the warped monitor trace window and the baseline and $\boldsymbol{q}$ is the column vector $(q_1 q_2 q_3 q_4 q_5)$. As with almost all subsurface inverse problems (Gubbins, 2004), a regularization is required to address the problem's ill-posedness and ensure the stability of the solution of the tomographic system. In equation 4.11, the regularization takes the form of additional costs which penalize the roughness of the $q_i$. As the model is discretized into a regular grid, for the regularization we use the Laplace filter $L$ (in a regular grid in two dimensions, the Laplacian is approximated using the five-point stencil finite-difference method). The $\mu_i$ are five parameters which control the regularization weight. Increasing $\mu_i$ increases the smoothness of $q_i$. In the applications further described in this paper, we do not assume a prior preferential direction of the anisotropy to avoid bias in the results. This leads us to consider the same value for the five regularization parameters.

#### 4.2.2.3 Construction of the tomographic system of equations

The Jacobian $J_{\text{TShift-tomography}}$ of the Time-Lapse Anisotropic Traveltime Tomography (TLATT) can be written as a function of the trace alignment such as

$$J_{\text{TShift-tomography}}(\boldsymbol{q}) = \frac{\partial r}{\partial \boldsymbol{q}}(\boldsymbol{q}) = \frac{\partial r}{\Delta t}(\boldsymbol{q}) \frac{\Delta t}{\partial \boldsymbol{q}} \quad . \tag{4.12}$$

The trace alignment part corresponds to $J_{\text{TShift}}$. It depends on the trace alignment algorithm, which in our case is given by equation 4.10. The tomographic part is the traveltime perturbation due to an anisotropic velocity change. It is computed by ray tracing in the reference interval velocity model. The linearized tomography is not a limitation and a dynamic tomography can be considered without changing the algorithm. The reason why we have decided to use the linearized approach is because (i) perturbations are small in the overburden and (ii) the dynamic approach can be unstable in certain circumstances (Jech and Pšenčík, 1989; Chapman and Pratt, 1992). The trace alignment is performed for a given window length using equations 4.8—4.10 as illustrated in Figure 4.2.

In the following, the model parameter $\boldsymbol{q}$ is discretized into a regular grid. In this representation, the traveltime perturbation due to a velocity change $\frac{\partial \Delta t}{\partial \boldsymbol{q}}$ is a matrix $A$ called the tomographic matrix. Each row of the tomographic matrix represents a ray and the columns of the matrix represent the cells of the model. As the number of model parameters is 5 times larger than in the isotropic case, the tomography matrix is the

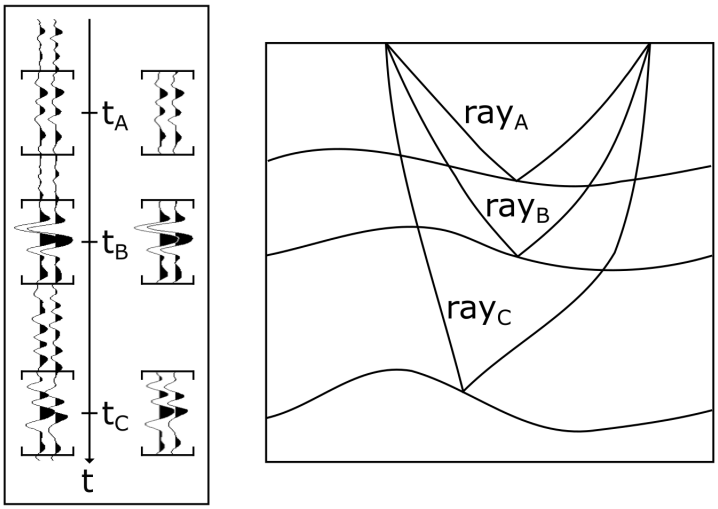


Figure 4.2: Trace alignment coupled with tomography for three reflectors sharing the same midpoint and offset at time $t_A$, $t_B$, and $t_C$. The TLATT consists of finding a velocity change $\frac{\Delta v}{v_0}$ such that the resulting time shifts $-\int_{\text{raypath}} \frac{\Delta v}{v_0} dt$ align the monitor to the baseline at the reflector time depth.

horizontal concatenation of 5 matrices labelled as $A_k$. The coefficient $a_k^{ij}$ at row $i$ and column $j$ of $A_k$ stores the travel time of the ray $i$ in the cell $j$ multiplied by the $k$-th basis function which depends on the angle of the ray $i$. Every row of the tomographic matrix is weighted by the Jacobian of the trace alignment (trace alignment part of equation 4.11). During the nonlinear iterations of the trace alignment procedure, the trace alignment residuals and its Jacobian are updated while the tomographic matrix $A$ remains constant. Indeed, the coefficients of the tomographic matrix (before weighting) depend on the reference model geometry and on the initial interval velocity model only. An example of the construction of the tomographic matrix in given in Appendix A.

#### 4.2.2.4 Resolution of the nonlinear damped least-squares problem

As the Jacobian matrix $J_{\text{TShift-tomography}}(\boldsymbol{q})$ and the residual vector $r_{\text{TShift}}(\boldsymbol{q})$ depend on the velocity change $\boldsymbol{q}$, the least squares minimization problem is solved in an iterative manner (Figure 4.3). As described by Gubbins (2004, p. 131–132), the velocity change is updated as $\boldsymbol{q}^{i+1} = \boldsymbol{q}^i + \delta\boldsymbol{q}^{i+1}$ with

$$\delta\boldsymbol{q}^{i+1} = (J^{\mathrm{T}}J + \mu^2 R^{\mathrm{T}}R)^{-1}(J^{\mathrm{T}}r - \mu^2 R^{\mathrm{T}}R\boldsymbol{q}^i) \quad , \tag{4.13}$$

where $R$ is the matricial representation of the regularization function (here five Laplacian matrices $L$ in diagonal block matrix). Equation 4.13 shows an additional term $-\mu^2 R^{\mathrm{T}}R\boldsymbol{q}^i$ as compared to the linear problem, which have the effect of damping the velocity change globally. The residuals $r = r(\Delta t^i)$ and the Jacobian matrix $J = J(\Delta t^i)$ are updated at each increment with the obtained time shift $\Delta t^i$ computed for the last velocity change estimate $\boldsymbol{q}^i$ such as $\Delta t^i = -A\boldsymbol{q}^i$ (discrete form of equation 4.2).

Equation 4.13 could be used to solve the inverse problem, but it would be very slow and difficult to compute the inverse of $J^{\mathrm{T}}J + \mu^2 R^{\mathrm{T}}R$. Instead, we use an iterative solver

$\boldsymbol{q}^0 = \mathbf{0}$

$i = 0$

Loop until convergence criteria reached

$\boldsymbol{\Delta t}^i = -\boldsymbol{A}\boldsymbol{q}^i$

$\boldsymbol{r}^i = \boldsymbol{r}_{\text{TShift}}(\boldsymbol{\Delta t}^i)$

$\boldsymbol{J}^i = \boldsymbol{J}_{\text{TShift-tomography}}(\boldsymbol{\Delta t}^i)$

$\boldsymbol{\delta q}^{i+1} = \underset{\boldsymbol{x}}{\text{argmin}} \left( \left\| \boldsymbol{J}^i \boldsymbol{x} - \boldsymbol{r}^i \right\|^2 + \mu^2 \left\| \boldsymbol{R}\boldsymbol{q}^i \right\|^2 \right)$

$\boldsymbol{q}^{i+1} = \boldsymbol{q}^i + \boldsymbol{\delta q}^{i+1}$

$i = i + 1$

End

Figure 4.3: Pseudo-code of the coupled warping tomography algorithm.

proposed by Fong and Saunders (2011), which can handle large and sparse matrices encountered in tomography as the rays cross a limited number of cells of the grid. We look for the velocity change increment $\delta \boldsymbol{q}^{i+1}$solution of the equation

$$\begin{pmatrix} J \\ \mu R \end{pmatrix} \delta \boldsymbol{q}^{i+1} = \begin{pmatrix} r \\ -\mu R \boldsymbol{q}^i \end{pmatrix} \tag{4.14}$$

in a least-squares sense. Our observations show that the number of nonlinear iterations varies from 3 to 10.

## 4.3 Results

In this section we present the results obtained on a synthetic model and on a real case study. The case study is a gas field that has been in production for over 15 years (see reservoir seal interface on Figure 4.4), with a measured depletion of 150 bars. The reservoir is a carbonate platform with a high porosity (28% average) sealed by low porosity marine shales, overlaid by prodeltaic sands and fluvio/deltaic sandstones and claystones. The reservoir lies on a volcanoclastic basement. It consists in a 10-meter-thick gas part.

Interesting reflectors are picked in the base migrated stack in the depth domain (Figure 4.5). As we are interested in the velocity change due to geomechanical effects at, and around, the reservoir, we picked reflectors in both the over- and underburden.

The selected reflectors are used as reflection points in the ray tracing to find the reflected rays with the same common depth point and the same offset as the prestack seismic traces. Unlike classical 1D time lapse inversion methods which estimate a time

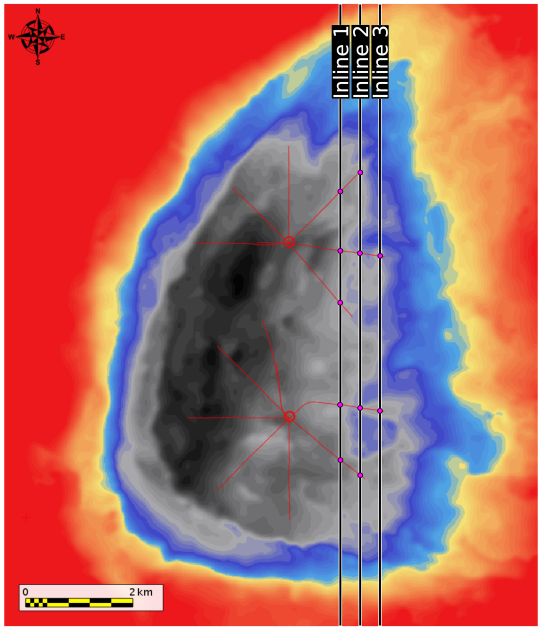


Figure 4.4: Basemap of the top of the carbonate platform. The three red lines correspond to the inline used in this article. The projected well trajectories are also presented; the wells are significantly perforated below the reservoir top.

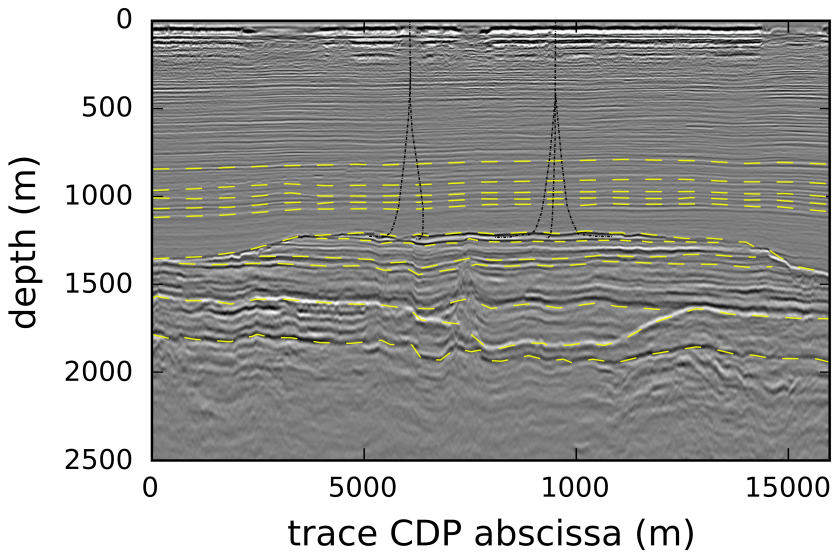


Figure 4.5: Depth migrated stacked seismic of the base for the second inline (middle one). The 12 horizons picked are drawn in dashed yellow lines.

shifts function along the trace, our method attempts to realign the monitor to the baseline for the selected reflectors. The time shifts are not actually directly estimated. Instead, a velocity perturbation which realigns the monitor to the baseline on the selected reflectors is retrieved and the time shifts are only an intermediate variable resulting from the trace alignment procedure.

### 4.3.1 Synthetic case

Before considering the real case study, we designed an analog synthetic data set to test the validity and the applicability of the tomographic inversion. The objective of this synthetic study is to assess what TLATT can retrieve in an idealized scenario corresponding to a perfectly known base model and noise free data, with similar angle coverage as in the real case. For this, we used the same geometry as the reference study. The reference velocity model used for the ray tracing is presented in Figure 4.6A. The velocity perturbations are described using Thomsen parameters (Thomsen, 1986) and correspond to an elliptic perturbation in a localized area of the overburden ($\varepsilon = \delta$). They can be written as

$$\frac{\Delta v}{v_0}(\theta) = \frac{\Delta v}{v_0}(0°) + \varepsilon \sin^2\theta \quad , \tag{4.15}$$

where $\frac{\Delta v}{v_0}(0°)$ and $\varepsilon = \frac{\Delta v}{v_0}(90°) - \frac{\Delta v}{v_0}(0°)$ represent respectively the vertical and the difference between the horizontal and the vertical time-lapse velocity change. To build the monitor model, we perturbed the base model with a 5% increase in the isotropic velocity in the reservoir and a 5% decrease in the vertical velocity in a relatively small area of the overburden. The vertical velocity change $\frac{\Delta v}{v_0}(0°)$ and the horizontal velocity change $\frac{\Delta v}{v_0}(90°)$ are presented in Figure 4.6B&C.

The time shifts between base and monitor are computed by integrating the anisotropic velocity change along rays traced on the reference velocity model, using equations 4.1 and 4.14. As the objective of the synthetic case is to assess the ray coverage associated with the acquisition geometry, we discard the uncertainty associated with time shift estimation and provide the exact time shifts to the tomography. Therefore, we only study the tomography part of equation 4.11. We performed 3 experiments for three different offset ranges: the near offsets range (325 m to 825 m), the near to mid offsets range (325 m to 1575 m) and near to far offsets range (325 m to 2375 m) (corresponding to the real data acquisition parameters). Results are shown in Figure 4.7 for the five $q_i$ parameters described in equation 4.7.

For the near offsets range (first column of Figure 4.7), only the term $q_1$ (i.e. the vertical velocity change) shows a significant amplitude at the position where the isotropic anomaly was introduced in the model. It corresponds to the isotropic velocity change both in the reservoir and the overburden. Indeed, for this acquisition, the rays are close to vertical rays and only $q_1$ is sensitive to velocity change in the vertical to subvertical direction (30° at maximum as shown in Figure 4.1). Some weak energy appears for $q_3$ but it is interpreted as a linkage between $q_1$ and $q_3$ rather than as a detection of the anisotropic anomaly. The horizontal velocity change increase is not detected in the reservoir since no horizontal rays exist.

For larger offsets range (second and third columns of Figure 4.7), the main

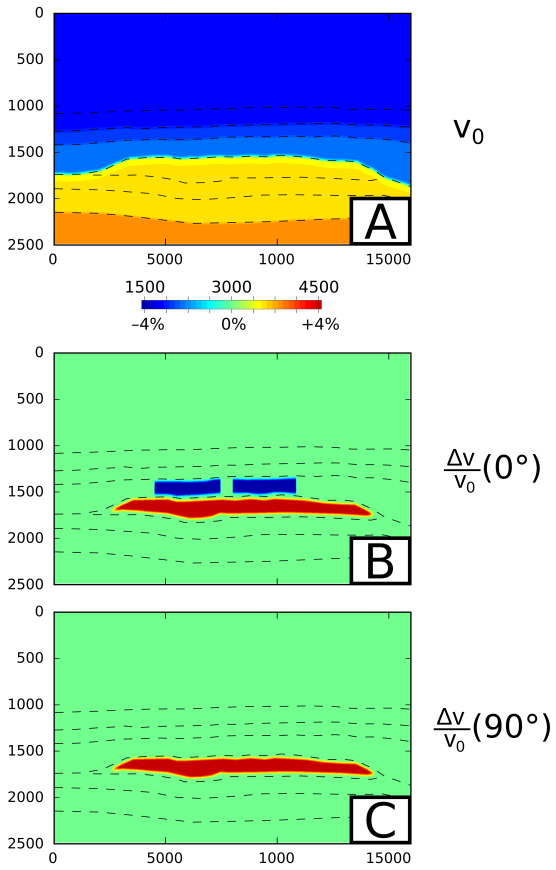


Figure 4.6: Synthetic data set. (A) The reference velocity model is heterogeneous and isotropic. The longitudinal wave velocity increases gradually in the shale (blue area) and it is chosen constant in the carbonate (orange area). The dimensions are in meters. Dashed lines correspond to reflectors. (B) Vertical velocity change. (C) Horizontal velocity change.

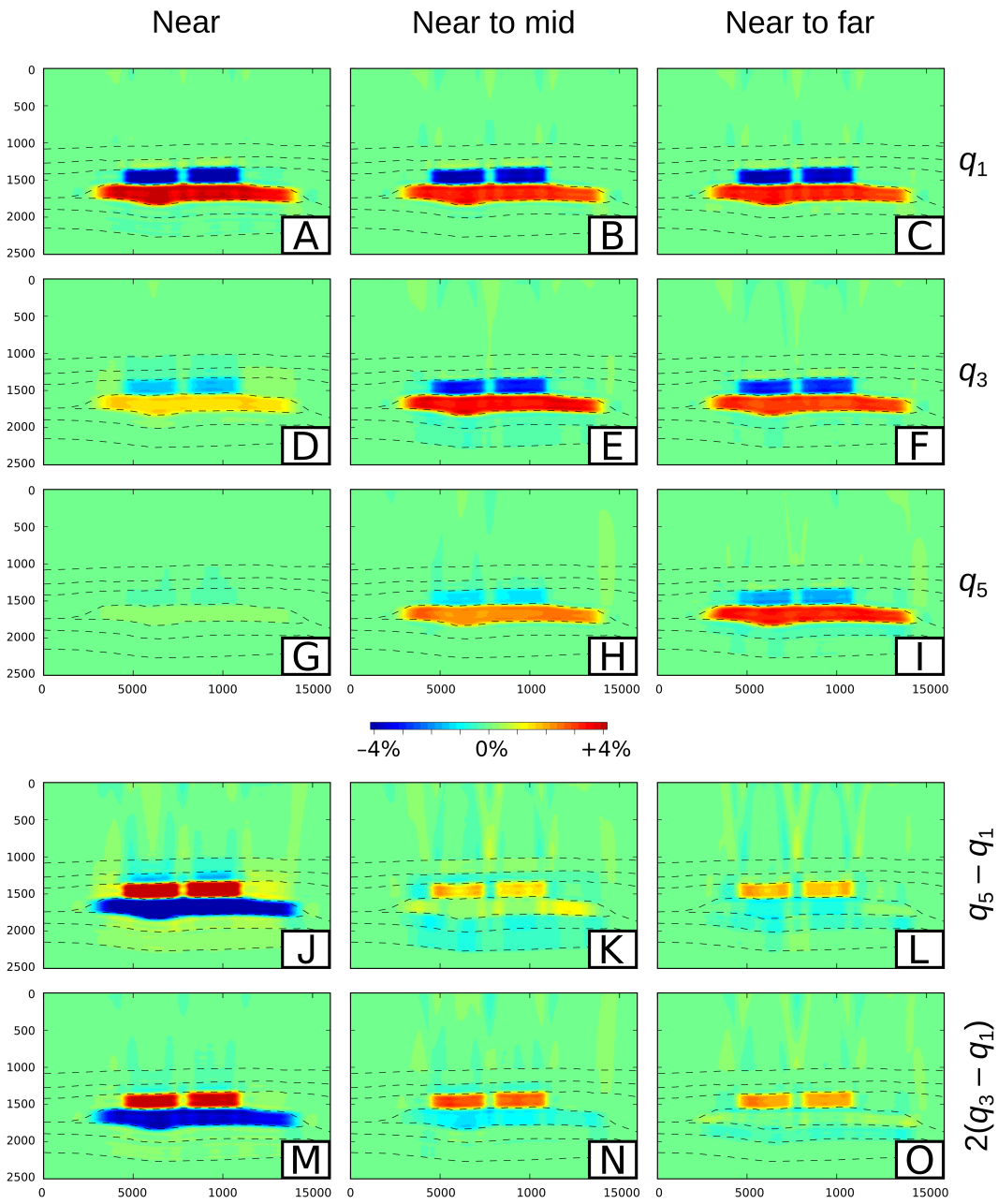


Figure 4.7: Anisotropic velocity changes retrieved by anisotropic reflection traveltime tomography. The columns represent the different offsets acquisitions. Rows represents the anisotropic velocity change parameters $q_1$, $q_3$, and $q_5$ and the algebraic formula $q_5 - q_1$ ($\varepsilon$) and $2(q_3 - q_1)$ ($\delta$) The parameters $q_2$ and $q_4$ are inverted but not presented because they are equal to zero. $q_1$ and $q_5$ must be compared with Figures 4.6B and 4.6C.

anisotropic parameters $q_1$, $q_3$, and $q_5$ show significant energy while and $q_2$ and $q_4$ are almost unchanged. Indeed, $q_2$ and $q_4$ are sensitive to tilted velocity changes which were not introduced in the perturbed model. To relate the tomographic inversion results to the true velocity anomaly, a change in the parametrization is needed. We translate the three main parameters $q_1$, $q_3$, and $q_5$ into Thomsen parameters. The results for the near to far offset cases are presented in Figure 4.7J—O. For the specific case of an elliptical velocity change, the formulas $q_5 - q_1$ and $2(q_3 - q_1)$ provide two different ways to estimate the elliptical anisotropy $\varepsilon$. The second formula works better in the case of the near to mid offsets range as the retrieved horizontal velocity change $q_5$ is not reliable. Indeed, the second formula gives a higher intensity in the caprock but a negative $\varepsilon$ in the reservoir which is not present in the synthetic velocity perturbation. For the near to far offsets range, both formulas provide similar results. The estimated parameters shape and sign are correct both for the isotropic and the anisotropic anomalies but in terms of amplitude, the inverted anomalies are weaker (by a factor of almost 2) as compared to the true values. A possible explanation for the mismatch between the recovered amplitudes and the true ones is the influence of the regularization. Another explanation is that because the sub-horizontal rays are in the minority in the caprock compared to the sub-vertical rays, the horizontal velocity change is less apparent than the vertical one.

The synthetic case, based on the geometry and velocity of the real case, shows that TLATT succeeds in recovering the shape, the position, and the sign of the anomalies. Based on this synthetic exercise, we can expect that the acquisition used in the real case study (325 m to 2375 m) is large enough to obtain a reliable anisotropic time-lapse velocity change.

### 4.3.2 Application to real data

We apply the TLATT to real data from which the synthetic example is derived. This field is chosen for its anticipated strong geomechanical effect in the cap rock and the overburden. As our method requires prestack seismic data with a large offset range, TLATT can only be performed along inlines (N/S orientation) rather than crosslines which do not contain any mid or far offsets. As the offshore platform obstructs the acquisition vessel, the inlines in the central part of the structure are missing in the monitor survey. The western part of the field is more complex because there is a shallower reservoir in this zone, so we decide to focus on the eastern part of the reservoir (Figure 4.4). We use 3 inlines separated by 375 m to check the consistency of the results. Additional information about the repeatability of the time-lapse prestack seismic data, the interval velocity model and the angular ray coverage, is given in Appendix B.

The tomography is performed first with an isotropic parameterization and second with an anisotropic parameterization using all the available offsets. In both cases, ten nonlinear iterations are needed to obtain the convergence of the system and the same regularization weights are used for each anisotropic parameter. The trace alignment is performed on a 180 ms window, which is the best compromise between precision of the results (central frequency is 30 Hz) and stability of the solution.

#### 4.3.2.1 Isotropic time-lapse velocity change

The tomography results for the isotropic parameterization of the three selected inlines are presented in Figure 4.8. We observe similar results as obtained when using 1D inversion: a velocity increase in the reservoir (due to compaction) and a decrease of velocity in the cap rock and the underburden as suggested in Sayers (2007) and Scott Jr (2007).

The three inlines, which have been inverted independently, show an overall coherent velocity perturbation result, which is consistent with the conceptual model of a globally depleted reservoir. Moreover, the line closest to the production wells shows a stronger time-lapse effect than the lines further away from the wells. Again, this is qualitatively consistent with the expected larger pressure drop closer to production wells. The overburden velocity decrease has been observed in many time-lapse studies, but it is generally supposed to be vertical with a large extension and an arch shape. Our tomographic results show a precise location of the velocity decrease in the cap rock at the top of the produced part of the reservoir. The positive reservoir anomaly is better seen in the first (western) inline than in the two others. Interestingly, we can observe in the two other (eastern) inlines that the connection between the two mains wells is weaker. This seems reasonable as some horizontal wells cross the first inline but do not reach the second or the third inline (Figure 4.4). This experiment provides good confidence on the quality of the data and therefore on the possibility of performing an anisotropic tomography.

#### 4.3.2.2 Anisotropic time-lapse velocity change

The anisotropic velocity change is parametrized with only three parameters ($q_1$, $q_3$, and $q_5$) and the results are presented in Figure 4.9. This simplification assumes a vertical symmetry axis.

The striking observation is the weak signal recovered on $q_1$ while $q_3$ shows amplitudes very similar to the inverted isotropic signal (Figure 4.8). The second obvious result is the very strong $q_5$ anomaly in the cap rock, which is not present in the underburden. These observations are consistent on the 3 inlines. As the acquisition is adapted to catch vertical and horizontal velocity changes, the fact that $q_3$ and $q_5$ show a high amplitude in the overburden and not $q_1$ can only be explained by an absence of slowdown in the vertical velocity. The observed horizontal velocity decrease in the cap rock seems to be incompatible with classical geomechanical models which suggests that the cap rock to be in vertically extending and in horizontally shortening.

At the reservoir top, the abrupt change in velocity from about 2 to 3 km/s induces a critical reflection angle of about 40°. This corresponds to the largest offsets recorded. The time-shifts estimation measured on a trace-by-trace basis can be hazardous if critical angle is reached and even more if the critical angle is different between the base and the monitor (rough estimate of 5° according to the estimated velocity changes). Nevertheless, during the tomography, the time-shifts are not estimated individually but are the consequences of an anisotropic velocity change. Therefore, the algorithm is not too sensitive to local phase changes between base and monitor. However, the horizontal velocity decrease ($q_5$) measured in the caprock (Figure 4.9G—I) is mainly driven by the reservoir top time-shifts of the largest offsets. These measurements are potentially

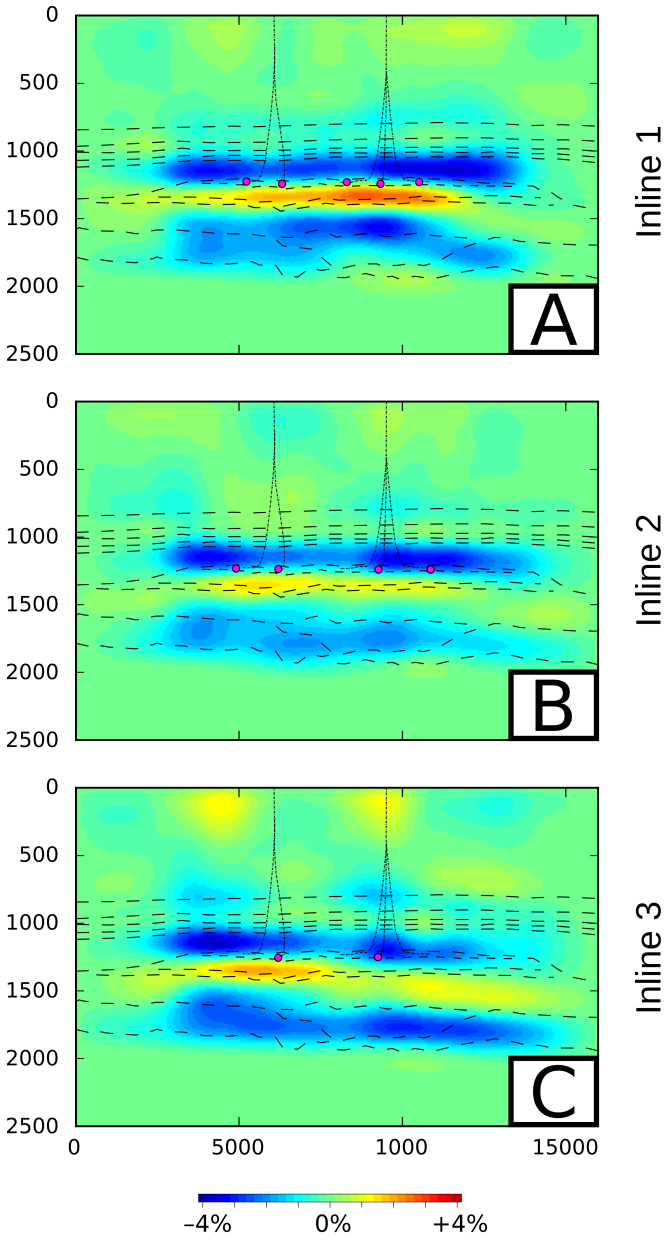


Figure 4.8: Isotropic velocity change retrieved by tomography for the three considered inlines. The horizons are drawn in dashed black lines. The red anomalies correspond to a velocity increase and they are mainly located in the reservoir. The blue anomalies correspond to a velocity slowdown and are located in the overburden and in the underburden. Projected wells are thin dashed lines; intersection between the wells are the image is indicated by purple dots.

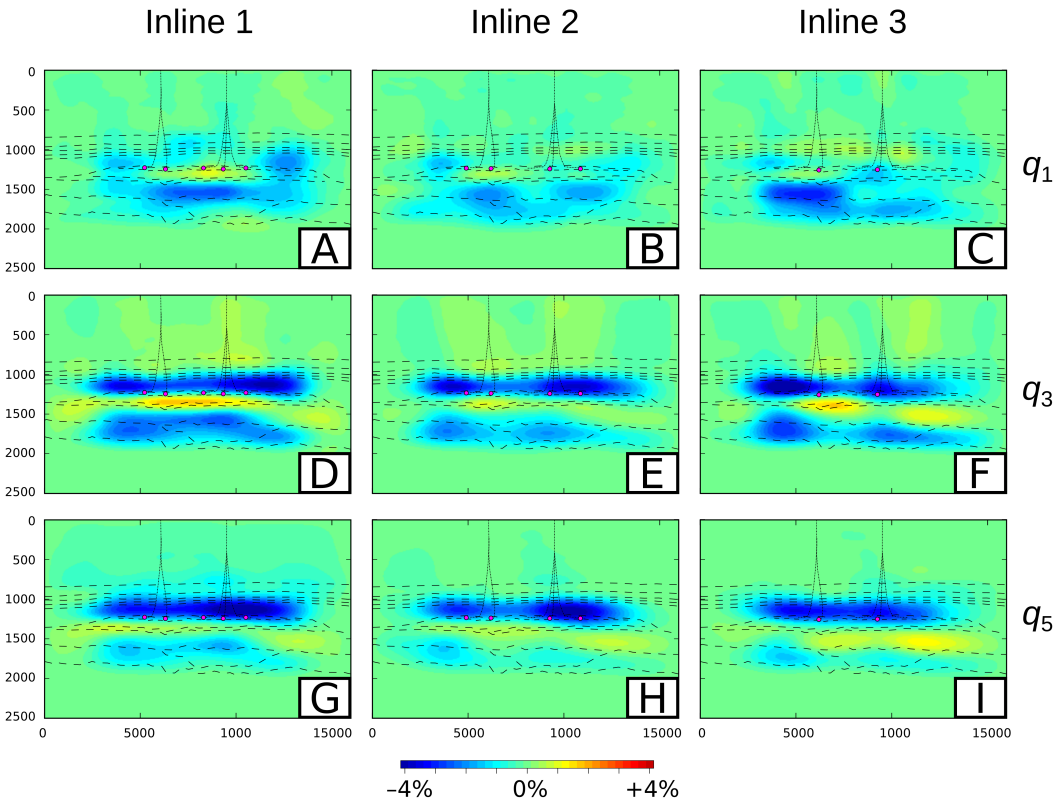


Figure 4.9: Anisotropic velocity change retrieved by tomography. Only the most sensitive parameters $q_1$, $q_3$, and $q_5$ are inverted which is equivalent to assuming a vertical symmetry. Note that $q_1$ i.e. the vertical velocity change is much weaker than the isotropic velocity change presented in Figure 4.8.

contaminated by phase changes between base and monitor surveys due to a variation of the overcritical angle which may jeopardize the interpretation of the horizontal velocity change.

In the underburden, only smaller angle range are available. The strong vertical velocity decrease (Figure 4.9A—C) and low horizontal velocity decrease (Figure 4.9G—I) could be an apparent anisotropy in the velocity change due to the lack of subhorizontal rays for retrieving the horizontal variations. Moreover, the strong reflectivity of the top of the carbonate platform makes it delicate to interpret the time shifts retrieved below the reservoir.

## 4.4 Discussions

Since $q_3$ shows the strongest anomalies in the cap rock, in the underburden and in the reservoir, the simplest interpretation is that they are due to cracks opening with an angle close to 45°. Is a single type of crack opening sufficient to explain the results observed on both the isotropic and the anisotropic inversions? To answer this question, we built new synthetics with anomalies of the same amplitudes (i.e. a 5% velocity change) but affecting only $q_3$, and inverted them both with an isotropic (Figure 4.10A) and an anisotropic inversion (Figure 4.10B—D). The global behavior observed on the synthetics matches closely the real data observations in the overburden and in the reservoir while disagreements remain in the underburden:

- The isotropic inversion shows a strong velocity decrease in the cap rock, a strong increase in the velocity in the reservoir and a slight velocity decrease in the underburden. The synthetic results match the real case isotropic inversion (Figure 4.7) for the reservoir and the overburden but they disagree for the underburden.
- The anisotropic inversion shows a strong anomaly in $q_3$ while $q_1$ is quasi mute. $q_5$ shows an anomaly in the cap rock while there is no anomaly in the underburden. The synthetic results match the real case anisotropic inversion (Figure 4.8) for the reservoir and the overburden but the $q_1$ anomaly in the underburden is not present in the synthetic inversion.

The similarity between synthetic results and real data is striking, even though we cannot expect a perfect match because (i) the synthetic model is over-simplified (ii) the stress regime in the reservoir and in the overburden is complex as the reservoir is inhomogeneous, (iii) measured time shifts on real data include noise not present on synthetic data. This means that the hypothesis of an existing set of fractures inducing a velocity slowdown preferentially around the 45° direction must be considered as a possible scenario.

The nonlinear elastic effect with the opening of microcracks such as those proposed by Hatchell and Bourne (2005) can explain the overburden time shifts. Previous 1D approaches used for time-lapse analysis are not able to distinguish between microstructures such as the cracks orientation distribution, their shapes, or the nature of the contact. Hatchell and Bourne (2005) propose that horizontal a dry cracks model is a good candidate because it has a strong effect on the vertical velocity change and the opening of such cracks is predicted by a geomechanical model of reservoir depletion under normal

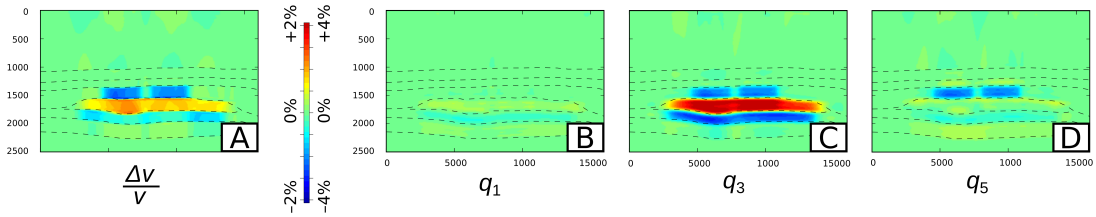


Figure 4.10: Isotropic velocity change (A) and anisotropic velocity change (B—D) retrieved in the synthetic case were only a single 45° velocity change is introduced. Results are very much similar to those obtained in the real data (Figure 4.8&4.9). In the anisotropic case, $q_1$ is almost mute, $q_3$ exhibits strong negative anomaly in the cap rock and the overburden and a high positive anomaly in the reservoir and $q_5$ shows high negative anomaly in the cap rock.

stress conditions. However, this model is not compatible with our observations as the vertical velocity change is low ($q_1$ is quasi mute). As often in ill-posed inverse problems, several explanations could probably be found. Some relate to the hypotheses made by our method, like the ray approximation and assuming an initial isotropic model. We are confident, however, that the consideration of small relative changes of elastic parameters justify the ray approximation, and that only very strong anisotropies in the initial model could affect the interpretation of the small observed velocity changes. It could still be interesting in future studies to compare more thoroughly and quantitatively the impact of the ray approximation by generating a synthetic time-lapse data with full elastic wave simulation. Another possibility could be to apply three-dimensional tomography, but, beyond the larger computational costs this would incur, this is not possible on this dataset because the time-lapse data do not include large offsets in the crossline direction.

The best remaining avenue to resolve the inconsistency between our observations and classical geomechanical models is to propose plausible alternative rock-physics models. The velocity change anisotropy induced by dry cracks is elliptical. Nevertheless, our real case inversion results show a 45° velocity change, which suggests that the anelliptic anisotropy in the velocity change could be due to the influence of cracks in water-saturated rock (Guéguen and Sarout, 2011). More precisely, Guéguen and Sarout (2011), model cracks as spheroidal inclusions with an aspect ratio between $10^{-2}$ and $10^{-3}$ and they expose the velocity change induced anisotropy for three basics crack configurations (identical cracks aligned in the same direction, identical cracks with random orientations and cracks randomly distributed in a zone with a given axis). Cracks randomly distributed in a zone with the vertical axis (i.e. vertical cracks) in a water-saturated rock model provide a good match in term of anisotropy with the one obtained in the real case anisotropic inversion. Compared to the penny-shaped cracks (the limit case of a spheroidal inclusion with a very small aspect ratio), the spheroidal inclusion in a water saturated rock induces a different velocity change anisotropy where there are aligned horizontally and vertically. Going further to quantitatively invert for the velocity change in term of crack orientation would require the knowledge of the crack density and the crack aspect ratio, which are unknown in our case.

At first sight, the presence of vertical cracks in the overburden seems incompatible

with the strain regime (vertical lengthening and horizontal shortening). Meanwhile, as the compacted area of the reservoir is about 100 m thick with a 12 km lateral extension, most of the strain is vertical strain: this means that the horizontal shortening is negligible, and the opening of vertical cracks is possible. We think that the measured anisotropy is the result of the reactivation of a preexisting fracture network. Indeed, the shale burial creates a triaxial stress regime such as the vertical stress is larger than the horizontal stress and subvertical cracks are created. The reservoir production probably reactivates preexisting weakness planes, which in our case, results in the opening of subvertical cracks filled with water.

## 4.5 Conclusion

Anisotropic time-lapse velocity changes due to reservoir compaction have been measured in a real case study. Despite the sensitivity of the tomographic method with respect to the picked horizons, the chosen trace alignment algorithm, the parametrizations, and the regularization weights, it has provided consistent results along the three studied inlines. We observe a velocity slowdown in the cap rock along horizontal and 45° directions. In the presence of such anisotropy, the classical 1D inversion algorithm used in time-lapse studies seems poorly adaptable to monitor the changes occurring in the cap rock, because they only consider vertical velocity changes.

Classical geomechanical models show that reservoir depletion may induce an opening of horizontal cracks in the cap rock, but the anisotropic time-lapse velocity change observed in our study are incompatible with this scenario. Our interpretation is that the overburden time shifts due to the reservoir production may be due to the reactivation of a pre-existing fracture network. Our tomography analysis of the overburden time shifts suggests that the time-lapse velocity change is likely a function of an intrinsic property of the rock (weakness planes). The proposed monitoring method provides a new insight for elaborating geomechanical models and stress-dependent rock-physics models calibrated with time-lapse seismic data.

# Appendices

## A Tomographic matrix examples

We present here a simple example on how to construct the tomographic matrix $A$. For the sake of simplicity, we present the construction procedure for only one ray which results in a single row tomographic matrix. The space is discretized in 4-by-4 regular grid as illustrated in Figure 4.11.

The ray trajectory is discretized by points sampled at a regular time interval $dt$. The ray travel time restricted to each cell of the grid is then approximated as the number of ray points within each cell times the sampling interval $dt$, and can be written in the

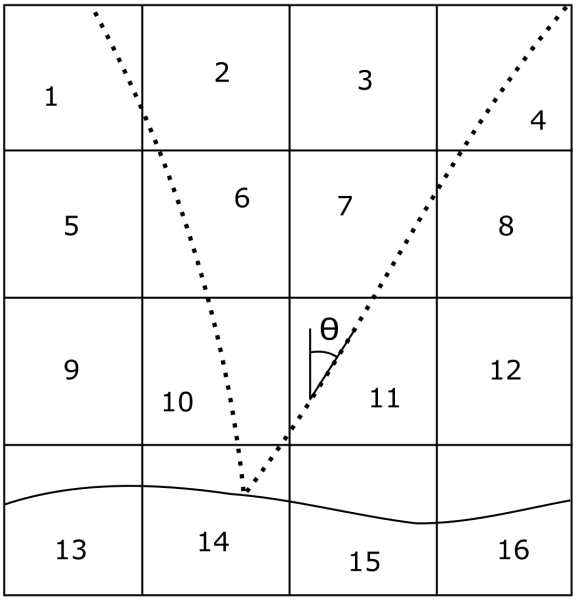


Figure 4.11: A simplistic example on the construction of the tomographic matrix. The model is divided into 16 cells. The reflected ray is sampled at regular time steps which are represented by dots. The traveltime spent by the ray at each cell is estimated by counting the number of dots in the cell and multiplying it by the time step.

matrix

$$\begin{pmatrix} 9 & 4 & 0 & 15 \\ 0 & 12 & 10 & 3 \\ 0 & 13 & 12 & 0 \\ 0 & 9 & 0 & 0 \end{pmatrix} dt \quad . \tag{4.16}$$

The error in one cell is bounded by $4dt$ if the ray crosses twice the same cell. To increase the tomography matrix accuracy, the regular grid can be finer, and the time interval can be shorter.

As a ray is represented by one row of the tomographic matrix such, we rewrite the matrix A-1 in the tomographic matrix as

$$A_{\text{iso}} = \begin{pmatrix} \vdots & \vdots & \vdots & \vdots & \vdots & \vdots & \vdots & \vdots & \vdots & \vdots & \vdots & \vdots & \vdots & \vdots & \vdots & \vdots \\ 9 & 4 & 0 & 15 & 0 & 12 & 10 & 3 & 0 & 13 & 12 & 0 & 0 & 9 & 0 & 0 \\ \vdots & \vdots & \vdots & \vdots & \vdots & \vdots & \vdots & \vdots & \vdots & \vdots & \vdots & \vdots & \vdots & \vdots & \vdots & \vdots \end{pmatrix} dt \quad . \tag{4.17}$$

In the presence of anisotropy, the velocity change $\frac{\Delta v}{v_0}$ is a function of the polar angle $\theta$ parameterized by five basis functions $f_k(\theta)$ as

$$\frac{\Delta v}{v_0}(\theta) = \sum_{k=1}^{5} q_k f_k(\theta) \quad . \tag{4.18}$$

The anisotropic tomographic matrix is the horizontal concatenation of five matrices which have the same dimension as the isotropic matrix but where all coefficients are

weighted by $f_k(\theta)$. To illustrate this, we write the $k$-part of one row of the anisotropic tomographic matrix $A^k_{\text{ani}}$ using the same rectangular representation as in equation 4.16

$$A^k_{\text{ani}} \begin{pmatrix} 9f_k(\theta_1) & 4f_k(\theta_2) & 0 & 15f_k(\theta_4) \\ 0 & 12f_k(\theta_6) & 10f_k(\theta_7) & 3f_k(\theta_8) \\ 0 & 12f_k(\theta_{10}^{\text{down}}) + f_k(\theta_{10}^{\text{up}}) & 12f_k(\theta_{11}) & 0 \\ 0 & 4f_k(\theta_{14}^{\text{down}}) + 5f_k(\theta_{14}^{\text{up}}) & 0 & 0 \end{pmatrix} dt \quad , \tag{4.19}$$

where $\theta_j$ is the polar angle of the ray at the cell $j$. For presentation purpose, we decompose the ray in two parts (one corresponding to the downgoing wavefield and on corresponding to the reflected upgoing wavefield). In practice, this angle is known at each ray discretization point, so the value $f_k(\theta)dt$ is accumulated during the ray tracing.

## B Case study seismic acquisition and preprocessing

The base and monitor vessels air guns shoot at a regular interval of 25 meters, which is translated in the data with common depth points (CDP) every 25 meters. Nevertheless, the air guns, the hydrophone arrays, and the number of streamers are different between the acquisitions of the base and the monitor. To address the source difference, the two acquisitions have been processed to comply with 4D standards in terms of equalization and spectrum. The distance between hydrophone arrays of the base and the monitor are respectively 33.33 and 25 meters which means that it is not possible to find a trace which corresponds to the same couple of source and receiver in both acquisitions. The traces were sorted into 43 offset classes (0 to 300, 300 to 350, ..., 2350 to 2400 meters). The first offset class has a larger interval and was excluded from the analysis, because the traces offset differences between the base and the monitor are often very large in this class, and it induces a moveout larger than the time-lapse time shifts. For the 42 other classes, the offset differences are reduced considerably but the induced normal moveout still needs to be corrected. Indeed, we study small overburden time shifts and this area is close enough to the surface to be affected by the offset difference. To solve this issue, we interpolated all the traces of these 42 offset classes to the middle offsets (325 m, 375 m, ..., 2375 m) by applying a time shift along the trace. This time shift $\delta t$ is estimated using the differentiation of the reflection traveltime with respect of the offset:

$$\delta t = \frac{x \delta x}{t v^2_{\text{RMS}}} \quad , \tag{4.20}$$

where $t$ is the two-way vertical traveltime (i.e. the trace depth in time), $v_{\text{RMS}}$ is the root mean square velocity, $\delta x$ is the offset of the trace and is the difference between the offset of the trace and the middle offset. This interpolation is only valid for reflected waves, which is the case in the considered dataset because the refracted energy is muted. After interpolation, the base and monitor traces share the same CDP and offset.

The interval velocity model (Figure 4.12) used for ray tracing was created from the $v_{\text{RMS}}$ model using smoothing and the Dix equation (an inverse approach procedure). Some far offset rays are presented to assess the ray angle coverage. The traveltime of the reflected rays are also used as a quality check (Figure 4.13).

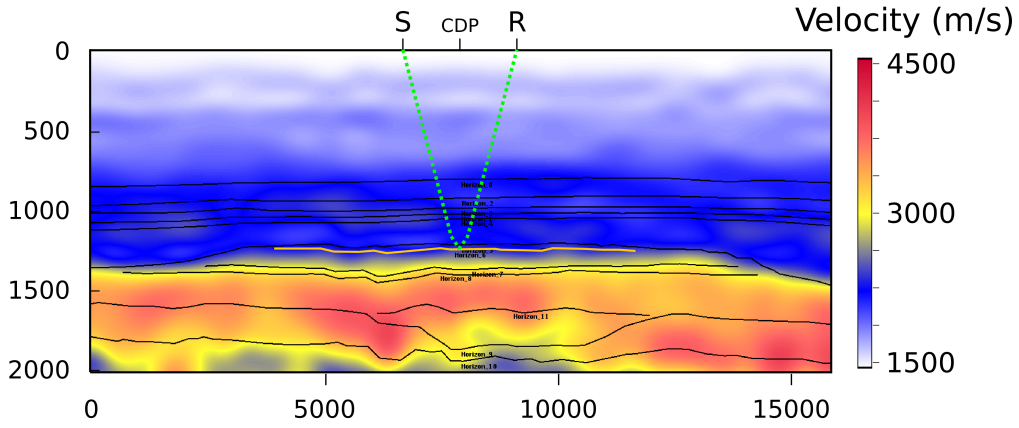


Figure 4.12: Internal velocity model used for ray tracing. A far offset ray is plotted in green.

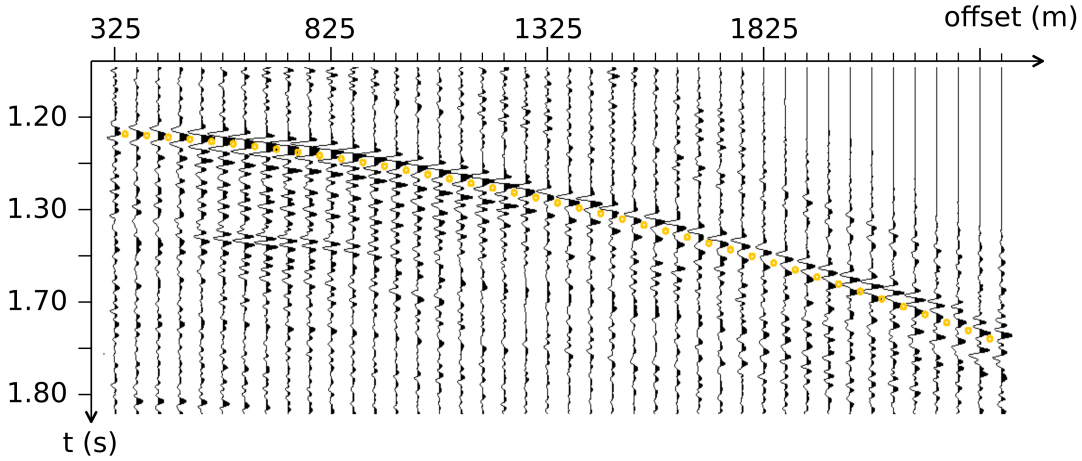


Figure 4.13: Prestack seismic traces of one CDP of the base. Ray computed traveltimes for one reflection surface are indicated with yellow circle.

# Conclusions

In this thesis, we present different ways of confronting the various data of the reservoir through inverse approaches. We investigate the geomechanical model building and we challenge the approximations made when matching the time-lapse seismic inversion results with the geomechanical model prediction. We propose a new ray-based anisotropic time-lapse seismic inversion method. We thereafter summarize the contributions of the thesis and discuss the open questions for future.

## Main contributions

### Understanding the time-lapse seismic data with a rock-physics model

Several mechanical laws have been established to understand the time-lapse seismic data. These laws take the form of rock-physics models where the elastic properties vary with the strain. The presented models are widely used to understand laboratory results on rock samples, but their usage on time-lapse seismic is complex. Indeed, the number of measurements (one for each monitor) is limited, the stress state change of the subsoil is not precisely known, and the rock mechanical properties inferred from log data and seismic data are not well known either. Moreover, the seismic elastic waves measurements on the field do not see the same scale as the ultrasonic measurements made in laboratory. The high dispersion between seismic and ultrasonic frequencies make their comparison difficult. As a result, R-factor measurements made at the laboratory fail to catch the amplitude of the overburden time-shifts observed on field cases. The time-lapse seismic inversion only measures the vertical longitudinal velocity change while laboratory measurements tends to measure the velocity change along three directions (0°, 45° and 90°) and for both longitudinal and transverse elastic waves. Finally, the impact of water in these models is ignored, and some authors (MacBeth et al., 2018) claim that the R-factor obtained in water-saturated rocks is similar to the one obtained in a dry rock, or it simply requires some correction. Effective models which represent the cracks with spheroidal inclusions show that this assumption is wrong, and that the crack aspect ratio is a fundamental controlling parameter. Nevertheless, crack aspect ratio is not known and it has never been addressed in time-lapse seismic studies. The third-order elasticity theory is used by Herwanger and Horne (2009) and Prioul et al. (2004) to understand 4D but laboratory experiments (Winkler and McGowan, 2004) show that this nonlinear elasticity model does not fit laboratory experiments in the wet case.

### Using the R-factor to update the geomechanical model

We use the R-factor to perform a geomechanical inversion using time-lapse seismic data. We invert for reservoir properties only because the elastic properties are actually not known but they are contained by the R-factor. Changes in these properties can be expressed by changing the R-factor. We show that the inverted reservoir properties depend on the product of the Biot's coefficient, the net-to-gross and the pore pressure change. Geomechanical simulations performed in chapter 1 show that the Poisson's ratio of the reservoir and the Young modulus contrast have a great influence on the stress change in the overburden.

### The impact of the in-situ stress

The initial stress state of the subsoil is simplified in geomechanical models. In the petroleum industry, it is generally assumed that the in-situ stress is Andersonian, which means that the major stress is along the vertical direction and the minor stresses are along the horizontal plane. In chapter 3, we extend the conclusions of Mazuyer et al. (2018) to integrate fault activity criteria. However, several observations made on the field, especially active faults, are incompatible with an Andersonian stress state. In a simplistic model, a non-Andersonian stress field which can explain the fault activity is retrieved. Nevertheless, our method is limited to 2D with a single fault close to the right boundary of our mechanical model. To tackle operational cases, we need to extend the method to 3D geometry, as done by Mazuyer et al. (2018). The plausible stress state which can explain fault activity is non-unique but the algorithm used is only able to retrieve one solution. This non-uniqueness needs to be addressed by other algorithms.

### Ray-based anisotropic time-lapse seismic inversion

In chapter 4, we proposed a new method to retrieve the anisotropic velocity change contained in time-lapse seismic data. Time-lapse studies measure the vertical velocity change only but we show that the time-lapse velocity change is anisotropic. Without knowing this anisotropic, finding the appropriate rock-physics model is difficult and time-lapse studies keep using the R-factor model which contained a mixture of geomechanical change such as the stress path and microstructural parameters. However, the stress-dependent rock-physics models which can explained the 4D time-shifts are various and non-unique. Retrieving the velocity change contained in time-lapse data in three directions (0°, 45°, and 90°) and these three velocity can be easily compared with laboratory experiments on rock samples or predicted velocity change made by effective elastic models. In the presented case study, we found that the overburden time-shifts can be explained by vertical cracks in a water-saturated rock. This model is very different from the horizontal cracks in a dry rock proposed by Hatchell et al. (2005).

## Perspectives

In a real case study, we show that the anisotropy allows to find a stress-dependent rock-physics model which can explain the 4D data. We only use the traveltime of P wave but other informations are available in time-lapse seismic. The phase and the

amplitude change can be studied as well. Moreover, the time-lapse analysis of the S-wave velocity change allows to retrieve the complete elastic perturbation rather than only the totally symmetric part. S-wave are interesting because they are sensitive to freely sliding cracks in contact for instance. A time-lapse amplitude change analysis can also be performed, but it would require high quality seismic data. Some operational studies (e.g. Røste et al., 2007) have shown an amplitude change while some other cases studies do not. Elastic inversion with full waveform inversion can also be used. This kind of inversion considers not just the P and S-waves but the full waveform, which integrates also the phase and the amplitude change. Nevertheless, this kind of inversion is much more expensive in terms of computational cost, than the ray approximation made in classical tomography (i.e the linearization of the traveltime perturbation along the reference ray). Initial anisotropy is also of great interest because overburden rocks are known to be anisotropic at typical reflection seismic resolution. But this anisotropy would change considerably our parametrization. An initial anisotropic velocity would require an anisotropic ray tracer which considers the slowness vector and the group velocity vector. Finally, a 3D approach could be considered. This would require an acquisition with large azimuthal angles. Nonetheless, our ray-based method can also be useful for laboratory experiments because it is difficult to measure the elastic properties of water-saturated shales (Sarout et al., 2014). Time-lapse seismic acquisition does not require to extract a rock-sample, as such it provides a non-destructive measurement of the elastic properties.

In terms of rock-physics models, we only consider penny-shaped cracks. In our time-lapse tomographic inversion, we propose a simple 3–parameters inversion which allows us to determine only a part of the microstructural parameters. In reality, the caprock is mainly shales where cracks do not necessarily exist. Conceptual advances are needed to understand why this model is valid on such material. If a crack model cannot be applied, one may wonder which time-lapse seismic parameter could be helpful to determine the appropriate microstructure? Can we still use an effective approach if the time-lapse effect is related to large scale fractures? In addition, the non-interaction approximation used in effective medium theory (Kachanov, 1992) does not distinguish connected cracks from independent ones. Connected cracks can lead to failure more easily so distinguishing them could allow to assess the rock failure. Can we use additional information, such as frequency effects, to distinguish between connected and disconnected cracks? This would provide essential information on the failure potential.

The proposed algorithms, either based on a least-square solver based on QR decomposition or an ensemble method based on a covariance matrix, allow to retrieve only one plausible solution. Can we imagine a method to explore all the space of solutions? EnKF is the optimal solver when the noise is Gaussian, but in real data, the noise is not Gaussian. Whereas this method seems to work on synthetic tests, we do not known the truth in real application case. How can we be sure that we retrieve the correct solution?

# Chapter A

# Appendix: The poroelastic problem in plane strain condition

The strain tensor $\varepsilon$ is the symmetric part of the displacement fields gradient. In indices notation, and following the Einstein summation convention over repeated indices, the strain tensor reads

$$\varepsilon_{ij} = \frac{1}{2}\left(\frac{\partial u_i}{\partial x_j} + \frac{\partial u_j}{\partial x_i}\right) \quad , \tag{A.1}$$

where $i$ and $j$ are indices representing the three directions of the space. For simplicity, we consider the base $(e_x e_y e_z)$ with a plane contained in the $e_x e_z$ plane.

The strain compatibility equation (A.1) can be written by eliminating the displacements in the previous equation

$$\frac{\partial^2 \varepsilon_{xx}}{\partial z^2} + \frac{\partial^2 \varepsilon_{zz}}{\partial x^2} - 2\frac{\partial^2 \varepsilon_{xz}}{\partial x \partial z} = 0 \quad . \tag{A.2}$$

Any strain field derived from a displacement field is a solution of this equation. In the following, the aim is to rewrite the compatibility equation in term of stresses. A saturated porous medium is considered, where the stresses are distributed between the solid skeleton (effective stress $\sigma'$) and the fluid contained in the pores as a fluid pressure $p$. The elastic behavior of the solid skeleton can be expressed with Hooke's law. This law links the strain to the effective stress $\sigma'$. For a linear isotropic material, Hooke's law takes the form

$$\varepsilon_{ij} = \frac{1+\nu}{E}\sigma'_{ij} - \frac{\nu}{E}\sigma'_{kk}\delta_{ij} \quad , \tag{A.3}$$

where $E$ is the Young modulus, and $\nu$ is the Poisson's ratio. In plane strain condition, the out-of-plane strain is equal to zero ($\varepsilon_{yy} = 0$). Hence, the out-of-plane stress is $\sigma'_{yy} = \nu(\sigma'_{xx} + \sigma'_{zz})$.

The strain compatibility equation can be written is term of effective stresses as

$$(1-\nu)\left(\frac{\partial^2 \sigma'_{xx}}{\partial z^2} + \frac{\partial^2 \sigma'_{zz}}{\partial x^2}\right) - \nu\left(\frac{\partial^2 \sigma'_{xx}}{\partial x^2} + \frac{\partial^2 \sigma'_{zz}}{\partial z^2}\right) - 2\frac{\partial^2 \sigma'_{xz}}{\partial x \partial z} = 0 \tag{A.4}$$

Considering a body force $\boldsymbol{f_b}$, the equilibrium equation of the solid skeleton is

$$\operatorname{div} \boldsymbol{\sigma'} - \alpha \, \mathbf{grad}\, p + \boldsymbol{f_b} = 0 \tag{A.5}$$

The divergence of this equation gives

$$\frac{\partial^2 \sigma'_{xx}}{\partial x^2} + \frac{\partial^2 \sigma'_{zz}}{\partial z^2} - 2\frac{\partial^2 \sigma'_{xz}}{\partial x \partial z} - \alpha \Delta p + \operatorname{div} \boldsymbol{f_b} = 0 \tag{A.6}$$

Combining the compatibility equation in term of effective stresses and the previous equation allows to write the following Laplace equation

$$\Delta \left( \sigma'_{xx} + \sigma'_{zz} - \frac{\alpha p}{1-\nu} \right) = -\frac{1}{1-\nu} \operatorname{div} \boldsymbol{f_b} \tag{A.7}$$

which can be written in term of total stress as

$$\Delta \left( \sigma_{xx} + \sigma_{zz} + 2\eta p \right) = -\frac{1}{1-\nu} \operatorname{div} \boldsymbol{f_b} \tag{A.8}$$

where $\eta = \frac{\alpha(1-2\nu)}{2(1-\nu)}$ is the poroelastic stress coefficient (Merxhani, 2016). In a homogeneous medium, the stress field is independent of the Young modulus. When the stress change is the result of a reservoir pore pressure drop, the body forces vanish, and the stress change only depends on the poroelastic stress coefficient $\eta$.

# Bibliography


K. Aki and P. G. Richards. *Quantitative seismology.* University Science Books, 2002.

N. A. Al-Shayea. Effects of testing methods and conditions on the elastic properties of limestone rock. *Engineering geology*, 74(1-2): 139–156, 2004.

T. Alkhalifah. Seismic data processing in vertically inhomogeneous TI media. *Geophysics*, 62(2): 662–675, 1997.

T. Alkhalifah and R.-É. Plessix. A recipe for practical full-waveform inversion in anisotropic media: An analytical parameter resolution study. *Geophysics*, 79(3): R91–R101, 2014.

A. Auger and N. Hansen. Theory of evolution strategies: a new perspective. In *Theory of Randomized Search Heuristics: Foundations and Recent Developments*, p. 289–325. World Scientific, 2011.

G. Backus. A geometrical picture of anisotropic elastic tensors. *Reviews of geophysics*, 8(3): 633–671, 1970.

O. I. Barkved and T. Kristiansen. Seismic time-lapse effects and stress changes: Examples from a compacting reservoir. *The Leading Edge*, 24(12): 1244–1248, 2005.

A. Barré de Saint-Venant. Etablissement élémentaire des formules et équations générales de la théorie de l'élasticité des corps solides. *Leçons Donnéesa l'Ecole des Ponts et Chaussées sur l'Application de la Mécanique par CLMH Navier, Third Edition, Paris*, 1864.

E. Beltrami. *Sull'interpretazione meccanica delle formole di Maxwell: memoria.* Tipografia Gamberini e Parmeggiani, 1886.

H. M. Benz, N. D. McMahon, R. C. Aster, D. E. McNamara, and D. B. Harris. Hundreds of earthquakes per day: The 2014 Guthrie, Oklahoma, earthquake sequence. *Seismological Research Letters*, 86(5): 1318–1325, 2015.

M. A. Biot. General theory of three-dimensional consolidation. *Journal of applied physics*, 12(2): 155–164, 1941.

D. R. Bland. *Nonlinear dynamic elasticity.* Blaisdell publishing company, 1969.

B. Bonner. Shear wave birefringence in dilating granite. *Geophysical Research Letters*, 1(5): 217–220, 1974.

J. Borgomano. *Dispersion des modules élastiques de carbonates saturés : étude expérimentale et modélisation.* Thèse, PSL Research University, 2018.

A. Botella, B. Lévy, and G. Caumon. Indirect unstructured hex-dominant mesh generation using tetrahedra recombination. *Computational Geosciences*, 20(3): 437–451, 2016.

A. Bouziat, N. Guy, J. Frey, D. Colombo, P. Colin, M.-C. Cacas-Stentz, and T. Cornu. An assessment of stress states in passive margin sediments: Iterative hydro-mechanical simulations on basin models and implications for rock failure predictions. *Geosciences*, 9(11): 469, 2019.

A. F. Bower. *Applied mechanics of solids.* CRC Press, 2009.

R. S. Carmichael. *Handbook of Physical Properties of Rocks (1982): Volume II.* CRC press, 2017.

V. Červenỳ. *Seismic ray theory.* Cambridge university press, 2001.

A. W.-K. Chan. *Production-induced reservoir compaction, permeability loss and land surface subsidence.* PhD thesis, Stanford University Stanford, CA, USA, 2004.

C. Chang and H. Conway. Stress analysis of an infinite plate containing an elastic rectangular inclusion. *Acta Mechanica*, 8(3-4): 160–173, 1969.

C. t. Chapman and R. Pratt. Traveltime tomography in anisotropic media—I. Theory. *Geophysical Journal International*, 109(1): 1–19, 1992.

J. Charléty, N. Cuenot, L. Dorbath, C. Dorbath, H. Haessler, and M. Frogneux. Large earthquakes during hydraulic stimulations at the geothermal site of Soultz-Sous-Forêts. *International Journal of Rock Mechanics and Mining Sciences*, 44(8): 1091–1105, 2007.

C. Cheng and D. H. Johnston. Dynamic and static moduli. *Geophysical Research Letters*, 8(1): 39–42, 1981.

B. Christaras, F. Auger, and E. Mosse. Determination of the moduli of elasticity of rocks. Comparison of the ultrasonic velocity and mechanical resonance frequency methods with direct static methods. *Materials and Structures*, 27(4): 222–228, 1994.

M. Ciccotti and F. Mulargia. Differences between static and dynamic elastic moduli of a typical seismogenic rock. *Geophysical Journal International*, 157(1): 474–477, 2004.

N. Cuenot, C. Dorbath, and L. Dorbath. Analysis of the microseismicity induced by fluid injections at the EGS site of Soultz-Sous-Forêts (Alsace, France): implications for the characterization of the geothermal reservoir properties. *Pure and Applied Geophysics*, 165(5): 797–828, 2008.

H. P. G. Darcy. *Les Fontaines publiques de la ville de Dijon. Exposition et application des principes à suivre et des formules à employer dans les questions de distribution d'eau, etc.* V. Dalamont, 1856.

S. De Gennaro, A. Onaisi, A. Grandi, L. Ben-Brahim, and V. Neillo. 4D reservoir geomechanics: a case study from the HP/HT reservoirs of the Elgin and Franklin fields. *First Break*, 26(12): 53–59, 2008.

C. Delle Piane, D. Dewhurst, A. Siggins, and M. Raven. Stress-induced anisotropy in brine saturated shale. *Geophysical Journal International*, 184(2): 897–906, 2011.

D. Dempsey and J. Suckale. Physics-based forecasting of induced seismicity at groningen gas field, the netherlands. *Geophysical Research Letters*, 44(15): 7773–7782, 2017.

D. N. Dewhurst and A. F. Siggins. Impact of fabric, microcracks and stress field on shale anisotropy. *Geophysical Journal International*, 165(1): 135–148, 2006.

U. Djuraev, S. R. Jufar, and P. Vasant. A review on conceptual and practical oil and gas reservoir monitoring methods. *Journal of Petroleum Science and Engineering*, 152: 586–601, 2017.

J. Du, R. Wong, et al. Application of strain-induced permeability model in a coupled geomechanics-reservoir simulator. *Journal of Canadian Petroleum Technology*, 46 (12), 2007.

O. Dybvik, L. Gemmer, U. Theune, and S. Østmo. Establishing a geomechanical workflow for time-lapse modelling of an HPHT field. In *71st EAGE Conference and Exhibition incorporating SPE EUROPEC 2009*, 2009.

H. Ebaid, M. Nasser, P. Hatchell, and D. Stanley. Time-lapse seismic makes a significant business impact at Holstein. In *SEG Technical Program Expanded Abstracts 2009*, p. 3810–3814. Society of Exploration Geophysicists, 2009.

J. Edgar and N. Mastio. Time-lapse velocity change tomography. In *79th EAGE Conference and Exhibition 2017*, p. 1–5, 2017.

A. C. Eringen, E. S. Suhubi, and S. Cowin. Elastodynamics (Volume 1, Finite Motions). *Journal of Applied Mechanics*, 42(3): 748–748, 1975.

G. Evensen. The ensemble kalman filter: Theoretical formulation and practical implementation. *Ocean dynamics*, 53(4): 343–367, 2003.

A. Every and W. Sachse. Sensitivity of inversion algorithms for recovering elastic constants of anisotropic solids from longitudinal wavespeed data. *Ultrasonics*, 30(1): 43–48, 1992.

E. Fjær. Static and dynamic moduli of a weak sandstone. *Geophysics*, 74(2): WA103–WA112, 2009.

E. Fjær. Relations between static and dynamic moduli of sedimentary rocks. *Geophysical Prospecting*, 67(1): 128–139, 2019.

D. C.-L. Fong and M. Saunders. LSMR: An iterative algorithm for sparse least-squares problems. *SIAM Journal on Scientific Computing*, 33(5): 2950–2971, 2011.

J. Fortin, S. Stanchits, G. Dresen, and Y. Guéguen. Acoustic emission and velocities associated with the formation of compaction bands in sandstone. *Journal of Geophysical Research: Solid Earth*, 111(B10), 2006.

J. Fortin, Y. Guéguen, and A. Schubnel. Effects of pore collapse and grain crushing on ultrasonic velocities and Vp/Vs. *Journal of Geophysical Research: Solid Earth*, 112 (B8), 2007.

F. Fournier, P. Léonide, L. Kleipool, R. Toullec, J. J. Reijmer, J. Borgomano, T. Klootwijk, and J. Van Der Molen. Pore space evolution and elastic properties of platform carbonates (Urgonian limestone, Barremian–Aptian, SE France). *Sedimentary geology*, 308: 1–17, 2014.

R. Fuck, A. Bakulin, and I. Tsvankin. Theory of traveltime shifts around compacting reservoirs: 3d solutions for heterogeneous anisotropic media. *Geophysics*, 74(1): D25–D36, 2009.

R. J. Greaves and T. J. Fulp. Three-dimensional seismic monitoring of an enhanced oil recovery process. *Geophysics*, 52(9): 1175–1187, 1987.

R. J. Greaves, T. J. Fulp, and P. Head. Three-dimensional seismic monitoring of an enhanced oil recovery project. In *SEG Technical Program Expanded Abstracts 1983*, p. 476–478. Society of Exploration Geophysicists, 1983.

D. Gubbins. *Time series analysis and inverse theory for geophysicists*. Cambridge University Press, 2004.

Y. Guéguen and M. Kachanov. Effective elastic properties of cracked rocks—an overview. In *Mechanics of crustal rocks*, p. 73–125. Springer, 2011.

Y. Guéguen and V. Palciauskas. *Introduction to the Physics of Rocks*. Princeton University Press, 1994.

Y. Guéguen and J. Sarout. Crack-induced anisotropy in crustal rocks: predicted dry and fluid-saturated Thomsen's parameters. *Physics of the Earth and Planetary Interiors*, 172(1-2): 116–124, 2009.

Y. Guéguen and J. Sarout. Characteristics of anisotropy and dispersion in cracked medium. *Tectonophysics*, 503(1-2): 165–172, 2011.

Y. Guglielmi, F. Cappa, and D. Amitrano. High-definition analysis of fluid-induced seismicity related to the mesoscale hydromechanical properties of a fault zone. *Geophysical Research Letters*, 35(6), 2008.

J. Guilbot and B. Smith. 4-D constrained depth conversion for reservoir compaction estimation: Application to Ekofisk Field. *The Leading Edge*, 21(3): 302–308, 2002.

I. N. Gupta. Seismic velocities in rock subjected to axial loading up to shear fracture. *Journal of Geophysical Research*, 78(29): 6936–6942, 1973.

D. Hale. Dynamic warping of seismic images. *Geophysics*, 78(2): S105–S115, 2013.

S. A. Hall, C. MacBeth, O. I. Barkved, and P. Wild. Time-lapse seismic monitoring of compaction and subsidence at Valhall through cross-matching and interpreted warping of 3d streamer and OBC data. In *SEG Technical Program Expanded Abstracts 2002*, p. 1696–1699. Society of Exploration Geophysicists, 2002.

P. Hatchell and S. Bourne. Rocks under strain: Strain-induced time-lapse time shifts are observed for depleting reservoirs. *The Leading Edge*, 24(12): 1222–1225, 2005.

P. Hatchell, R. Kawar, and A. Savitski. Integrating 4d seismic, geomechanics and reservoir simulation in the Valhall oil field. In *67th EAGE Conference & Exhibition*, 2005.

P. Hatchell, O. Jorgensen, L. Gommesen, and J. Stammeijer. Monitoring reservoir compaction from subsidence and time-lapse time shifts in the Dan field. In *SEG Technical Program Expanded Abstracts 2007*, p. 2867–2871. Society of Exploration Geophysicists, 2007.

C. Hawkes, P. McLellan, U. Zimmer, S. Bachu, et al. Geomechanical factors affecting geological storage of CO2 in depleted oil and gas reservoirs. In *Canadian International Petroleum Conference*, 2004.

K. Hawkins, S. Howe, S. Hollingworth, G. Conroy, L. Ben-Brahim, C. Tindle, N. Taylor, G. Joffroy, and A. Onaisi. Production-induced stresses from time-lapse time shifts: A geomechanics case study from Franklin and Elgin fields. *The Leading Edge*, 26(5): 655–662, 2007.

R. Hearmon. 'third-order' elastic coefficients. *Acta Crystallographica*, 6(4): 331–340, 1953.

J. Herwanger and N. Koutsabeloulis. Seismic geomechanics: How to build and calibrate geomechanical models using 3d and 4d seismic data. *EAGE publications*, 2011.

J. Herwanger, C. Schiøtt, R. Frederiksen, O. Vejbæk, R. Wold, H. Hansen, E. Palmer, and N. Koutsabeloulis. Applying time-lapse seismic methods to reservoir management and field development planning at South Arne, Danish North Sea. In *Geological Society, London, Petroleum Geology Conference series*, vol. 7, p. 523–535, 2010.

J. V. Herwanger and S. A. Horne. Linking reservoir geomechanics and time-lapse seismics: Predicting anisotropic velocity changes and seismic attributes. *Geophysics*, 74 (4): W13–W33, 2009.

N. Hodgson, C. MacBeth, L. Duranti, J. Rickett, and K. Nihei. Inverting for reservoir pressure change using time-lapse time strain: Application to Genesis field, Gulf of Mexico. *The Leading Edge*, 26(5): 649–652, 2007.

A. Holland. *Examination of possibly induced seismicity from hydraulic fracturing in the Eola Field, Garvin County, Oklahoma.* Oklahoma Geological Survey, 2011.

R. M. Holt, E. Fjær, and A.-K. Furre. Laboratory simulation of the influence of earth stress changes on wave velocities. In *Seismic anisotropy*, p. 180–202. Society of Exploration Geophysicists, 1996.

R. M. Holt, A. Bauer, and A. Bakk. Stress-path-dependent velocities in shales: Impact on 4d seismic interpretation. *Geophysics*, 83(6): MR353–MR367, 2018.

D. S. Hughes and J. Kelly. Second-order elastic deformation of solids. *Physical review*, 92(5): 1145, 1953.

A. L. Janssen, B. A. Smith, G. W. Byerley, et al. Measuring seismic velocity sensitivity to production-induced strain at the Ekofisk field. In *Offshore Technology Conference*, 2007.

J. Jech and I. Pšenčík. First-order perturbation method for anisotropic media. *Geophysical Journal International*, 99(2): 369–376, 1989.

C. Julio, G. Caumon, and M. Ford. Sampling the uncertainty associated with segmented normal fault interpretation using a stochastic downscaling method. *Tectonophysics*, 639: 56–67, 2015.

M. Kachanov. Continuum model of medium with cracks. *Journal of the engineering mechanics division*, 106(5): 1039–1051, 1980.

M. Kachanov. Effective elastic properties of cracked solids: critical review of some basic concepts. *Applied Mechanics Reviews*, 45(8): 304–335, 1992.

M. L. Kachanov, B. Shafiro, and I. Tsukrov. *Handbook of elasticity solutions*. Springer Science & Business Media, 2013.

V. Kazei and T. Alkhalifah. Waveform inversion for orthorhombic anisotropy with P waves: feasibility and resolution. *Geophysical Journal International*, 213(2): 963–982, 2018.

S. C. Key, S. H. Pederson, and B. A. Smith. Adding value to reservoir management with seismic monitoring technologies. *The Leading Edge*, 17(4): 515–519, 1998.

T. Kristiansen, O. Barkved, M. Landrø, and L. Amundsen. Reservoir monitoring technology part v: Linking seismic response to geomechanics. *GEO ExPro Magazine*, 2009.

L. D. Landau and E. Lifshits. Theoretical Physics, Vol. 7, Theory of Elasticity. *Science, Moscow, Main editorial board for physical and mathematical literature*, 1987.

M. Landrø and J. Stammeijer. Quantitative estimation of compaction and velocity changes using 4d impedance and traveltime changes. *Geophysics*, 69(4): 949–957, 2004.

S. Le Bégat and V. Farra. P-wave traveltime and polarization tomography of VSP data. *Geophysical Journal International*, 131(1): 100–114, 1997.

H. Ledbetter. Dynamic vs. static Young's moduli: a case study. *Materials Science and Engineering: A*, 165(1): L9–L10, 1993.

D. Lockner, J. Walsh, and J. Byerlee. Changes in seismic velocity and attenuation during deformation of granite. *Journal of Geophysical Research*, 82(33): 5374–5378, 1977.

P. Longuemare, M. Mainguy, P. Lemonnier, A. Onaisi, C. Gérard, and N. Koutsabeloulis. Geomechanics in reservoir simulation: overview of coupling methods and field case study. *Oil & Gas Science and Technology*, 57(5): 471–483, 2002.

A. E. H. Love. *A treatise on the mathematical theory of elasticity.* Cambridge University Press, 1944.

C. MacBeth. *Multi-component VSP analysis for applied seismic anisotropy*, vol. 26. Elsevier, 2002.

C. MacBeth, A. Kudarova, and P. Hatchell. A semi-empirical model of strain sensitivity for 4d seismic interpretation. *Geophysical Prospecting*, 66(7): 1327–1348, 2018.

C. MacBeth, M.-D. Mangriotis, and H. Amini. Post-stack 4d seismic time-shifts: Interpretation and evaluation. *Geophysical Prospecting*, 67(1): 3–31, 2019.

L. Maerten, F. Maerten, M. Lejri, and P. Gillespie. Geomechanical paleostress inversion using fracture data. *Journal of Structural Geology*, 89: 197–213, 2016.

J.-L. Mallet. Space–time mathematical framework for sedimentary geology. *Mathematical geology*, 36(1): 1–32, 2004.

R. Martin III, R. Haupt, et al. Static and dynamic elastic moduli in granite: The effect of strain amplitude. In *1st North American Rock Mechanics Symposium*, 1994.

J. Martínez-Martínez, D. Benavente, and M. García-del Cura. Comparison of the static and dynamic elastic modulus in carbonate rocks. *Bulletin of engineering geology and the environment*, 71(2): 263–268, 2012.

S. K. Matthai, A. A. Mezentsev, M. Belayneh, et al. Finite element-node-centered finite-volume two-phase-flow experiments with fractured rock represented by unstructured hybrid-element meshes. *SPE Reservoir Evaluation & Engineering*, 10(06): 740–756, 2007.

G. Mavko, T. Mukerji, and J. Dvorkin. *The rock physics handbook.* Cambridge University Press, 2019.

A. Mazuyer, R. Giot, P. Cupillard, P. Thore, M. Conin, and Y. Leroy. Integrated inverse method to estimate virgin stress state in reservoirs and overburden. In *79th EAGE Conference and Exhibition 2017*, p. 1–5, 2017.

A. Mazuyer, P. Cupillard, R. Giot, M. Conin, Y. Leroy, and P. Thore. Stress estimation in reservoirs using an integrated inverse method. *Computers & Geosciences*, 114: 30–40, 2018.

A. Merxhani. An introduction to linear poroelasticity. *arXiv preprint arXiv:1607.04274*, 2016.

T. D. Mikesell, A. E. Malcolm, D. Yang, and M. M. Haney. A comparison of methods to estimate seismic phase delays: Numerical examples for coda wave interferometry. *Geophysical Journal International*, 202(1): 347–360, 2015.

R. D. Mindlin. Force at a point in the interior of a semi-infinite solid. *physics*, 7(5): 195–202, 1936.

F. D. Murnaghan. Finite deformations of an elastic solid. *American Journal of Mathematics*, 59(2): 235–260, 1937.

F. D. Murnaghan. *Finite deformation of an elastic solid*. Wiley, 1951.

G. Nolet. *Seismic tomography: with applications in global seismology and exploration geophysics*, vol. 5. Springer, 1987.

R. L. Nowack and I. Pšenčík. Perturbation from isotropic to anisotropic heterogeneous media in the ray approximation. *Geophysical Journal International*, 106(1): 1–10, 1991.

W. Nowacki. Thermoelasticity, 1986.

J.-W. Oh and T. Alkhalifah. The scattering potential of partial derivative wavefields in 3-D elastic orthorhombic media: an inversion prospective. *Geophysical Journal International*, 206(3): 1740–1760, 2016.

M. Pervukhina, D. Dewhurst, B. Gurevich, U. Kuila, T. Siggins, M. Raven, and H. M. Nordgård-Bolås. Stress-dependent elastic properties of shales: Measurement and modeling. *The Leading Edge*, 27(6): 772–779, 2008.

O. Podgornova, S. Leaney, and L. Liang. Resolution of VTI anisotropy with elastic full-waveform inversion: theory and basic numerical examples. *Geophysical Journal International*, 214(1): 200–218, 2018.

V. Prieux, R. Brossier, Y. Gholami, S. Operto, J. Virieux, O. Barkved, and J. Kommedal. On the footprint of anisotropy on isotropic full waveform inversion: the valhall case study. *Geophysical Journal International*, 187(3): 1495–1515, 2011.

R. Prioul, A. Bakulin, and V. Bakulin. Nonlinear rock physics model for estimation of 3D subsurface stress in anisotropic formations: Theory and laboratory verification. *Geophysics*, 69(2): 415–425, 2004.

M. J. Pyrcz and C. V. Deutsch. *Geostatistical reservoir modeling, Second Edition*. Oxford University Press, 2014.

J. R. Rice and M. P. Cleary. Some basic stress diffusion solutions for fluid-saturated elastic porous media with compressible constituents. *Reviews of Geophysics*, 14(2): 227–241, 1976.

J. Rickett and D. Lumley. Cross-equalization data processing for time-lapse seismic reservoir monitoring: A case study from the gulf of mexico. *Geophysics*, 66(4): 1015–1025, 2001.

J. Rickett, L. Duranti, T. Hudson, B. Regel, and N. Hodgson. 4D time strain and the seismic signature of geomechanical compaction at Genesis. *The Leading Edge*, 26(5): 644–647, 2007.

P. Ringrose and M. Bentley. *Reservoir model design*. Springer, 2016.

A. Rodriguez-Herrera, N. Koutsabeloulis, A. Onaisi, J. Fiore, and F. Selva. Stress-induced signatures in 4D seismic data: Evidence of overburden stress arching. In *SEG Technical Program Expanded Abstracts 2015*, p. 5368–5372. Society of Exploration Geophysicists, 2015.

J.-P. Rolando, G. Massonnat, J. Grasso, F. Odonne, R. Meftahi, et al. Characterization and modelling of increasing permeability while producing a gas fractured reservoir. In *SPE Annual Technical Conference and Exhibition*, 1997.

T. Røste and G. Ke. Overburden 4d time shifts—Indicating undrained areas and fault transmissibility in the reservoir. *The Leading Edge*, 36(5): 423–430, 2017.

T. Røste, A. Stovas, and M. Landrø. Estimation of layer thickness and velocity changes using 4d prestack seismic data. *Geophysics*, 71(6): S219–S234, 2006.

T. Røste, M. Landrø, and P. Hatchell. Monitoring overburden layer changes and fault movements from time-lapse seismic data on the Valhall field. *Geophysical Journal International*, 170(3): 1100–1118, 2007.

T. Røste, O. P. Dybvik, and O. K. Søreide. Overburden 4D time shifts induced by reservoir compaction at Snorre field. *The Leading Edge*, 34(11): 1366–1374, 2015.

E. H. Saenger, O. S. Krüger, and S. A. Shapiro. Effective elastic properties of fractured rocks: Dynamic vs. static considerations. In *SEG Technical Program Expanded Abstracts 2006*, p. 1948–1952. Society of Exploration Geophysicists, 2006.

J. Sarout and Y. Guéguen. Anisotropy of elastic wave velocities in deformed shales: Part 1—experimental results. *Geophysics*, 73(5): D75–D89, 2008.

J. Sarout, L. Esteban, C. Delle Piane, B. Maney, and D. N. Dewhurst. Elastic anisotropy of Opalinus clay under variable saturation and triaxial stress. *Geophysical Journal International*, 198(3): 1662–1682, 2014.

M. R. Sastre and L. Calleja. Caracterización del comportamiento elástico de materiales pizarrosos del Sinclinal de Truchas mediante ultrasonidos. *Trabajos de Geología*, 24: 153–164, 2004.

C. M. Sayers. Asymmetry in the time-lapse seismic response to injection and depletion. *Geophysical Prospecting*, 55(5): 699–705, 2007.

T. E. Scott Jr. The effects of stress paths on acoustic velocities and 4d seismic imaging. *The Leading Edge*, 26(5): 602–608, 2007.

A. Settari, F. Mourits, et al. A coupled reservoir and geomechanical simulation system. *Spe Journal*, 3(03): 219–226, 1998.

G. Simmons and W. F. Brace. Comparison of static and dynamic measurements of compressibility of rocks. *Journal of Geophysical Research*, 70(22): 5649–5656, 1965.

I. Song, M. Suh, Y.-K. Woo, and T. Hao. Determination of the elastic modulus set of foliated rocks from ultrasonic velocity measurements. *Engineering Geology*, 72(3-4): 293–308, 2004.

J. P. Spivey and W. J. Lee. *Applied well test interpretation*. Society of Petroleum Engineers Richardson, TX, 2013.

R. Staples, J. Ita, R. Burrell, and R. Nash. Monitoring pressure depletion and improving geomechanical models of the Shearwater field using 4d seismic. *The Leading Edge*, 26(5): 636–642, 2007.

A. Sulak, J. Danielsen, et al. Reservoir aspects of Ekofisk subsidence. In *Offshore Technology Conference*, 1988.

H. Sun and R. Prioul. Relating shear sonic anisotropy directions to stress in deviated wells. *Geophysics*, 75(5): D57–D67, 2010.

S. Takahashi and R. Motegi. Measurement of third-order elastic constants and applications to loaded structural materials. *SpringerPlus*, 4(1): 325, 2015.

A. Tarantola. *Inverse Problem Theory and methods for model parameter estimation*, vol. 89. SIAM, 2005.

K. Terzaghi. *Erdbaumechanik auf bodenphysikalischer grundlage*. F. Deuticke, 1925.

K. Terzaghi. Relation between soil mechanics and foundation engineering. In *Proceedings of the International Conference on Soil Mechanics and Foundation Engineering*, vol. 3, p. 13–18, 1936.

L. Thomsen. Weak elastic anisotropy. *Geophysics*, 51(10): 1954–1966, 1986.

P. Thore. Uncertainty in seismic inversion: What really matters? *The Leading Edge*, 34(9): 1000–1004, 2015.

P. Thore and C. Hubans. 4d seismic-to-well tying, a key step towards 4d inversion. *Geophysics*, 77(6): R227–R238, 2012.

P. Thore, A. Mazuyer, and N. Mastio. Constrained inverse method for estimating virgin stress state. In *81st EAGE Conference and Exhibition 2019*, p. 1–5, 2019.

P. D. Thore and J. A. Edgar. Method of constraining an inversion in the characterisation of the evolution of a subsurface volume, 2017. US Patent App. 15/324,400.

R. Toupin and B. Bernstein. Sound waves in deformed perfectly elastic materials. Acoustoelastic effect. *The Journal of the Acoustical Society of America*, 33(2): 216–225, 1961.

A. Tura, T. Barker, P. Cattermole, C. Collins, J. Davis, P. Hatchell, K. Koster, P. Schutjens, and P. Wills. Monitoring primary depletion reservoirs using amplitudes and time shifts from high-repeat seismic surveys. *The Leading Edge*, 24(12): 1214–1221, 2005.

A. N. Tutuncu, A. L. Podio, A. R. Gregory, and M. M. Sharma. Nonlinear viscoelastic behavior of sedimentary rocks, Part I: Effect of frequency and strain amplitude. *Geophysics*, 63(1): 184–194, 1998.

P. Van Bergen, S. De Gennaro, F. Fairhurst, R. Hurry, M. Concho, J. Watson, L. Sturgess, M. Bevaart, et al. Shearwater-Securing the Chalk-Effects of Depletion of a HPHT Reservoir on Chalk Overburden. In *SPE offshore Europe oil and gas conference and exhibition*, 2013.

J. Walsh. The effect of cracks on the compressibility of rock. *Journal of Geophysical Research*, 70(2): 381–389, 1965a.

J. Walsh. The effect of cracks on the uniaxial elastic compression of rocks. *Journal of Geophysical Research*, 70(2): 399–411, 1965b.

Z. Wang. Seismic anisotropy in sedimentary rocks, part 1: A single-plug laboratory method. *Geophysics*, 67(5): 1415–1422, 2002.

F. Wellmann and G. Caumon. 3-d Structural geological models: Concepts, methods, and uncertainties. In *Advances in Geophysics*, vol. 59, p. 1–121. Elsevier, 2018.

J. White. Computed seismic speeds and attenuation in rocks with partial gas saturation. *Geophysics*, 40(2): 224–232, 1975.

P. Williamson, A. Cherrett, and P. Sexton. A new approach to warping for quantitative time–lapse characterisation. In *69th EAGE Conference and Exhibition incorporating SPE EUROPEC 2007*, 2007.

K. W. Winkler and X. Liu. Measurements of third-order elastic constants in rocks. *The Journal of the Acoustical Society of America*, 100(3): 1392–1398, 1996.

K. W. Winkler and L. McGowan. Nonlinear acoustoelastic constants of dry and saturated rocks. *Journal of Geophysical Research: Solid Earth*, 109(B10), 2004.

M. Wong and C. MacBeth. R-factor recovery via Geertsma's pressure inversion assisted by engineering concepts. In *78th EAGE Conference and Exhibition 2016*, p. 1–5, 2016.

S. Xu and R. E. White. A new velocity model for clay-sand mixtures 1. *Geophysical prospecting*, 43(1): 91–118, 1995.

D. Yale, W. Jamieson Jr, et al. Static and dynamic mechanical properties of carbonates. In *1st North American Rock Mechanics Symposium*, 1994.

M. Zoback, C. Barton, M. Brudy, D. Castillo, T. Finkbeiner, B. Grollimund, D. Moos, P. Peska, C. Ward, and D. Wiprut. Determination of stress orientation and magnitude in deep wells. *International Journal of Rock Mechanics and Mining Sciences*, 40(7-8): 1049–1076, 2003.

M. D. Zoback. *Reservoir geomechanics*. Cambridge University Press, 2010.

## Cohérence d'un modèle de sous-sol en intégrant des données Géologiques, Géomécaniques, Géophysiques et de Simulation d'écoulement

**Résumé :** La production des réservoirs pétrolifères modifie l'état de contrainte du sous-sol. L'extraction du pétrole induit une diminution de la pression des pores et la roche réservoir est soumise à un chargement supplémentaire. Le réservoir n'est la seule région affectée par la production : les couches sus-jacentes et sous-jacentes se déplacent aussi. Pour comprendre l'effet de la compaction du réservoir sur les couches sus-jacentes et sur la subsidence, des modèles géomécaniques sont construits. Le comportement élastique et le changement de la pression des pores sont utilisés pour calculer le champ de déplacement et le changement d'état de contrainte. Néanmoins, les modèles des champs pétrolifères sont entachés d'incertitudes parce que les données sont éparses, mal-comprises et elles sont le résultat d'un traitement long et complexe. L'incertitude des données rends leur interprétation et leur utilisation difficile.

Pour améliorer la prédictibilité des modèles, les données sismiques comme la sismique 4D sont utilisés dans le processus de construction du modèle géomécanique. La sismique 4D est empreinte par l'écoulement des fluides dans le réservoir, par sa déformation et celle des roches environnantes et par l'endommagement des roches. Dans la plupart des champs en production, la quantité de « time-shifts » (la différence en temps de trajet des réflecteurs) dans les roches sus-jacents est importante. Ce signal s'explique en partie par la déformation, mais surtout par le changement de la vitesse des ondes sismiques. L'ouverture de petites fractures peut induire des changements de vitesse fort. Les modèles de fractures permettent d'expliquer ce changement de propriétés élastique durant un changement d'état de contraintes. Grâces à des modèles synthétiques, des auteurs ont prédits que le changement de vitesses est anisotrope parce que le changement d'état de contrainte dans les roches sus-jacentes est anisotrope. Cependant, l'anisotropie du changement de vitesse en sismique 4D n'est pas considérée. L'inversion 4D ne considère que des changements de vitesse verticale.

L'objet de cette thèse est d'extraire plus d'information dans les données pour créer une description plus précise du sous-sol. En utilisant des méthodes d'ensemble, le modèle géomécanique est mis-à-jour en utilisant des données issues de l'inversion sismique 4D. Pour ce faire, nous proposons en premier lieu d'obtenir la variation de pression du réservoir qui permet d'expliquer des données sismiques 4D. Cette étude suggère que la compartimentalisation du réservoir doit être réévaluée afin de comprendre les données sismiques. Puis, nous proposons d'obtenir l'anisotropie du changement de vitesse à partir des données sismiques 4D avant sommation. Une reconstruction tomographique de ce changement de vitesse permets de réaligner la base au monitor. Cette méthode est appliquée sur un cas d'étude réel. L'anisotropie du champ de vitesse obtenue corresponds à une diminution d'$\varepsilon$ et de $\delta$ en termes de paramètres de Thomsen alors que le changement de vitesse verticale est faible. Les modèles géomécaniques montrent que la déformation des roches sus-jacentes est compatible avec l'ouverture de fractures horizontales ; ce n'est pas ce que l'on observe dans notre cas d'étude. Pour expliquer nos résultats, nous proposons un modèle de roches dans lequel se développe une fracturation verticale dans une roche saturée en eau. Ces fractures ont un rapport d'aspect faible (entre $10^{-2}$ et $10^{-3}$). Cette seconde approche nous interroge sur les hypothèses faites quand les prédictions des modèles géomécaniques sont comparées aux résultats d'inversion 4D.

Ces deux approches montrent un grand potentiel dans l'amélioration de la cohérence et la réduction des incertitudes dans les modèles quand différentes données sont confrontées. Davantage d'effort est nécessaire afin de construire un modèle du sous-sol qui permettrait de comprendre toutes les données à notre disposition.

**Mots-clés :** physique des roches, problème inverse, sismique 4D

---

## Improving the global coherency of the *Shared Earth Model* using static, dynamic and geomechanics data

**Abstract:** Petroleum reservoir production modifies the stress state of the subsurface. Petroleum is drawn out, the reservoir pore pressure decreases, and the reservoir rock supports an additional loading. The reservoir is not the only affected area of the field during the production: the layers above (the overburden) and below (the underburden) move. To understand the effect of the reservoir compaction on the overburden and on the subsidence, geomechanical models are built. The rock elastic behavior and the pore pressure change are used to compute the displacement field and the stress changes. In any case, the models of petroleum fields are riddled with uncertainties because the data are sparse and fuzzy and often the results of a long and complex processing. The data uncertainties make the interpretation difficult, or the usage of the prediction made by reservoir models.

To reduce these uncertainties, seismic data such as time-lapse seismic (4D) is used in the geomechanical modelling workflow. 4D seismic are imprinted by the fluid flow in the reservoir, by the strain in the reservoir and in the overburden, and by the rock damaging. In most of the produced fields, the amount of time shifts (the reflectors time-arrival difference) in the overburden is significant. While only a small part of the overburden time shifts is explained by the strain, the velocity change plays a major role. But the relationship between the velocity change and the stress state change due to the reservoir compaction is not known. Microcracks opening is known to have a strong effect on the velocity change. Crack-based models can explain the stress-dependent velocity change in rock samples. Based on synthetics models, different authors predict that the velocity change is anisotropic because the stress change in the overburden is anisotropic. However, the velocity change anisotropy is not considered in the classic time-lapse seismic inversion as only the vertical direction is considered.

The object of this thesis is to extract more information from the data to create a more precise description of the subsurface model. A Mechanical History Matching of time-lapse inverted time strains using Ensemble methods is performed. For this, we first propose to invert for pressure variation in the reservoir to match the time-lapse seismic data. Using the empirical R-factor law, time-lapse time strains are predicted by the mechanical vertical strains. The reservoir pore pressure is updated to match the geomechanical model predictions with the time-lapse inversion results, suggesting that a new compartmentalization of the reservoir is needed to match the 4D information in the overburden. This first approach interrogates on the usage of reservoir simulation data in the geomechanical model. Second, we propose to recover the velocity change anisotropy from prestack time-lapse seismic data. A tomographic reconstruction of the velocity change is performed by realigning the baseline to the monitor. The method is applied to a real case study. The retrieved anisotropic velocity change in the overburden corresponds to a large decrease in $\varepsilon$ and $\delta$ in terms of Thomsen parameters while the vertical velocity change is tiny. Classically, geomechanical models show an overburden stretching corresponding to an opening of horizontal cracks; this is not what we observe in the velocity change anisotropy. To explain the data, we propose a rock-physics model corresponding to vertical cracks with a small aspect ratio (between $10^{-2}$ and $10^{-3}$) in a water-saturated rock. This second approach interrogates on the assumptions made when the geomechanical model simulation results are compared to the time-lapse seismic inversion results.

As shown in the two approaches, a great potential for improving the consistency and reduce uncertainty of the models exists when mixing various data. This work is preliminary and much more work is required to integrate all sources of data into the shared earth model.

**Keywords:** rock physics, inverse problem, 4D seismic